Master's thesis

NTNU
Norwegian University of Science and Technology
Faculty of Natural Sciences
Department of Materials Science and Engineering

Anne-Line Berg Korneliussen

Comparing LiFSI and $LiPF_6$ electrolytes for Algae based Silica Anodes in Li-ion Batteries

Master's thesis in Materials Science and Engineering
Supervisor: Ann Mari Svensson
June 2020

NTNU
Norwegian University of
Science and Technology

Anne-Line Berg Korneliussen

Comparing LiFSI and $LiPF_6$ electrolytes for Algae based Silica Anodes in Li-ion Batteries

Master’s thesis in Materials Science and Engineering
Submission date: June 2020

Supervisor:	Ann Mari Svenson, IMA
Co-supervisor(s):	Maria Valeria Blanco John Viktor Emanuel Renman

Norwegian University of science and Technology
Faculty of Natural Science
Department of Materials Science and Engineering

NTNU
Norwegian University of
Science and Technology

Preface

This thesis is submitted to the Norwegian University of Science and Technology in the course TMT4905 Materials Technology, Master's Thesis, as a finalization of the Master's degree program Materials Science and Engineering. The work, carried out during the spring of 2020, has been supervised by Professor Ann Mari Svensson at the department of Materials Science and Engineering. Dr. Maria Valeria Blanco and Dr. John Viktor Emanuel Renman, of the Department of Materials Science and Engineering, co-supervised the work carried out in this thesis.
As parts of this work resemblance the work carried out in the project "Algae based Silica Anodes for Li-ion batteries"[1] conducted by the author in the fall 2020, theory section 2.1, 2.2 and 2.3.2 resemblance that of the project. However, some additions and modifications have been made.

The initial treatment of as-recieved diatoms, as well as the milling and carbon-coating of the SiO_2 was conducted by Dr. Maria Valeria Blanco and Dr. John Viktor Emanuel Renman. The XPS measurements were made by Øystein Dahl, Research Scientist, SINTEF Industry. Apart from this, all experiments and analysis described in this work was carried out by the author at the Department of Materials Science and Engineering.

Trondheim, June 25, 2020
Anne-Line Berg Korneliussen

Acknowledgments

I would like to take the time to give recognition to the people who have guided and supported me throughout my work. Firstly, special thanks goes to my main supervisor Ann Mari Svensson. Not only have you set aside time for meetings, both in- and outside of working hours, but you have also manage to keep me motivated in this extraordinary trying period. I am grateful for your patience, comprehensive knowledge and guidance. Secondly, I would like to thank my co-supervisors Dr. Maria Valeria Blanco and Dr. John Viktor Emanuel Renman. Thank you for your rapid replays and for taking the time to give me guidance and advices in the laboratory, on e-mails, but also when I have come knocking on your office doors. I am also grateful to you for conducting the initial treatment of as-recieved diatoms, as well as the milling and carbon-coating of the SiO_2.

I would also like to thank the battery group at NTNU. Thank you for always being helpful by providing good input, asking constructive questions and sharing your experiences and tips. Thanks also goes to the technical staff and engineers at the Department of Materials Science and Technology for training and assistance with experimental equipment. Also, thank you Øystein Dahl, for performing the XPS measurements and for being helpful with the analysis of the XPS data.

Finally, I would like to thank my partner and my family for their immense support. Thank you for listening to me rambling about batteries for the past whole year. Also, a big thanks goes to my study buddies for sharing the ups and downs of this final year with me. I could not have done this without you.

Abstract

Energy technology has a vast impact on our society, ranging from environmental challenges and economic development to consumers' electronics and transportation. Looking forward, energy technologies, such as batteries, are predicted to keep growing. In recent years, silica extracted from diatom frustules has been explored as a replacement for graphite anodes in commercial Li-ion batteries, as it has low cost, environmentally friendly and yields a high theoretical capacity.

In this work, the effect of the lithium salt was studied by analysis of the electrochemical data of silica cells with different electrolytes, i.e. electrolytes containing different lithium salts. The silica was extracted from diatom frustules and milled to reduce the particle size. Electrodes with "pure"silica or carbon-coated silica were prepared with 15 wt% water soluble Na-alginate and 10 wt% carbon black. Two different electrolytes, with lithium bis(fluorosulfonyl)imide (LiFSI) and lithium hexafluorophosphate ($LiPF_6$) salt respectively, were used when assembling the coin cells. The cells were cycled galvanostatically with the same cycling programs. After cycling, postmortem characterization was performed by X-ray photoelectron spectroscopy, and also focused ion beam and scanning electron microscopy characterization for selected electrodes.

The capacity of the carbon-coated silica anodes was, as expected, higher than the capacity of silica anodes. For the carbon-coated silica, cells with $LiPF_6$ obtained an average capacity of 669 $mAhg^{-1}$ whereas cells with LiFSI obtained a capacity of 598 $mAhg^{-1}$, i.e cells with $LiPF_6$ obtained a higher capacity than cells with LiFSI. However, for "pure" silica, cells with LiFSI obtained higher capacity than cells with $LiPF_6$, 554 $mAhg^{-1}$ and 516 $mAhg^{-1}$ respectively. The latter is most likely attributed to the SEI formation and the SEI properties. For the carbon-coated silica cells with LiFSI, a small cell degradation was observed, as opposed to the other cells which exhibited good cycling stability. Analysis of the coulombic efficiency revealed that "pure" silica anodes obtained a higher coulombic efficiency than carbon-coated silica cells, regardless of the electrolyte.

Further study of the SEI with XPS indicated that the SEI formation happens at a higher potential for LiFSI than $LiPF_6$. In addition, a difference in where the inorganic and organic components are located in the SEI was observed, indicating that the SEI formed with LiFSI is both more flexible but also more conductive than the SEI formed with $LiPF_6$.

Sammendrag

Energiteknologi har en stor innvirkning på samfunnet vårt, alt fra miljøutfordringer og økonomisk utvikling til forbruker elektronikk og transportsektoren påvirkes av energiteknologi. I fremtiden vil energiteknologier, slik som batterier, fortsette å vokse. Derfor har det i nyere år blitt forsket alternative materialer til å erstatte grafittanodene i kommersielle Li-ion batterier. Silisiumoksid utvinnet fra kiselalger er et av materialene som har blitt undersøkt, da det er rimelig, miljøvennlig og har en høy teoretisk kapasitet.

I dette arbeidet er effekten av litiumsalt studert ved å analysere de elektrokjemiske dataene fra celler med forskjellig aktivt materiale og forskjellige elektrolytter, dvs. elektrolytter med forskjellige litiumsalt. Silisiumoksidet som ble brukt er utvunnet fra kiselalger og malt opp for å redusere partikkelstørrelsen. Elektroder av «rent» silisiumoksid og karbonbelagt silisiumoksid ble laget med 15 vekt% vannløselig Na-alginat og 10 vekt% karbon (carbon black). Battericeller ble laget med de to forskjellige elektrolyttene, som inneholdt henholdsvis litium-bis(fluorosulfonyl)imid (LiFSI) salt og litiumheksafluorfosfat ($LiPF_6$) salt. Cellene ble syklet galvanostatisk med samme syklingsprogram. Etter endt sykling ble postmortem karakterisering med røntgenfotoelektron-spektroskopi utført, i tillegg til ytterligere karakterisering med focused ion beam (FIB) og skanning elektronmikroskop (SEM) på utvalgte elektroder.

Kapasiteten til de karbonbelagte silisiumoksidanodene var som forventet høyere enn kapasiteten til «rene» silisiumoksidanoder. For karbonbelagt silisium oppnådde celler med $LiPF_6$ en gjennomsnittlig kapasitet på 669 $mAhg^{-1}$, mens celler med LiFSI oppnådde en kapasitet på 598 $mAhg^{-1}$, dvs. at celler med $LiPF_6$ oppnådde en høyere kapasitet enn celler med LiFSI. For "ren" silisium oppnådde celler med LiFSI imidlertid høyere kapasitet enn celler med $LiPF_6$, da gjennomsnittlig kapasitet var henholdsvis 554 $mAhg^{-1}$ og 516 $mAhg^{-1}$ for LiFSI of $LiPF_6$. Denne forskjellen i ytelse mellom LiFSI og $LiPF_6$ er knyttet til SEI (solid electrolyte interface)-formasjonen og egenskapene til SEIen. For de karbonbelagte silisiumoksid cellene med LiFSI ble det observert en synkende trend i kapasitet under sykling, noe som indikerte nedbryting av cellen. De andre cellene viste derimot god sykkelstabilitet. Analyse av den coulombiske-effektiviteten avslørte at "rene" silisiumoksid anoder oppnådde en høyere coulombisk-effektivitet enn karbonbelagte silisiumoksid anoder, uavhengig av type elektrolytt.

Videre studier av SEI med XPS indikerte at SEI-formasjonen skjer på et høyere potensial for LiFSI enn $LiPF_6$. I tillegg ble det observert en forskjellige i hvor de ulike organiske og uorganiske komponentene kan lokaliseres i SEI, hvilket indikerte at SEI dannet med LiFSI er mer fleksibel, men også mer ledende enn SEI dannet med $LiPF_6$.

Table of Contents

List of Abbreviations

CB	Carbon black
CE	Coulombic efficiency
CPS	Counts per second
DI-water	Deionized water
DEC	Diethyl carbonate
DMC	Dimethyl carbonate
EC	Ethylene carbonate
EMC	Ethyl methyl carbonate
FIB	Focused ion beam
HF	Hydrofluoric acid
ICL	Irreversible capacity loss
IPA	Isopropanol
LCO	$LiCoO_2$
LEDC	Lithium ehylene dicarbonate
Li-ion	Lithium-ion
LiFSI	Lithium bis(fluorosulfonyl)imide
$LiPF_6$	Lithium hexafluorophosphate
PC	Propylene carbonate
PVDF	Polyvinylidene fluoride
Redox	Reduction-oxidation
SEI	Solid-electrolyte interphase
SEM	Scanning electron microscope
V_{OC}	Open circuit voltage
WE	Working electrode
XPS	X-ray photoelectron spectroscopy

Chapter 1: Introduction

Energy technology has a vast impact on our society, ranging from environmental challenges and economic development to consumers' electronics and transportation. Looking forward, energy technologies, such as batteries, are predicted to keep growing in the future.

Today Li-ion technology has conquered the portable electronic markets and is the dominating solution for high energy (i.e. automotive) and high-power applications, due to their superior power and energy density.[2] Global warming, finite fossil-fuel supplies and city pollution are driving forces for society to convert to more renewable energy and electric transport.[3] The development of new battery technology will continue to shape the transportation sector, as not only vehicles are becoming electric, but also ferries and potentially aircraft in the future. Also, personal electronics can be further developed by new battery technologies. In rural areas, such as sub-Sahara Africa, there are hundreds of millions of people living off central power grids, i.e. without access to electricity, stalling the economic development of these areas.[4] To offer these communities clean and decentralized energy, mini-grids can be installed storing energy produces from local solar- or windmill plants. Here, lithium-ion batteries are ideal energy storage systems, granted that they have a long lifespan, high density of energy and high density of power.[5] With these mini-grids the development of businesses in addition to improving the living standards is enabled.[4] Hence, the development of new battery technology can have a profound impact on both our personal life and the society at large.

For a widespread application of battery technology to meet the demands of these different sectors, a series of challenges must be overcome. The most demanding challenge is to increase the energy density of the batteries, while simultaneously decreasing the costs and not increasing the size. Another important aspect is that as the battery technology replaces other technologies, such as in vehicles, the number of batteries in circulation increases. However, the "design life span" of lithium-ion batteries, considered to be on average 9 years, is low leading to an increase in the waste stream produced by the battery industry.[6] Thus, the future batteries are expected to be composed of more sustainable materials, being both environmentally friendly and abundant. Thereby, the overall challenge is to develop batteries with improved energy density composed of environmentally benign components, at a reduced cost.

To meet the requirements of new battery technology, various materials have been researched as potential new anode materials. Today, commercial lithium-ion batteries use graphite as the anode material, with a capacity of 372 $mAhg^{-1}$.[7] To replace the graphite, other materials with high capacities, such as silicon has been considered. Silicon has been researched as a potential anode material since the 1990s and yields a theoretical capacity of ~3600 $mAhg^{-1}$, thus showing great potential.[8] However, some problems where discovered. When the silicon reacts with lithium there is a huge volume expansion, up to 400 %, resulting in cracking and pulverization of the anode, and thus a short lifetime.[9] Another drawback of silicon as an anode material is the environmental aspect. Most pure grade silicon is obtained from reacting crystalline silica (SiO_2) with carbon at elevated temperatures, resulting in a high CO_2 footprint of 3.5 - 11 kg CO_2 per kg silicon produced.[2]

Among silicon-based materials silica (SiO_2), is an environmentally friendly and low-cost option, as well as one of the most abundant materials on Earth. Silica has a theoretical specific capacity up to 1965 $mAhg^{-1}$ and reacts with lithium in different ways, forming lithium oxides, lithium silicates and silicon. When the silicon formed reacts with the lithium there will still be a volume expansion, however, this expansion will to some extent be buffered by the lithium silicates and the negative effects of the volume changes are minimized.[9,10]
As SiO_2 is an insulating material a coating may be applied, using a highly conductive material, to improve the conductivity and stability of SiO_2. Carbon is most commonly used for coating, due to its good electronic conductivity and low cost.

The electrolyte, which ensures the conduction of the lithium-ions between the negative and positive electrodes, has a strong impact on battery performance. Here, the lithium salt used is essential to ensure the high ionic conductivity of the electrolyte.[11] Today, $LiPF_6$ is the most commonly used lithium salt in commercialized Li-ion batteries.[11] However, $LiPF_6$ is thermally unstable and extremely sensitive to traces of water and alcohol which leads to the formation of hydrofluoric acid (HF). The formation of HF degrades the battery and is a safety hazard, thus a replacement of the $LiPF_6$ salt is desired.[12] LiFSI is a new lithium salt, presenting good ionic conductivity in addition to having good stability towards hydrolysis.[13] Recent studies by Philippe *et al.* showed that LiFSI salt had a beneficial role in improving the electrochemical performance of Li/Si cells.[14]

The lithiation mechanisms of silica are not well understood, nor is the lithiation mechanism of silicon. To understand this better an investigation of the interaction between the electrolyte, containing lithium salts, and the anode material will be made in this thesis. When the electrolyte reacts with the surface of the anode a solid electrolyte interface (SEI) layer is formed. The SEI consists of electrolyte decomposition products and the composition of the SEI is dependent on the electrolyte composition and the anode material. The preliminary SEI is formed during the first delithiation, where some lithium will be consumed causing an irreversible capacity loss. The properties of the SEI are important for the stable performance of anodes.

Aim of this Work

The main goal of this work is to address the effect of lithium salt by investigating if SiO_2 anodes yield better electrochemical properties with LiFSI salt rather than the common $LiPF_6$ salt. Here, cells with both "pure" SiO_2 anodes and anodes with carbon-coated SiO_2 will be studied.

The performance of the cells will be assessed by the electrochemical data. Moreover, an additional study of the solid electrolyte interphase (SEI) will be conducted by XPS to better understand the differences between the two lithium salts observed by electrochemical characterization.

Chapter 2: Theory

The purpose of this chapter is to provide a theoretical framework for further discussion throughout this report. First, an introduction to galvanic cells and secondary batteries is given. Then, the different components of battery cells in general, with a focus on Li-ion batteries, are given in more detail. Following this a further description of silicon (Si) and silica (SiO_2) anodes are given. Finally, a section covering different characterization techniques relevant to this thesis.

Although SiO_2 anodes are the main topic of this thesis, the review provided in this chapter includes both Si anodes and SiO_2 anodes. The reason for this is twofold. Firstly, silicon and silica have relatively similar chemistry. Secondly, upon charging in the Li-ion battery, SiO_2 anodes are gradually converted to Si and other components, such that the main charge storage mechanisms are the alloying of lithium in silicon. Besides, the amount of research published on SiO_2 anodes is limited.

2.1 Galvanic cells and secondary batteries

A battery is an electrochemical device that converts chemical energy into electrical energy by reduction-oxidation (redox) reactions taking place at the electrodes. The term battery refers to either a single electrochemical cell or a stack of electrochemical cells in series and/or parallel. Here, the focus is on describing single cells.

There are two main types of batteries; primary cells and secondary cells. The reactions occurring in the former are irreversible, while the reactions occurring in the latter are reversible. Another way to phrase this is to say that the primary cells operate solely in the galvanic mode, while the secondary cells operate in the galvanic as well as the electrolytic mode, and can thereby be recharged.[15] The electrodes in secondary batteries will, therefore, alternate between hosting the reduction and oxidation reaction, depending on whether or not the batteries are charged or discharged.

2.1.1 The fundamental principles of Lithium-ion batteries

Li-ion batteries have grown to become the dominant energy storage solution for portable information technology devices, since its commercialization in 1991.[16]
The Li-ion battery consists of four major components; a cathode, an anode, an electrolyte and a separator. During charging of the cell, Li-ions are released from the cathode and migrate through the electrolyte, and separator, into the carbon in the anode. During the discharging, the reverse reaction occurs. Hence, batteries can store and release electric energy.[16]
The most common cathode material is $LiCoO_2$ (LCO), while graphite is the most common anode material. The reactions occurring during charging and discharging can be described by the following reactions:[7]

$$\text{Anode:}\quad 6C + xLi^+ + xe^- \rightleftharpoons Li_xC \tag{2.1}$$
$$\text{Cathode:}\quad LiCoO_2 \rightleftharpoons Li_{1-x}CoO_2 + xLi^+ + xe^- \tag{2.2}$$
$$\text{Total Cell reaction:}\quad LiCoO_2 + 6C \rightleftharpoons Li_{1-x}CoO_2 + Li_xC \tag{2.3}$$

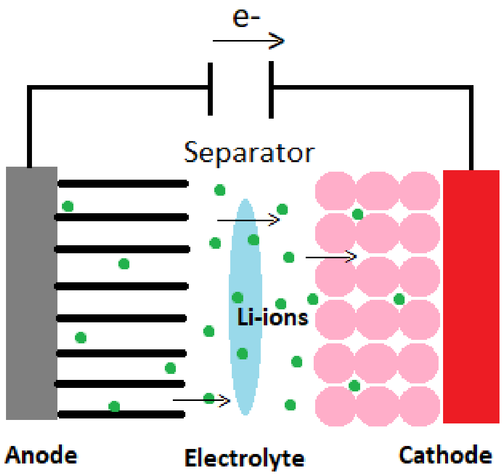

Fig. 2.1. Schematic of conventional Li-ion battery with a graphite anode. The directional flow of Li-ions and electrons during discharge is illustrated.

Alumina foil and copper foil are normally used as current collector material for the cathode and anode respectively. The current collector plays no role in the cell's chemistry but ensures good electrical contact between the electrode and the external circuit. The electrolyte, a good ionic conductor, allows the ions to move between the electrodes but has a limited electrical conductivity. The role of the separator is to physically separate the electrodes, and thus prevent short-circuiting. The property of the separator ensures that the electrolyte is kept between the two electrodes; at the same time it allows for ionic conduction, but electric insulation of the electrodes.[17] This forces the electrons to go through the external circuit, as illustrated in Figure 2.1.

2.2 Battery terminology

The total amount of energy that can be stored in the charging process can be expressed as:

$$\text{Energy} = \int_0^Q V(q)dq \tag{2.4}$$

where V(q) is the potential when charge q is moved from one of the electrodes to the other, and Q is the total amount of charge taking place in process of charging the battery.[18] The total energy of the battery, given by equation 2.4 can be improved by either increasing the total amount of charge involved in the charging process (Q) or maximize the potential of the battery V(q) throughout the charging cycle. If the V(q) is to be maximized, the open circuit potential (V_{OC}) and the potential changes as a function of the state of charge has to be considered.
V_{OC} of a full cell is given by the difference in the electrochemical potentials of the two electrodes:

$$V_{OC} = \frac{\mu_a - \mu_c}{e} \tag{2.5}$$

where μ_a is the electrochemical potential of the anode, μ_c is the electrochemical potential of the cathode and e is the magnitude of an electron charge.[18]

The energy density of a battery is usually given in terms of gravimetric energy density or volumetric energy density and reflects the utility of a battery in a practical setting. The gravimetric - and volumetric energy densities are given by:[18]

$$\text{Gravimetric Energy Density} = \frac{\int_0^Q V(q)dq}{\text{wt}} \tag{2.6}$$

$$\text{Volumetric Energy Density} = \frac{\int_0^Q V(q)dq}{\text{vol}} \tag{2.7}$$

The power density of a battery is especially important for applications of batteries in portable electronics and electric vehicles. The output power of a battery is given by:[18]

$$P(q) = V(q)I_{dis} \tag{2.8}$$

$$\text{Volumetric Power Density} = \frac{P(q)}{\text{vol}} \tag{2.9}$$

where I_{dis} is the discharge current.

The cycle life of a battery is the number of cycles until the capacity fades to 80% of its initial reversible value.[18] The capacity loss of a single cycle is often given by either the coulombic efficiency (CE) or the irreversible capacity loss (ICL), given as:

$$CE = 100\frac{Q_{dis}}{Q_{ch}} \tag{2.10}$$

$$\mathrm{ICL} = 100\frac{Q_{ch} - Q_{dis}}{Q_{ch}} \tag{2.11}$$

here Q_{dis} is the capacity during discharge and Q_{ch} is capacity during charge.[18] The capacity of a battery is a measure of the charge that is stored by the battery and is determined by the mass of active material contained in the battery. The battery capacity can be defined as the maximum amount of energy that can be extracted from the battery under specified conditions.

The total loss in capacity over multiple cycles, cumulative capacity loss (CCL), can be defined as:

$$\mathrm{CCL} = \sum_{k} Q_{ch} - Q_{dis} \tag{2.12}$$

where k is the number of cycles.

2.3 Cell components

The goal of this section is to give a general introduction to the different parts of a battery cell.

2.3.1 Electrolytes and the solid electrolyte interface

Electrolyte

The electrolyte is one of the three main parts of the Li-ion battery. It acts as a physical barrier between the positive and negative electrodes, when coupled with a separator for liquid electrolytes, as well as it ensures the conduction of the Li-ions between the two electrodes. The chemical nature of the electrolyte has a strong impact on battery performance, especially on the electrode/electrolyte interfaces.[11] The electrolyte constituents can be the object of redox reactions occurring near the electrode surface, leading to decomposition of the electrolyte and deposition of some electrolyte decomposition products at these interfaces. In Figure 2.2 the electrochemical window of an electrolyte is illustrated. For an electrolyte to be thermodynamically stable the electrochemical potentials of the electrodes, i.e. μ_A and μ_C, must be within the electrochemical window (E_g). However, μ_A for all realistic electrolytes lies above the LUMO of Li-anodes (i.e. metallic Li, Si, and graphite). Hence, a reduction of the electrolyte is inevitable and thus a solid electrolyte interface is formed.

An ideal electrolyte has some general requirements to fulfill:[12,11,19]

- Large electrochemical potential window: the redox potential of both electrode materials should fall within this window to avoid oxidative or reductive degradation of the electrolyte, i.e. $eV_{OC} = \mu_A - \mu_C \leq E_g$ in Figure 2.2. Thus, with a limited E_g($\sim$ 1.2eV), aqueous electrolytes are excluded in favor of non-aqueous electrolytes.
- High ionic conductivity ($\sigma_{Li} > 10^{-4}$ Scm^{-1}) and low electronic conductivity ($\sigma_e > 10^{-10}$ Scm^{-1}) over a wide range of temperature range (-40 °C to +60 °C)

- Chemically stable towards all the cell components (separator, current collectors, cell packaging materials)
- Should form a stable passivation layer, i.e. an SEI layer, at the surface of the electrodes. (The SEI will be discussed in more detail later in this Section)
- Be able to tolerate extreme conditions (electric, mechanical and thermal abuse)
- Low toxicity and low cost

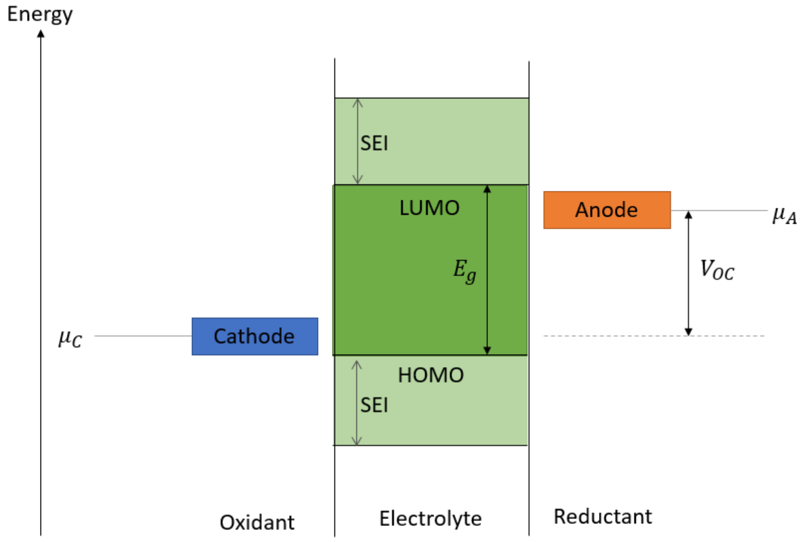

Fig. 2.2. Schematic open-circuit energy diagram of an electrolyte. Modified illustration from Goodenough *et al.*[12]

The role of the electrolyte is to serve as a medium for the transfer of charge, i.e. ions, between the electrodes in the battery.[19] The electrolyte could be viewed as the inert component of the battery, as all Faradaic processes are expected to occur within the electrode. The electrolyte must demonstrate stability against both cathode and anode surfaces, this electrochemical stability is especially important in rechargeable battery systems.[20]

The ability the electrolyte has to conduct ions can be quantified by the parameter, ionic conductivity, given by

$$\sigma = \sum_{\mathrm{i}} \mathrm{N_i u_i Z_i e} \tag{2.13}$$

where N_i is the number of free ions, u_{i} the ion mobility, Z_i the valence of ionic species i and e the fundamental charge of an electron.

In general, the electrolyte is specifically designed for a particular battery application comprised of a mixture of salt, multiple solvents, and electrolyte additives, to meet the aforementioned requirements of an electrolyte.

Electrolyte salts and solvents

In liquid electrolytes, a huge variety of solvents can be used (organic or inorganic). There are some additional requirements for a liquid electrolyte for lithium-ion batteries:[11,19]

- Be able to dissolve a lithium salt to a sufficient concentration (high dielectric constant ε)
- Have a low viscosity η to facilitate ion transport.
- Be in the liquid state in a wide temperature range (low melting point (T_m) and high boiling point (T_b))
- Be aprotic because of the highly reducing negative electrodes and the highly oxidizing positive electrode
- It should also be safe (high flash point T_f), non-toxic and economical.
- As all liquid electrolytes have a LUMO below the electrochemical potential of most common anodes, like graphite or silicon, the ability to kinetically stabilize the anode by the formation of a passivation layer, so-called solid electrolyte interphase, is critical.

In practice, it is difficult to find a single compound with all these properties, hence a mixture of different solvents is generally used.

In Li-ion batteries, the most common solvents are ethylene carbonate (EC), propylene carbonate (PC), dimethyl carbonate (DMC), diethyl carbonate (DEC) and ethyl methyl carbonate (EMC). The chemical structures of these carbonates are shown in Figure 2.3, where EC and PC are aromatic components and DMC, DEC and EMC are linear.

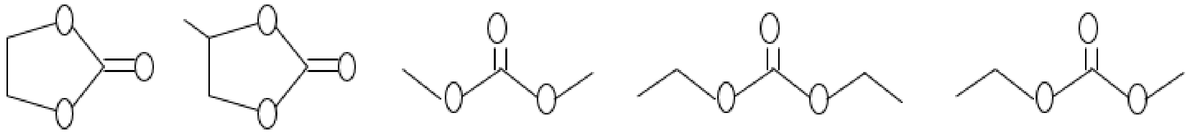

Fig. 2.3. Chemical structures of common electrolyte solvents. From left to right EC, PC, DMC, DEC and EMC.

Carbonates are organic liquids that are reasonably good solvents for Li salts with a wide electrochemical window between 4.7 V (HOMO) and 1.0 V (LUMO) vs Li^+/Li^0.[12] The aromatic compounds, EC and PC, are polar solvents, and needed for good dissolution of the lithium salts. However, as EC and PC are very viscous, the addition of linear carbonates is required to lower the viscosity.

To ensure high ionic conductivity of the electrolyte the lithium salt is essential. Specifications for the lithium salt are as follows:[11]

- Complete dissolution and dissociation in non-aqueous solvents
- High mobility of the solvated ions in the solvents selected
- Inert anion towards the solvents and stable against oxidative decomposition at the positive electrode

$LiPF_6$ is the most commonly used lithium salt in commercialized Li-ion batteries, due to its well-balanced properties as an electrolyte salt.[19] However, $LiPF_6$ is very sensitive to moisture, and hydrofluoric acid will form as there is always trace amounts of water present in the electrolyte:[12]

$$LiPF_6 \leftrightarrow LiF + PF_5 \tag{2.14}$$

$$PF_5 + H_2O \rightarrow 2HF + PF_3O \tag{2.15}$$

These reactions degrade the battery and lead to safety hazards. However, additives have been shown to prevent this decomposition of $LiPF_6$.[12]

As $LiPF_6$ is sensitive to water and alcohol and its thermal instability can present safety problems, alternatives to replace $LiPF_6$ have been studied.[11] Successfully tests with imide salts have been carried out and the most efficient salt is lithium bis(fluorosulfonly)imide: $Li[N(SO_2F)_2]$ (LiFSI).[11]
The LiFSI salt presents a good ionic conductivity, better than that of $LiPF_6$. Also, LiFSI has good stability towards hydrolysis and exhibits good anticorrosive properties towards aluminum when it is very pure.[13]

LiFSI has several advantages over the classic conducting salt, $LiPF_6$, as reported by Liu *et al.*[21] and Han *et al.*[22] summarized by Zhang *et al.*[13] below:

1. LiFSI is more thermally stable than $LiPF_6$.
2. LiFSI exhibits far superior stability toward hydrolysis than $LiPF_6$ in dipolar aprotic carbonate solvents and almost does not generate HF.
3. LiFSI is highly soluble in most polar solvents due to its low melting point (i.e., low lattice energy), and a concentration of 5 M was reached in DMC, despite its low dielectric constant.
4. LiFSI is more dissociated in carbonates than $LiPF_6$, due to the weaker coordinating ability of FSI^- vs. PF_6^-. The ionic conductivities of LiFSI in carbonates are all higher than those of electrolytes with other common lithium salts, e.g., 9.73 $mScm^{-1}$ (LiFSI) vs. 9.33 $mScm^{-1}$ ($LiPF_6$) (1.0 M solute in a mixture of EC/EMC (3:7, v/v) at 25 °C).

Solid electrolyte interface

The electrochemical window, which gives the thermodynamic stability of the electrolytes, is given by the energy separation (E_g) of the lowest unoccupied molecular orbital (LUMO) and the highest occupied molecular orbital (HOMO). The electrochemical potentials of the electrodes must be within the electrochemical window of the electrolyte to be electrochemically stable. However, for most high voltage batteries the V_{OC} lies outside the electrochemical window of most electrolytes, and all electrolytes are outside the window of the most common anodes, graphite and Si. Thus, the requirement of electrolyte stability is not met by the thermodynamic stability, but rather the kinetic stability.[12]

A passivating solid electrolyte interface (SEI) layer at the electrode/electrolyte boundary can give kinetic stability. When the lithium is in contact with the electrolyte solution a layer, consisting of insoluble and partly soluble reduction products of electrolyte components, forms instantaneously. This passivating layer blocks the electronic current and only ionic current is enabled to pass. The layer acts as an interphase between the lithium and the electrolyte and has the properties of a solid electrolyte with high electronic resistivity, hence the name solid electrolyte interphase.[20] The same applies for anode materials like graphite and silicon.

The SEI is important as it determines the morphology of lithium deposits, power capability, shelf life, cycle life and safety of the battery.[20] It also prevents further decomposition of the electrolyte and plating of Li on the anode during the fast charging of the battery.

The SEI formation is generally reported to start below 0.8 V.[11] However, the electrolyte stops decomposing when the SEI layer reaches a critical thickness and covers the entire surface of the electrode, preventing the migration of electrons. To ensure good cyclability of the battery, the SEI has to be electronically isolating but ionically conducting.

The formation of the SEI contributes, firstly to a part of the initial irreversible capacity loss, and then, its properties (thickness, composition, morphology, and density) are crucial for the battery behavior upon long-term cycling.[11] Philippe lists the following requirements that an ideal SEI has to meet:[11]

- Very low electronic conductivity ($t_{e^-} \sim 0$)
- High ionic conductivity $t_{Li^+} \sim 1$)
- Uniform and stable composition and morphology to prevent further electrolyte decomposition
- Good adhesion to the electrode materials
- Good flexibility and mechanical properties to accommodate the volume expansion
- Low solubility in the electrolyte to avoid further electrolyte degradation

It is also important to note that besides the chemical factors, the electrochemical cycling conditions and the temperature also have an impact on the SEI.

The electrolyte needs to be inert towards both the anode and the cathode material. Given the strong reducing and oxidizing power of the electrode materials, the possibility of a stable electrolyte is similar to nonexistent. Hence, the passivation of the electrode surfaces ensures the inertness of the bulk electrolyte.[19]

The passivation layer forms as the product of the initial electrolyte decomposition deposits on the pristine surface of the electrode, forming a dense, protective film preventing sustained decomposition.

2.3.2 Anode materials

Anode materials can be divided into three main categories; intercalation anodes, alloying anodes and conversion anodes. In this section, the different anodes are discussed.

Intercalation anode

Intercalation involves the insertion of an element, in our case an ion, into an unoccupied site in the crystal lattice. The host material usually has a stable crystal lattice, with a layered- or tunnel structure, which provides a pathway for guest ions to diffuse.[19] Kang Xu wrote in his chemical review that by injecting or extracting electrons, the redox reactions occur on the host lattice while mobile guest ions intercalate into or deintercalate from the host matrix to ensure regional electroneutrality.[19] During the full intercalation/deintercalation cycle, the "guest ion" is not involved in reactions forming new products.[19] Graphite is the most known intercalation anode. The final product of reversible lithiated graphite is given by the reaction:

$$C_6 + Li^+ + e^- \rightleftharpoons LiC_6 \tag{2.16}$$

whit a reversible capacity of 372 $mAhg^{-1}$.[7] These graphite anodes have a long cycle life and a coulombic efficiency larger than 99%.

Alloying anode

Lithium metal alloys Li_xM_y (M = Si, Sb, Sn, Al, Ge, etc.) have been studied as negative electrode materials for Li-ion batteries. In the alloying mechanism, bonds between host-atoms are broken, causing dramatic structural changes. The atomic framework of the host thereby does not constrain the reaction and anode materials that form alloys can, therefore, have a much higher specific capacity than intercalation electrode materials, e.g. $Li_{4.4}Si$ has a theoretical capacity of 4200 $mAhg^{-1}$.[7] Si is a well known alloying anode and will be discussed further in Section 2.4.

Conversion anode

Conversion anodes are a promising substitute for the intercalation anode as it yields a high theoretical capacity, have good cycling behavior, and are low cost. The conversion anode is based on the conversion reaction and can be expressed as:[7]

$$M_xX_y + yne^- + ynLi^+ \leftrightarrow xM^0 + yLi_nX \tag{2.17}$$

where M_xX_y denotes a binary transition-metal compound (M = Fe, Mn, Ni, Co, Cu; X = O, S, P, S) and n is the formal oxidation state of the anion. SiO_2 is a conversion anode and will be discussed further in Section 2.5.

Requirements of anode materials

An ideal anode material should fulfill the following requirements:[7]

1. It must be light and accommodate as much Li as possible to optimize the gravimetric capacity.
2. Its redox potential with respect to Li/Li^+ must be as small as possible at any Li-concentration.
3. It must possess good electronic and ionic conductivities since faster motion of the lithium ions and the electrons also mean higher power density of the cell.
4. It must not be soluble in the solvents of the electrolyte and not react with the lithium salt.
5. It must be safe, i.e. avoid any thermal runaway of the battery.
6. It must be cheap and environmentally friendly.

Today, the intercalation compound, graphite, is most used. Graphite anodes have a theoretical capacity of 372 $mAhg^{-1}$, this together with the challenges related to Li deposition and dendrite growth, which is a severe safety issue, are good reasons for researching new anode materials that satisfies several of the requirements above.

2.3.3 Electrode binders

The electrode binder, used in most electrodes, ensures good adhesion between the active material, the conductive additives and the current collector, thus maintaining good electronic conductivity.
The most conventional binder used for batteries is poly(vinylidene fluoride) (PVDF). However, PVDF only forms weak van der Waal bonds to Si and fails to accommodate the large volume expansions of the Si reactions.[23] Therefore, research has been carried out on polymeric binders such as carboxymethyl cellulose (CMC) and sodium alginate as an alternative binder for Si.

Alginate binder was found to yield a stable Si-based anode.[24] Unlike PVDF and CMC, Alginate has a high content of carboxyl moiety, which can lead to many possible bonds with Si particles. Importantly, the carboxyl moieties in Na alginate are uniformly distributed, unlike CMC with a random distribution of carboxyl groups. It was explained that this uniform distribution of carboxyl moieties can lead to a more uniform coverage and more efficient assistance with the formation of SEI on the Si.[24 ,25]

2.4 Si anodes

Silicon anodes are one of the most promising candidates to replace graphite. The desirable traits of silicon are the following:[7 ,26]

1. Si has a high theoretical capacity.
2. The onset potential of the alloying of Si with Li is 0.3-0.4 V above the Li/Li^+ redox potential, which gives a good balance between limiting lithium plating and yielding a reasonable V_{OC} in a full cell.
3. Si is abundant and potentially low cost
4. Si is environmentally friendly and non-toxic

Hence, Si satisfies many of the mentioned requirements of anode materials mentioned in Section 2.3.2.

2.4.1 The nature of Si and SiO_2

Si and SiO_2 are respectively the oxidation and reduction products of each other. Hence, Si particles are often covered by a thin layer of SiO_2.[27] The reason that the relationship between Si and SiO_2 is important to this work is twofold. First, the lithiation mechanism of SiO_2 involves the reduction of SiO_2 to Si (which will be covered in section 2.5.2).[10] Hence, to fully understand the lithiation mechanisms of SiO_2, one also needs to understand the lithiation mechanisms of Si. Second, there is limited research available on SiO_2 anodes, hence published results on Si anodes may serve as a guideline for research on SiO_2 anodes.

2.4.2 Lithiation mechanism of Si

The lithiation mechanisms of Si and Li^+ is yet to be fully understood, despite the increased research on Si as anode material. Multiple Li_xSi compounds have been detected during lithiation, however, the formation of these compounds is dependent on the cycling speed and the lithiation cut-off potential.[28]

Initial research by Wen and Huggings determined that $Li_{4.4}Si$ was the most lithium-rich intermediate phase in the Li-Si system[29] with a theoretical capacity of 4200 $mAhg^{-1}$.[26] However, the $Li_{4.4}Si$ phase is not stable at room temperature.[30] Hence, crystalline $Li_{3.75}Si$ is the final lithiation product of Si under practical operating conditions, yielding a theoretical capacity of 3579 $mAhg^{-1}$.[8]

A study of the lithiation mechanisms of Si-nanowires by Ogata *et al.* proposed that Li^+ first reacts with crystalline Si forming different amorphous Li_xSi compounds, then a crystalline $Li_{3.75}Si$ phase and lastly an over-lithiated $Li_{3.75+\delta}Si$ phase is formed.[28] An overview of the proposed lithiation "stages" by Ogata *et al.* is presented in Table 2.1.

Tab. 2.1. Lithiation and delithiation mechanisms of Si as proposed by Ogata *et al.*[28]

Cycle/Stage	Reaction	Potential [V]
1st Lithiation	$c-Si \rightarrow a-Li_xSi \rightarrow c-Li_{3.75}Si \rightarrow c-Li_{3.75+\delta}Si$	0.10
≥ 2nd Lithiation		
2	$a-Si \rightarrow a-Li_{2.0}Si$	0.30 - 0.25
3	$a-Li_{2.0}Si \rightarrow a-Li_{3.5}Si$	0.10
4	$a-Li_{3.75}Si \rightarrow c-Li_{3.5}Si$	0.05
5	$c-Li_{3.75}Si \rightarrow c-Li_{3.5+\delta}Si$	0.03
Delithiation		
1	$Li_{3.5+\delta}Si \rightarrow c-Li_{3.5}Si + c-Li_{3.5-\delta}Si$	0.05 - 0.15
2	$a-Li_{3.5}Si \rightarrow a-Li_{2.0}Si$	0.27
3	$c-Li_{3.5}Si \rightarrow a-Li_{1.1}Si$	0.43
4	$a-Li_{2.0}Si \rightarrow a-Si$	0.50

2.4.3 Challenges of Si as anode material in Li-ion batteries

Drastic volume expansion (up to 420% for $Li_{4.4}Si$[7]) and huge stress generation are accompanied with the lithiation/delithiation process of Si, causing a series of destructive consequences:[26]

1. Electrode structure integrity is deteriorated due to gradually enhanced pulverization during repeated discharge/charge processes
2. Disconnection between the electrode and current collector is induced by the interfacial stress
3. Continuous consumption of lithium ions occurs during the continuous formation-breaking-reformation process of solid electrolyte interface (SEI) due to the expansion and continuous exposure of fresh surface

All these processes accelerate electrode collapse and capacity fading synergistically.[26]

2.4.4 SEI formation on silicon anodes

During the first discharge, the SEI is formed on the surface of the anode. However, when silicon alloys with lithium, the huge volume expansion leads to cracking of the SEI, and a continuous reduction of the electrolyte occurs during subsequent cycling. In addition to the consumption of electrolyte (Li source), a growth of the SEI limits Li-ion diffusion through it and reduce the kinetics and performance of the system.[11] Some of the species found in the SEI are Li_2CO_3, $ROCO_2Li$, and LiF. Similar SEI compounds have been identified on carbon-based electrolytes as well.[11]

To prevent cracking of the preliminary SEI formed on the anode surface, research has been done on electrolyte additives. Successful results to stabilize the SEI have been obtained by the addition of electrolyte additives like fluoroethylene carbonate (FEC)[31,32] and vinylene carbonate (VC)[33,34] . These additives have higher reduction potentials than the common electrolyte solvents, such as EC, enabling them to decompose and form more flexible and stronger SEI layers.[31]

2.5 SiO_2 anodes

SiO_2 is widely utilized in the glass and electronics industries. In the context of battery applications, SiO_2 was initially considered an electrochemical inactive material as it would not react with lithium due to the stability of the oxide.[9] However, in 2001 Gao *et al.* reported that SiO_2 nanoparticles were found to react with Li in the voltage range of 0.0 V - 1.0 V.[35] The theoretical specific capacity of SiO_2 can range up to 1965 $mAhg^{-1}$, depending on the lithiation mechanism.[10] In addition, SiO_2 is found to have great cycling stability.[10] Hence, silica-based materials are important candidates as anode material for Li-ion batteries, not only because of their good electrochemical performance, but also due to the low cost, low toxicity and abundance in the earth crust.[36]

The topics of SiO_2 and silicon oxide (SiO_x for $0 < x < 2$) are discussed somewhat interchangeably in the literature. SiO_x can both refer to core-shell Si/SiO_2 particles with various silicon/silica ratios, or homogeneous SiO_x particles.[37] In this work, the therm SiO_x will simply refer to materials where the distribution of Si and SiO_2 is unknown.

2.5.1 SiO_2 as anode material

In literature, the discussion regarding SiO_2 as an anode material can be divided into three categories; SiO_2 as a feedstock for Si anodes, SiO_2/Si composites and SiO_2 as the main active material. An overview of the usage of SiO_2 in battery anodes is given in Figure 2.4.[17] In this work, the use of SiO_2 as the main active material in the anode is the focus.

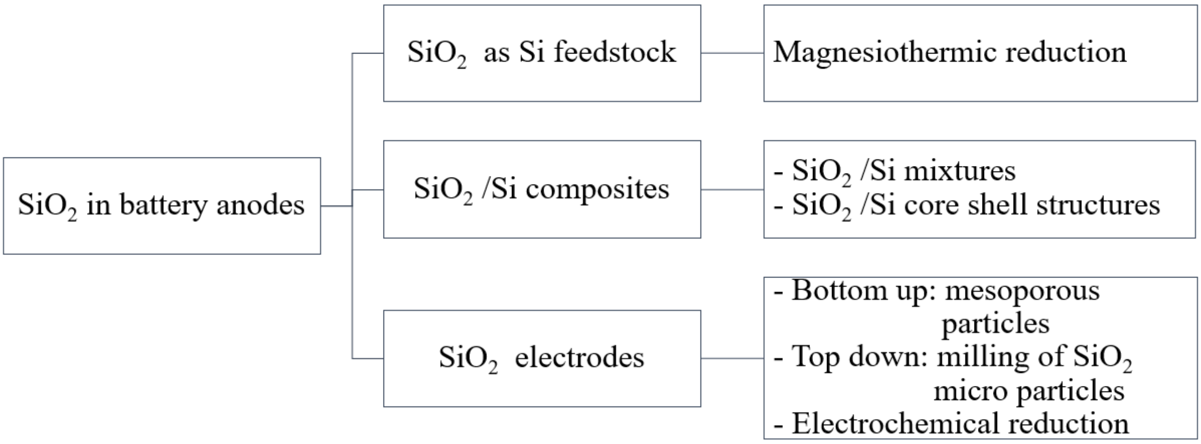

Fig. 2.4. Schematic illustration of the usage of SiO_2 as an anode material, replicated from ref.[17]

SiO_2 utilized as the main active material in anodes are mainly retrieved by either electrochemical reduction,[37] milling of SiO_2 microparticles,[9] or synthesis for porous SiO_2 structures by wet chemical methods.[38] In most cases carbon is added to further improve the performance of the electrode, this will be discussed further in section 2.5.3.

Of the different SiO_2 structures, the porous SiO_2 structures have been the most studied over the last years. These structures have generally shown a relatively high capacity, ranging from 247 mAhg^{-1} to ~1055 mAhg^{-1},[17] and good rate capabilities. Also, the cycling stability of porous SiO_2 is improved relative to Si and Si/SiO_2 anodes. The importance of the porosity and how this impacts the electrochemical results will be further discussed in section 2.5.4.

Milling of SiO_2 particles has also shown to be a good alternative. In 2012 Chang *et al.* achieved capacities up to 800 mAhg^{-1} (after 200 cycles at 100 mAg^{-1}) with < 300 nm SiO_2 particles milled from SiO_2 microparticles.[9]

2.5.2 Lithiation of SiO_2

Sun *et al.* was the firsts to propose a lithiation mechanism for SiO_2, thus a further expansion of the lithiation mechanisms by Guo and Chang *et al.* resulted in the following proposed mechanisms:[39 ,10 ,9]

$$5SiO_2 + 4Li^+ + 4e^- \rightarrow 2Li_2Si_2O_5 + Si \qquad 335 \ \mathrm{mAhg^{-1}} \tag{2.18}$$

$$2SiO_2 + 4Li^+ + 4e^- \rightarrow Li_4SiO_4 + Si \qquad 836 \ \mathrm{mAhg^{-1}} \tag{2.19}$$

$$SiO_2 + 4Li^+ + 4e^- \rightarrow 2Li_2O + Si \qquad 1673 \ \mathrm{mAhg^{-1}} \tag{2.20}$$

$$Si + 3.75Li^+ + 3.75e^- \rightarrow Li_{3.75}Si \qquad 3600 \ \mathrm{mAhg^{-1}} \tag{2.21}$$

The formation of $Li_2Si_2O_5$, Li_4SiO_4 and Li_2O provides structural support, buffering the volume expansions of the Si.

The lithiation potentials of SiO_2

The onset potentials of the different lithiation and delithiation reactions that are reported in the literature are varied. The onset potential is affected by different factors, such as particle size, crystallinity and electrode composition. An overview of some reported onset potentials for the lithiation and delithiation of SiO_2 is given in Table 2.2

Tab. 2.2. Reported experimental lithiation and delithiation potentials of different Si compounds found in the literature on SiO_2 anodes

Reaction	Potential [V]
Lithiation	
$5SiO_2 + 4Li^+ + 4e^- \rightarrow 2Li_2Si_2O_5 + Si$	0.27 [9]
$2SiO_2 + 4Li^+ + 4e^- \rightarrow Li_4SiO_4 + Si$	0.24 [9 ,10]
$SiO_2 + 4Li^+ + 4e^- \rightarrow 2Li_2O + Si$	0.72 [40]
$Si + 3.75Li^+ + 3.75e^- \rightarrow Li_{3.75}Si$	0.00, 0.24, 0.40 [9 ,10 ,40]
Delithiation	
$Li_2Si_2O_5 + Si \leftrightarrow 5SiO_2 4Li^+ + 4e^-$	0.27 [9]
$Li_{3.75}Si \rightarrow 3.75Li^+ + Si + 3.75e^-$	0.34 [9]

2.5.3 Carbon coatings and carbon additives

Surface coatings have proven to be an economic and feasible technology to improve the battery performance by modifying the surface chemistry or providing a protective layer to minimize the direct contact between the active material and the electrolyte.[41] The coating layer can improve the ionic or electronic conductivity, suppress phase transitions, increase the structural stability, favor the formation of the SEI film and decrease the electrode resistance, side reactions and heat generation during cycling. Thus, improving the cycle life, rate capability, reversible capacity and coulombic efficiency.[41] Carbon is superior to other coating materials due to its good electronic conductivity, in addition, carbon is one of the most abundant elements in the earth. Carbon precursors, such as sucrose and cornstarch, are used to form the carbon coatings.

SiO_2 possesses the lowest conductivity among the silicon oxide-based materials[42] and is regarded as a relatively poor electrical conductor. By coating the active particles with carbon the coating supplies fast electrons and can also be permeable for Li^+ ions from the surrounding electrolyte solution ensuring an effective diffusion of Li^+ and e^- into/out of the active particles and increasing the active area, as shown in Figure 2.5. The carbon coating also shortens the electronic transport length, given that all particles are fully coated, as the formation of agglomerates is reduced. Then, the electrons can pass along the outer side of the particle surfaces, forming a continuous transport path within the entire electrode, thus reducing the particle/particle interface resistance. This is shown in Figure 2.6.
The carbon coating also serves as an elastic shell around the particles improving the mechanical strength against volume expansion. In addition, carbon has very good chemical stability, and can therefore protect the active material against corrosion.[41]

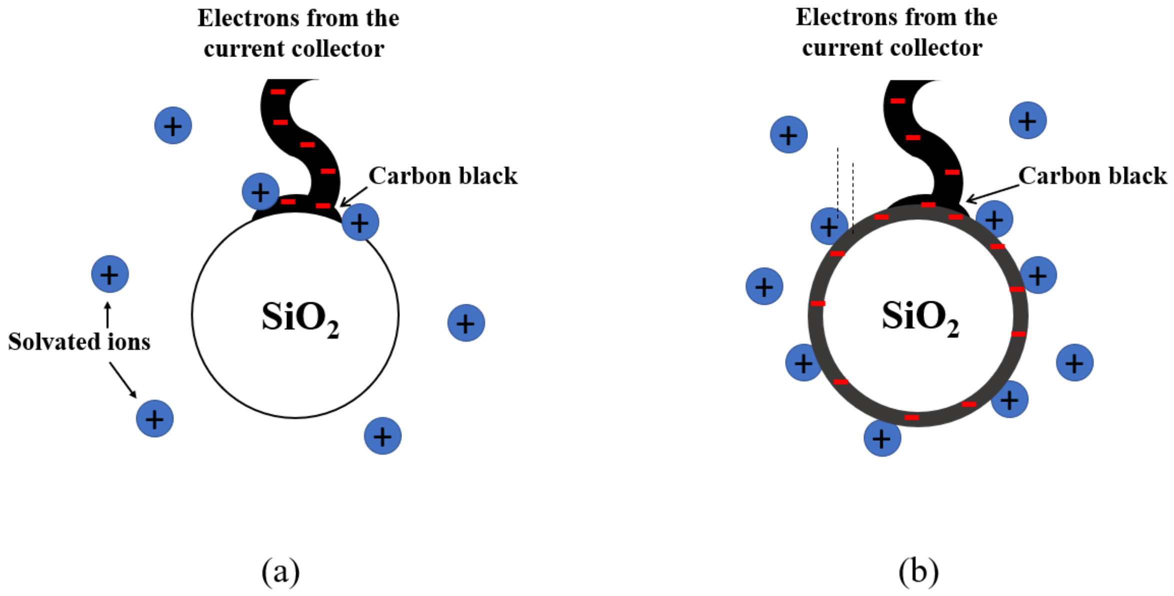

Fig. 2.5. Schematic illustration of the effect of carbon coating. (a) Electrons are supplied only through the point of contact between the active particle and the carbon black. (b) The carbon coating allows for an even distribution of electrons around the entire surface of the active particle. With inspiration from Li *et al.*[43]

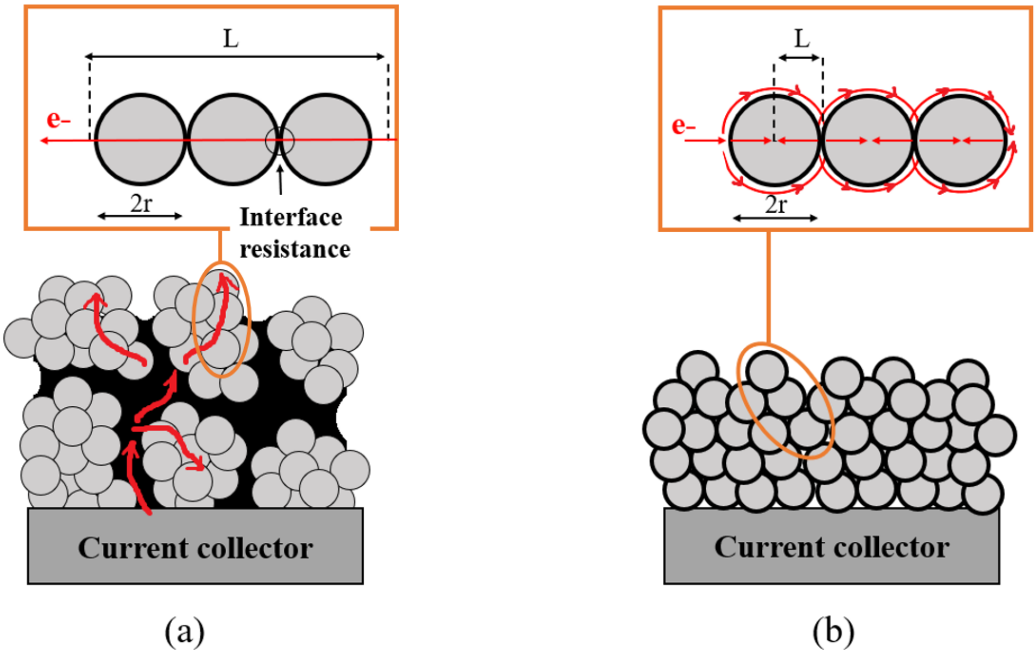

Fig. 2.6. Schematic representation of the electronic transport length (L) in the electrode: (a) without carbon coating; (b) with carbon coating. Recreated from Li *et al.*[43]

Carbon is also used as a conductive additive. For this purpose carbon black (CB) and graphene are mostly used. The conductive additive, which is homogeneously dispersed within the electrode to ensure "point-contact" between the active particle and one or more additive particle, allows for easy electron transport between the current collector and the active material, thus improving the conductivity of the electrode.[41]

2.5.4 Importance of porosity and particle size

A variety of nanoporous SiO_2 structures have been made in the last years, such as porous nanocubes[44] and porous nanospheres.[40] Porous structures are believed to be beneficial in several ways. The porous structures allow for easier electrolyte penetration into the electrode, as well as the diffusion path for Li^+ between the electrolyte and the active material is shorter.[44] In addition, the pores also help buffer the volume change during lithiation, preventing reformation of the SEI during cycling.[38]

However, there are also some disadvantages related to porous structures. The ICL for the first cycle is generally quite large with porous structures.[38] This capacity loss is mainly attributed to two things; the irreversible formation of lithium compounds, such as Li_2O and Li_4SiO_4, and the extensive SEI formation due to the high surface area. Also, the process of synthesizing these porous materials requires complex procedures and high-cost precursors, increasing the material production cost.[9]

Initially, SiO_2 was believed to be unsuitable for battery applications, as it was unreactive towards Li under battery conditions. However, since Gao *et al.* demonstrated the reactivity of 7 nm SiO_2 nanoparticles towards lithium, it has been believed that sufficiently small particle size is crucial for the SiO_2 electrode to be reactive.[35] Gao *et al.* explained that the theoretical reason for the increased reactivity with size reduction was given by the changes in the thermodynamic properties, where the ratio of surface to volume is greatly changed.[35]

2.6 SiO_2 from coscinodiscous diatoms

Coscinodiscus diatoms, an unicellular algae, have been researched for different applications, such as dye-sensitized solar cells and electroluminescent devices.[45] The diatoms have a skeletal shell of amorphous SiO_2, called a frustule, with a highly porous three-dimensional structure.[46] The nano-sized amorphous SiO_2 building blocks mainly consisting of spherical SiO_2 units, constructs patterned micro- and nano-structures to form new/larger frustules.[45]

The coscinodiscous diatom frustule, shown in Figure 2.7, consists of four main structures; cribellum, cribrum, areola and foramen. Losic *et al.* described the different parts of the frustules as given;[46] The cribellum is the outer part of the frustule and consists of a hexagonal array of pores with a pore size of ~45 nm. The cribellum covers the second structural layer which is twofold. The outer part is the cribrum and consists of hexagonally packed pores, with a size of ~200 nm in diameter. The foramen is the inner part and consists of large radially distributed holes with a diameter of ~1150 nm.

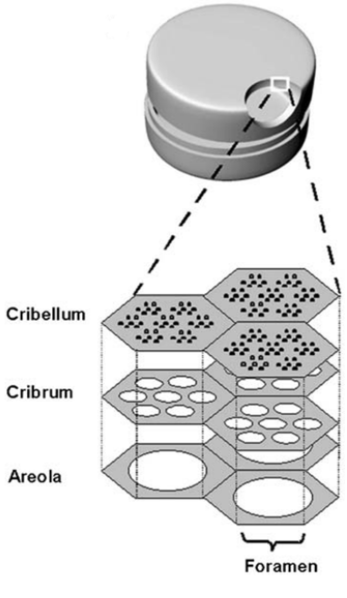

Fig. 2.7. Schematic of coscinodiscous frustule structure.

2.6.1 Diatoms in battery anodes

The diatom frustules display several desirable properties, as described in previous sections 2.5.4, such as the combination pf the mesoporous structure of the SiO_2 building blocks and the macroporous structure of the different layers of the frustule. In addition, the diatom frustules are environmentally friendly and advanced synthesis techniques/expensive precursors are not needed.

In 2019, Nordberg *et al.* achieved a capacity of 624 $mAhg^{-1}$ after 50 cycles with pristine milled SiO_2 from seawater diatom algae.[2] The current density was 50 $mAg^{-1}$for the first cycle and the electrochemical reduction step, and 200 mAg^{-1} for the subsequent cycles. The reported capacity has accounted for the contribution of the carbon black, and hence is only the contribution from the SiO_2 frustules.

2.7 Characterization techniques

In this section, a brief introduction to some of the experimental techniques used in this work is described.

2.7.1 Electrochemical characterization techniques

Galvanostatic cycling

Galvanostatic cycling is an electrochemical method for the characterization of galvanic cells. Parameters can be set to practical operating conditions to provide insight into the capacity and reversibility of a cell.

In galvanostatic cycling, the working electrode is subjected to constant current and the resulting potential is measured versus time. For lithiation of anode materials, the current is applied until an voltage limit V_1 is reached, before the current is reversed and applied until a voltage limit V_2 is reached.[17]
Figure 2.8 illustrates a characteristic plot of the potential as a function of capacity for an anode half cell. Here, the potential decreases rapidly, as a constant current is applied, until the lithiation potential is reached. The lithiation continues until the the current is reversed. As the constant current is reversed, the potential increases and stabilizes as the delithiation takes place, before rapidly increasing when all lithium stored in the electrode is released. The increase in voltage continues until either a new electrochemical reaction takes place, the current is stopped or the current is reversed. One cycle is now completed, and the process is repeated.

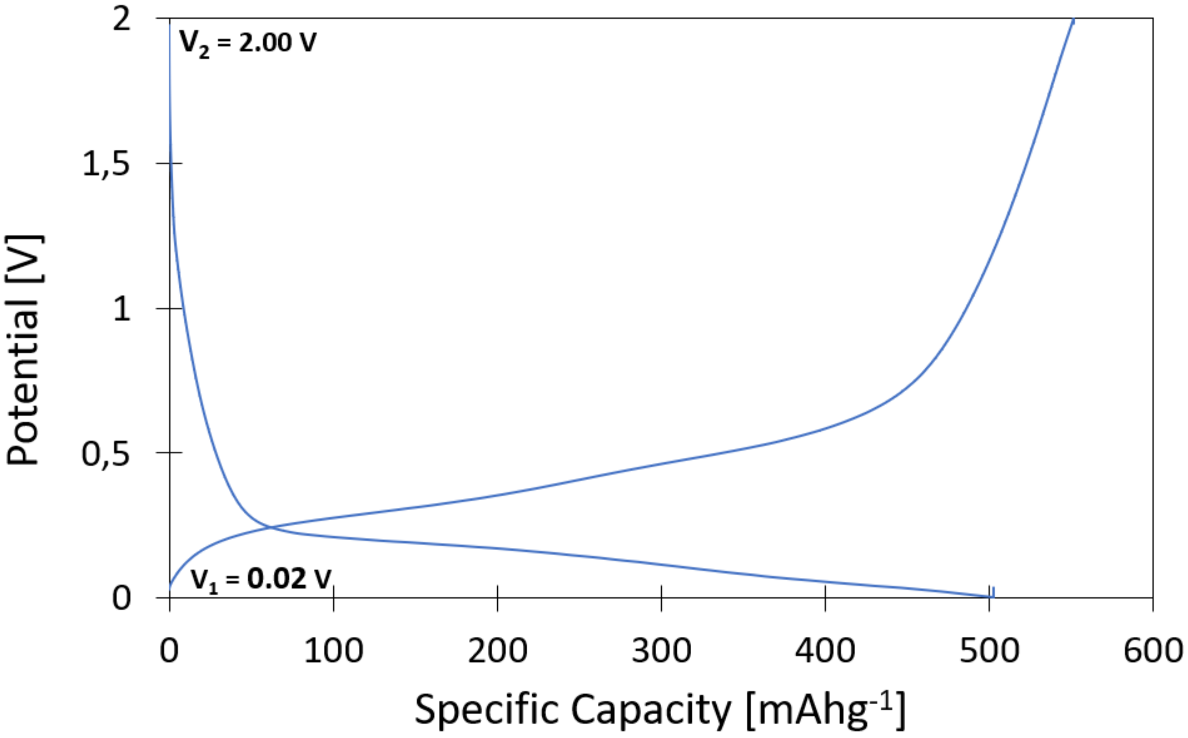

Fig. 2.8. Schematic of galvanostatic cycling. The higher cut-off potential is 2 V and lower cut-off potential is 0.002 V

Differential capacity analysis

The differential capacity curve, as shown in Figure 2.9, is the first derivative of a galvanostatic curve dQ/dV and can give an insight into the reactions occurring in a galvanic cell during galvanostatic cycling. The peaks in these plots correspond to sharp increases in charge at voltage plateaus in galvanostatic curves, whereas the area under the peaks corresponds to the charge related to the particular electrochemical reaction causing the plateaus. The potential at which a peak is located can thus be used to determine the presence of an electrochemical reaction.[17]

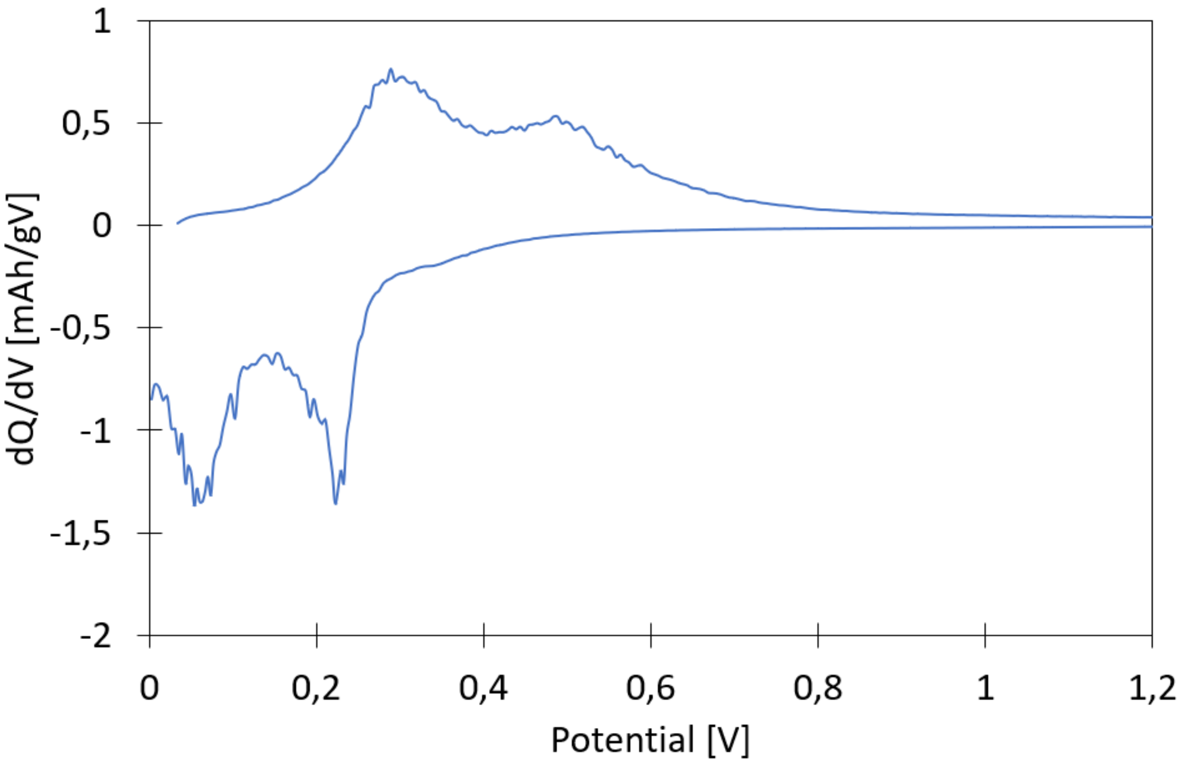

Fig. 2.9. Differential capacity curve

2.7.2 Structural characterization techniques

X-ray photoelectron spectroscopy

X-ray photoelectron spectroscopy (XPS) is a nondestructive analytical technique that gives information on elemental composition and the chemical bonding states of these elements. XPS spectra are obtained by measuring the kinetic energy spectrum of photoelectrons ejected from the specimen surface by the irradiating X-ray having constant energy, hv, in a vacuum.[47] The balance between hv and the kinetic energy of the photoelectron, E_k, is expressed as:

$$hv = E_K + E_B + \varphi \tag{2.22}$$

Where E_B is the binding energy of the electron to the nucleus relative to the Fermi level and φ is the work function of a specimen.[47]

XPS can be used to analyze the surface chemistry of the material, however, this method is restricted as the number of photoelectrons that can migrate to the outside of the specimen decreases with the penetration depth. Hence, XPS provides extremely weighted information of the outermost layer, but the measured data might also suffer from surface contamination.[47]

Scanning electron microscopy

The scanning electron microscope (SEM) is an extremely versatile instrument used for examination and analysis of the microstructure morphology and chemical composition characterizations.[48]

The SEM utilizes a focused electron beam to systematically scan across the surface of the specimen. An image is produced by collecting and processing the signals emitted from the sample surface. The main signals are the backscattered electrons (BSE), secondary electrons (SE) and the characteristic X-rays.
The secondary electron emission signal is the most widely used and is produced by the primary electron beam striking the sample surface and ionizes the specimen atoms, causing loosely bound electrons to be emitted. The secondary electrons have a low energy, (3-5 eV) and can therefore only escape from a region within a few nanometers into the material surface.[48] SEs are primarily used to obtain a topography contrast in the SEM.

Backscattered electrons are used to provide both compositional and topographic information in the SEM. The BSEs have undergone single or multiple scattering events, escaping from the surface with an energy greater than 50 eV. The amount of BSEs increases with increasing atomic number since elements with higher atomic numbers have a more positive charge on the nucleus, thus the backscatter signal is higher. Hence, the backscatter yielded, which is dependent on the atomic number, provides an atomic number contrast in the SEM images.[48]
BSEs are produced from a relatively large region, compared to the SEs, due to the fact that the high energy of the electrons prevents them from being absorbed by the sample.[48]

Focused ion beam

Focused ion beam (FIB) is a characterization technique used for site-specific analysis, ablation of materials and deposition. Today, most FIB systems are incorporated into SEMs, allowing you to operate both the SEM and FIB in the same chamber, providing an even more detailed characterization and manipulation of the material.[49]
The FIB uses an ion beam which is created by heating the ion source, most commonly gallium (Ga), whereas heated Ga flows and wets a tungsten needle. An electric field is applied to the needle tip, forming liquid Ga to a point source of 2-5 nm in diameter. The ions are accelerated through a potential down the ion column.[49]
When using FIB the interaction between the ion beam and the sample might significantly alter the morphology of the material. Thus, the interpretation of surfaces manipulated by an ion source must be performed with care.

2.8 Notes on full cells and half cells

In battery research, half cell configurations are most commonly used. Here, Li-metal is used as a counter electrode in the cell. The benefits of using half cells are twofold. First, the use of lithium metal as a counter electrode provides a nearly limitless source of Li^+ to the system. Second, by using the same counter electrode it is simpler to compare results in the literature. However, the use of half cells has some other implications that should be noted.

Li-metal has a low standard reduction potential. Hence, most anodes operate as a cathode in a half cell configuration, which is the case of SiO_2. However, materials that work as anodes in a full cell configuration will also be referred to as anodes in a half cell configuration.

By applying this, it is necessary to redefine some of the metrics defined in Section 2.2 to correlate to half cells.

$$\mathrm{CE} = 100\frac{Q_{ch}}{Q_{dis}} \tag{2.23}$$

$$\mathrm{ICL} = Q_{dis} - Q_{ch} \tag{2.24}$$

$$\mathrm{CCL} = \sum_{k} Q_{dis} - Q_{ch} \tag{2.25}$$

The use of half cells limits the study of compatibility between the anode materials, cathode materials and electrolytes. Other limitations that are crucial to be aware of with the use of half cells are the unrealistic abundance of Li^+ in the context of full cells. In full cells, there is a limited amount of Li^+ available, thus, consumption of Li^+ might lower the capacity of a full cell.

Chapter 3: Experimental

3.1 Overview

In this section, a detailed description of the procedures carried out in this work is given. The experimental techniques and equipment are also accounted for. The experimental work was carried out in steps, where the preparation of the silica and the active material was conducted in the first step. In the second step, the coin cells were assembled. The final step consisted of electrochemical and structural analysis of the electrodes before and after cycling.

3.2 Preparation of the active material

The SiO_2 used in this project was derived from diatom frustules, supplied from Plantonic AS. The diatom frustules are delivered in bags containing a mixture of seawater, algae and other impurities. Thus, the as received diatom frustules goes through a series of procedures, including washing, calcination, milling and coating, to obtain the properties needed for battery applications.
The main processing steps, described in this section, are based on the experimental processes carried out in the project preceding this thesis, withe some modifications.[1]

3.2.1 Initial treatment of as-received diatoms

1. As received diatoms from Planktonic were poured into a beaker and weighed, for the sole purpose of knowing how much algae compared to water and other impurities each bag contained. It was also desirable to know how much of the material that was lost in the different steps of the process.

2. The beaker was left for 1 h so that the oil, water, and diatoms separated in the beaker.

3. The oil and water was poured off, and the remaining water and diatoms were separated using a 36 µm mesh sieve.

4. The diatoms were dried in the oven, first at 90 °C for 24 h then at 150 °C for another 24 h.[17]

Fig. 3.1. As received diatom frustules, after being drained.

3.2.2 Washing and calcination of diatoms

The SiO_2 frustules were washed and calcined to get rid of the organic and inorganic substances. Washing of the frustules was conducted to remove water-soluble inorganic substances, such as NaCl, while calcination was carried out to remove organic impurities. The washing and calcining of SiO_2 was conducted according to the following scheme:[17]

1. The dried diatoms were rinsed with DI-water and added to a large beaker. The mass ratio of diatoms to water was 1:100.
2. The beaker was placed on a hotplate with a magnetic stirrer for 2 h at 130°C and 450 rpm. The beaker was covered with aluminum foil to ensure that the beaker/solution was evenly heated and to prevent the solution from boil over.
3. A 36 µm sieve was used to separate the water and diatoms. The diatoms were rinsed with DI-water.
4. The diatoms were transferred back into the beaker and DI-water was added so that the mass ratio of diatoms to water was 1:100.
5. The solution was sonicated for 30 min at room temperature (25 °C).
6. A 36 µm sieve was used to separate the water and diatoms after sonication. The diatoms were washed with flowing DI-water for 5 min.
7. Finally, the diatoms were dried in a drying cabinet at 90 °C for 24 h, before the temperature was increased to 150 °C for another 24 h. The reason for drying the diatoms in several steps was to prevent the water, still adhered to the diatoms, from boiling.
8. The diatoms were calcined at 650 °C for 2 h in flowing synthetic air atmosphere (80 Lh^{-1}) to remove any remaining organic compounds, forming pure nanostructured SiO_2.

3.2.3 Milling of diatom frustules:

As received the diatoms had a particle size greater than 36 µm. Milling of the diatoms was conducted to reduce the particle size of the frustules, as results from previous work, carried out in the project preceding this thesis, indicated that milling of SiO_2 increased the external surface area, thus increasing the contact points between SiO_2 and Li^+.[1] One of the reasons for choosing milling as an experimental technique for reducing the size of the particles was that it is easy to upscale.

Wet ball milling was carried out in the planetary mill (RETSCH PM100). SiO_2 was added to a tungsten carbide (WC) beaker together with WC-balls with a diameter of 3 mm. The ball to powder ratio between the WC-spheres and SiO_2 was 20:1, as 2 g of SiO_2 and 40 g of WC-balls was used. To achieve good mixing and even dispersion, 8 mL of ethanol was added to the WC-beaker. The milling was conducted with the following steps for 3 h:

1. Milling with 400 rpm for 10 min clockwise. Rest for 1 min.
2. Milling with 400 rpm for 10 min counterclockwise. Rest for 1 min.

3.2.4 Carbon coating

In this project, the electrochemical performance of electrodes fabricated from pristine silica, as well as carbon-coated silica, were compared. The procedure for carbon coating is described below.

Glucose (SIGMA-ALDRICH) was used as a carbon precursor with the ratio 40 wt% : 60 wt% between glucose and SiO_2 respectively. This composition was chosen based on the results, from previous work carried out in the project preceding this thesis, where a coating with 20 wt% glucose was not sufficient to coat the entire surface of the particles, whereas a coating with 60 wt% glucose resulted in a to thick carbon-coating[1]

The carbon coating was made by dissolving glucose in DI-water. When the glucose was dissolved SiO_2 was added to the mixture and stirred gently. The mixture was then sonicated for 30 min, to ensure an even coating of all SiO_2 atoms.

After sonication, the mixture was placed on a hotplate with a magnetic stirrer at 70 °C and 300 rpm to evaporate the water added to the glucose. The mixture was kept on the hotplate until almost complete evaporation, and finished by hand in a mortar until complete evaporation of the water. The coated SiO_2 was then annealed with an argon flow of 80 cm^3/h at a heating rate of 3 °C/min and a holding time of 6 h at 850 °C. During the annealing the glucose reacted with the air, at a temperature around 600 °C, leaving a pure carbon layer around the particles. CO_2 and H_2 gas were released during the annealing as reaction products.

3.3 Slurry preparation and casting

SiO_2 electrodes used in this thesis were prepared by mixing 75 wt% of active material, 15 wt% of alginate binder and 10 wt% of carbon black. In addition, 0.05 g of isopropyl alcohol was added to obtain a higher viscosity and a more homogeneous slurry. To make the electrode slurry, carbon black and alginate binder were first mixed in Retsch Shaker 400 MM for 4 min at 25 Hz. Then, the active material and IPA were added and blended in Retsch Shaker 400 MM for 45 min at 25 Hz. The resulting slurry was cast onto an 18 µm thick copper foil and air-dried.
The alginate binder used in the electrode slurry was prepared by mixing Sigma alginic acid sodium salt (from brow algae) and DI-water (with a ratio of 1:60 powder to water) on a hotplate at 60 °C and 500 rpm for ~ 3 h (until all of the powder were dissolved).

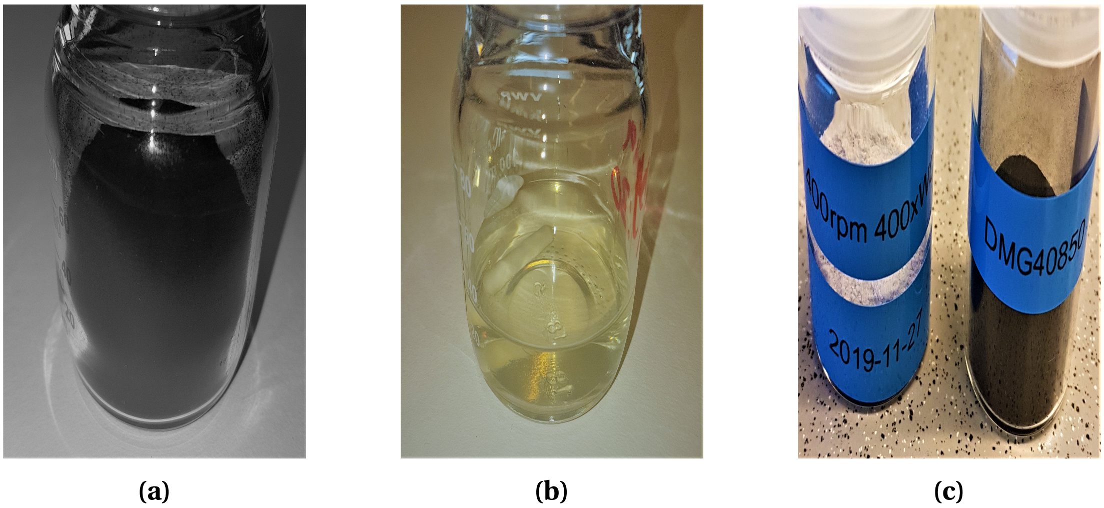

(a) **(b)** **(c)**

Fig. 3.2. (a) carbon black, (b) alginate binder and (c) silica powder, without carbon coating to the left and with carbon coating to the right.

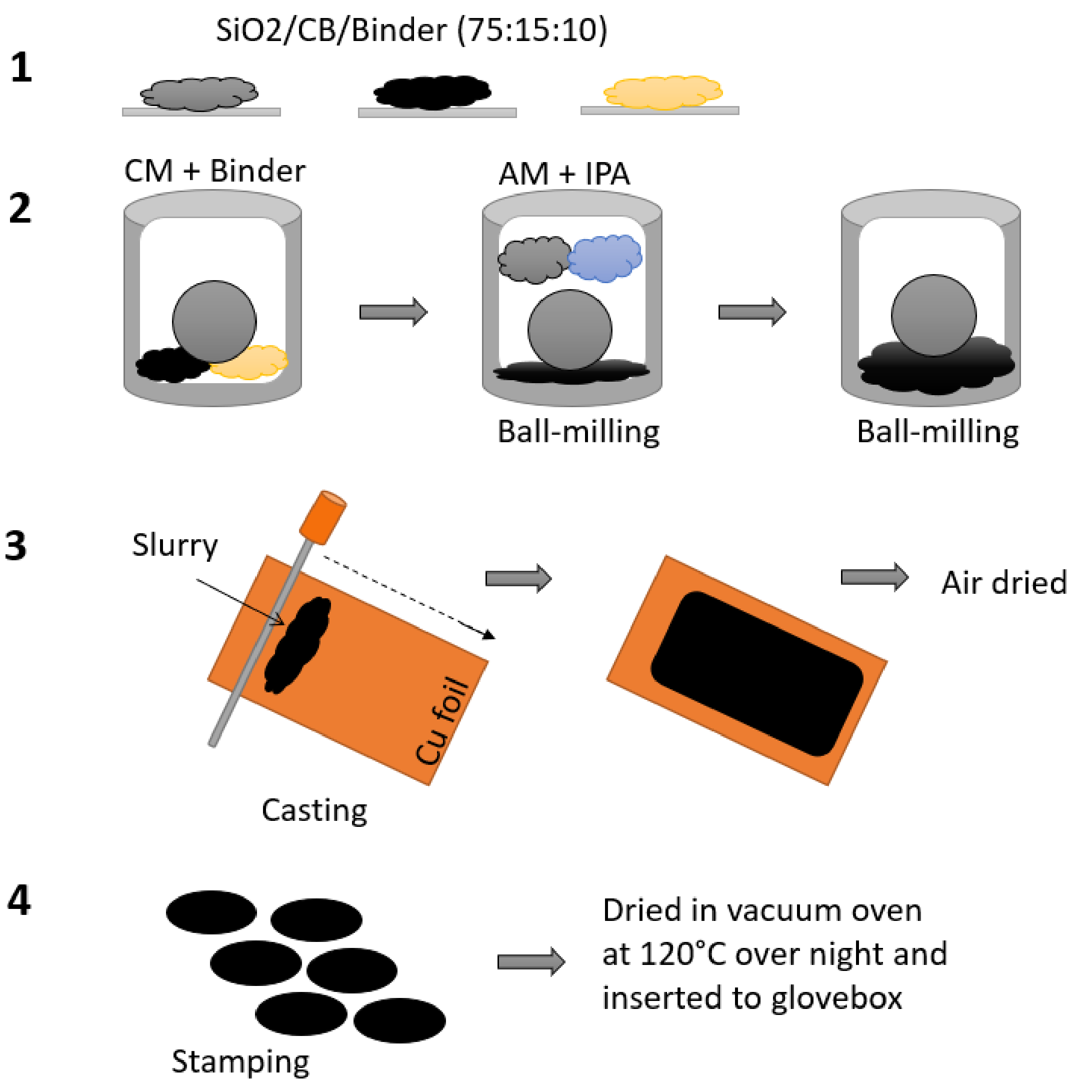

Fig. 3.3. Illustration of the slurry- and electrode preparation.

3.4 Electrolyte preparation

Two electrolytes were used in this thesis, $LiPF_6$ and LiFSI. A 1M $LiPF_6$ in 50:50 vol% EC:DEC electrolyte (1.0 M $LiPF_6$ in EC/DEC = 50/50, battery grade, Sigma Aldrich) and an 1M LiFSI in 50:50 vol% EC:DEC electrolyte was prepared.

The 1M LiFSI electrolyte was prepared in a glove box (Labmaster SP, Mbraun) under an argon atmosphere, with H_2O and O_2 levels below 0.1 ppm. EC (SIGMA-ALDRICH Ethylene carbonate, anhydrous, 99%) and DEC (SIGMA ALDRICH, diethyl carbonate anhydrous > 99%) were added in a polytetrafluoroethylene coated aluminum flask, then LiFSI salt (American elements, >99.9%) was added to the solvent mixture. The electrolyte mixture was then stirred for a couple of minutes on a hotplate until the salt was completely dissolved.

Tab. 3.1. Overview of electrolytes

Nomenclature	Composition
$LiPF_6$	1M $LiPF_6$ EC:DEC 50/50 vol%
LiFSI	1M LiFSI EC:DEC 50/50 vol%

3.5 Coin cell assembly

Coin cell parts were supplied by Hohsen Corp. (CR2016, 20 mm diameter and 1.6 mm height). A general schematic of a coin cell and the different components can be seen in Figure 3.4. A full overview of the cells assembled is given in the Appendix section A.2.

The electrodes were heat-treated in a vacuum drying chamber (Binder VD 23) at 120°C in vacuum over night before introduced into the glow box, to get rid of humidity or impurities. Before assembly, all electrodes were weighed against a reference copper foil disk, so that the active material could be calculated.
The 12 mm diameter anodes were placed in the cell bottom, which was fitted with a gasket. 15 µL of electrolyte was then ejected onto the middle of the electrode before a separator (Celgard, 25 µm thick) was placed on top of the electrolyte, and then another 15 µL of electrolyte was ejected on top of the separator. A 14 mm diameter Li metal counter electrode was punched out from a Li-foil (99.9%, 0.75 mm thick, Alfa Aesar) and brushed on both sides, to remove any surface films, before pressed onto a 16 mm diameter stainless-steel spacer (CR 2016, 0.3 mm thick, Hohsen corp.). The Li metal counter electrode was placed on top of the separator, with the lithium facing the electrolyte. Finally, the cell cap was placed on top and the cell was hermetically sealed using a crimping machine (Automatic crimping machine, Hohsen Corp.).

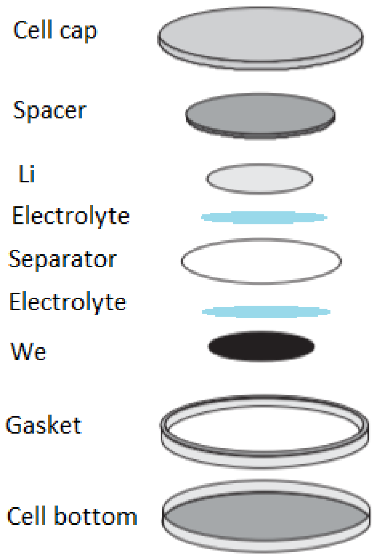

Fig. 3.4. Schematic of coin cell and the order of the different cell components. With modifications from Burns *et al.*[50]

3.6 Electrochemical characterization

Previous to the electrochemical characterization all cells were rested for 30 min to allow the electrolyte to penetrate the porous electrodes.

3.6.1 Galvanostatic cycling

Prior to galvanostatic cycling, the cells were subjected to an activation procedure. The activation procedure consisted of lithiation to 2 mV with potentiostatic holding for 48 h and delithiation up to 2 V with potentiostatic holding for 24 h. This step was repeated 5 times. The activation was conducted with a current density of 50 mAg^{-1}. After the activation steps normal cycling from 2 mV to 2 V at 100 mAg^{-1} was conducted. The coin cells were cycled galvanostatically in two galvanostats: BioLogic BSC 805 and BioLogic VMP3. The electrochemical data was processed in EC-Lab.
To study the formation of the SEI a batch of cells was stopped in the 2^{nd} activation step, as illustrated in Figure 3.5, to determine from which stage the formation of the SEI was visible. Another batch of cells was stopped at different potentials during the first discharge to study the formation of SEI and the electrolyte decomposition products with the use of XPS. Finally, the remaining cells were cycled until they achieved 80 cycles, to compare the structural changes of the different cells after long term cycling.

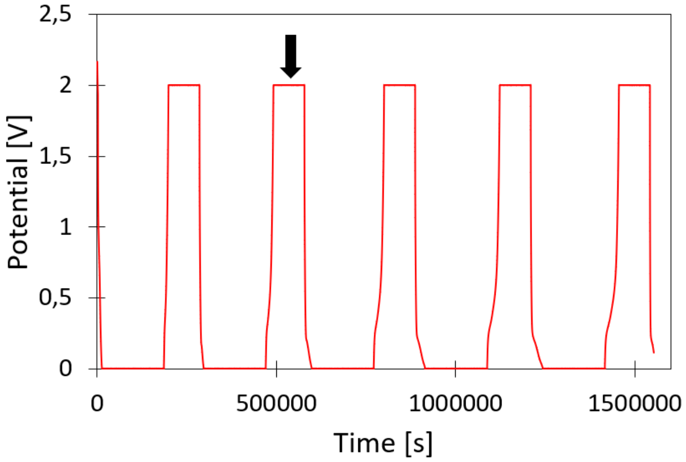

Fig. 3.5. Cycling process of cells designed to study the SEI formation. The black arrow indicates where in the activation procedure the cells were stopped.

3.7 Structural characterization

Postmortem characterization was conducted on selected electrodes. The electrodes were collected by disassembly of coin cells in a glove box, where they were rinsed with DMC and dried. All electrodes were stored in the glove box until use, to minimize contamination.

3.7.1 X-ray photoelectron spectroscopy

In-House X-ray photoelectron spectroscopy (XPS) measurements were carried out on the SiO_2 cells presented in Table 3.2 with Kratos Axis Ultra using a focused monochromatized Al Kα radiation (hν = 1486.6 eV) operating at 100 W. The analyzed area of the samples was 300x700 μm^2 and the pressure in the analysis chamber was $\sim 10^{-9}$ Torr. In addition, the pass energy was 20 eV and charge neutralization with low-energy electrons were used. To prevent the samples from being exposed to moisture/air during transfer an inert transfer arm was used. Short-time spectra were recorded, so that any possible degradation during measurements could be detected. The binding energy scale was calibrated with the hydrocarbon C 1s peak at 285.0 eV. Core peaks were analyzed using CasaXPS software, using a nonlinear Shirley-type background, and peak positions and areas were obtained by a weighted least-squares fitting of model curves (70% Gaussian and 30% Lorentzian combination).

Tab. 3.2. Cells for XPS measurements. The potential indicates the potential at which the cells were stopped during the very first discharge (lithiation)

Cells	Potential [V]
SiO_2-LiFSI	0.5
SiO_2-LiFSI	0.2
SiO_2-$LiPF_6$	0.5
SiO_2-$LiPF_6$	0.2

3.7.2 Focused ion beam cross-section analysis

The focused ion beam (FIB) was used to make cross-sections of electrodes to study the changes in morphology. When making the cross-section a carbon layer of size 35 µm x 5 µm x 6 µm were deposited using a current of 6.1 nA. Then a regular cross-section, approximately 5 µm below the carbon deposited layer, of size 30 µm x 20 µm x 10 µm with current 21 nA were made. To finish, a cleaning cross-section of size 30 µm x 10 µm x 10 µm was made overlapping the carbon deposited layer and the regular cross-section with a current of 21 nA and another cleaning cross-section of size 30 µm x 5 µm x 10 µm with current 6.1 nA overlapping the first cleaning cross-section and the carbon deposited layer. When using the ion source an acceleration voltage of 30 kV was used. To acquire good pictures of the structure and cross-section the secondary electron microscope feature of the FIB was used, with 2 kV and 43 nA in immersion mode.

FIB analysis was conducted on pristine electrodes as well as electrodes from cells stopped at the second activation step, as indicated in Figure 3.5.

3.8 Report terminology

This sections gives a short overview of terminologies used in this report

- **Reference for potentials:**
  All potentials are given vs Li/Li$^+$ unless otherwise is stated.
- **Use of the word active material:**
  Active material will in this work describe all material in the electrode which is not the binder nor conductive additives, i.e. the active material is defined as the amount of SiO_2 or the amount of carbon-coated SiO_2.
- **Use of the word capacity:**
  The word capacity will in this work refer to the specific charge capacity of a cell (the capacity during delithiation) unless otherwise is stated. The specific charge capacity is normalized to the active material in the cell. Hence, the weight of the binder and the conductive additives are not accounted for.
- **Naming conventions for cells:**
  The naming convention for different casts and cells used in this work is presented in Table 3.3. For the active material, the C in SiO_2/C indicates that the SiO_2 particles are carbon-coated.

Tab. 3.3. Overview over the combinations of active material and electrolytes

Active material	Electrolyte	Nomenclature
SiO_2	LiFSI	SiO2-LiFSI
SiO_2	$LiPF_6$	SiO2-LiPF6
SiO_2/C	LiFSI	SiO2/C-LiFSI
SiO_2/C	$LiPF_6$	SiO2/C-LiPF6

Chapter 4: Results

4.1 Overview

The results in this chapter are divided into three main parts. First, the results from the electrochemical characterization of SiO_2 and SiO_2/C anodes by galvanostatic cycling are presented. The goal of this part is to determine the difference in the performance of cells with LiFSI and $LiPF_6$ containing electrolytes. This part is followed by XPS of SiO_2 anodes stopped at different potentials during the first lithiation. The aim of this is to better understand the formation of the SEI and how this corresponds with the electrochemical data. Finally, postmortem analysis was conducted by SEM and FIB cross-section.

4.2 Electrochemical characterization

4.2.1 Galvanostatic cycling - activation

With the aim of triggering silica reaction towards lithium, the electrodes were subjected to an electrochemical activation process. The activation treatment consisted in a sequence of galvanostatic and potentiostatic steps, using a voltage window of 0.002 V and 2 V. The evolution of the voltages with time upon electrochemical activation is depicted in Figure 4.1. As it can be seen from the Figure, each galvanostatic step is followed by a potentiostatic hold step. The duration of the potentiostatic hold step is of 48 h after discharge and 24 h after charge.

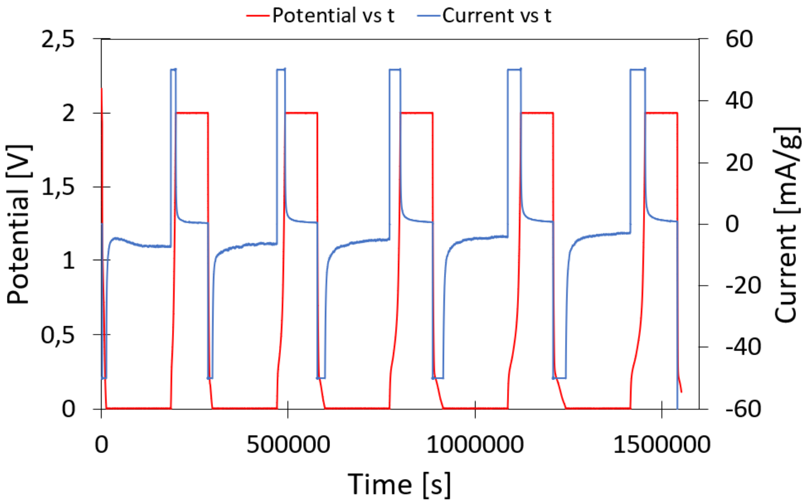

Fig. 4.1. Galvanostatic activation procedure, showing the galvanostatic cycling and the potentiostatic hold steps.

Specific capacity activation

The specific capacity plots for the cells during activation can be found in Figure 4.2. The initial specific capacity values are significantly higher for the cells with carbon-coated SiO_2 than the cells with "pure" SiO_2, i.e. 384 $mAhg^{-1}$, 440 $mAhg^{-1}$, 697 $mAhg^{-1}$ and 698 $mAhg^{-1}$ for SiO_2-$LiPF_6$, SiO_2-LiFSI, $LiPF_6$/C-$LiPF_6$ and SiO_2/C-LiFSI respectively. The general trend is that the coulombic efficiency increases with the cycle number. Moreover, the difference between lithiation and delithiation decreases with increased cycle numbers for all cells, an thus the coulombic efficiency increases. A common trend seen in all cells is that the delithiation specific capacity always has an increasing trend, i.e. the charge is always increasing. Figures 4.2a and 4.2b shows that for SiO_2 anodes LiFSI yields higher lithiation capacity than $LiPF_6$, i.e. 716 $mAhg^{-1}$ and 655 $mAhg^{-1}$ respectively. The opposite is seen in Figures 4.2c and 4.2d for the carbon-coated SiO_2 anodes, where $LiPF_6$ reaches a higher lithiation capacity than LiFSI, i.e. 1006 $mAhg^{-1}$ and 950 $mAhg^{-1}$ respectively, during the activation.
When studying the coulombic efficiency with regards to the electrolyte, LiFSI is found to yield a higher coulombic efficiency at the end of the galvanostatic activation for both SiO_2 and carbon-coated SiO_2, 83% and 95% respectively, whereas $LiPF_6$ yielded a coulombic efficiency of 82% and 92% for SiO_2 and carbon-coated SiO_2, respectively.

In Figure 4.2d the lithiation capacity for SiO_2/C-LiP_6 decreases from the first cycle to the second cycle, before it increases rapidly in the next cycle and continues to increase throughout the remaining cycles of the activation. A somewhat similar trend can be seen in Figure 4.2c, where a rapid increase in the capacity of the lithiation is seen from the second cycle to the third cycle. This phenomenon is not observed in the specific capacity plots of SiO_2 anodes, given in Figure 4.2a and 4.2b. Here, the lithiation capacity slowly increases throughout all cycles of the activation.

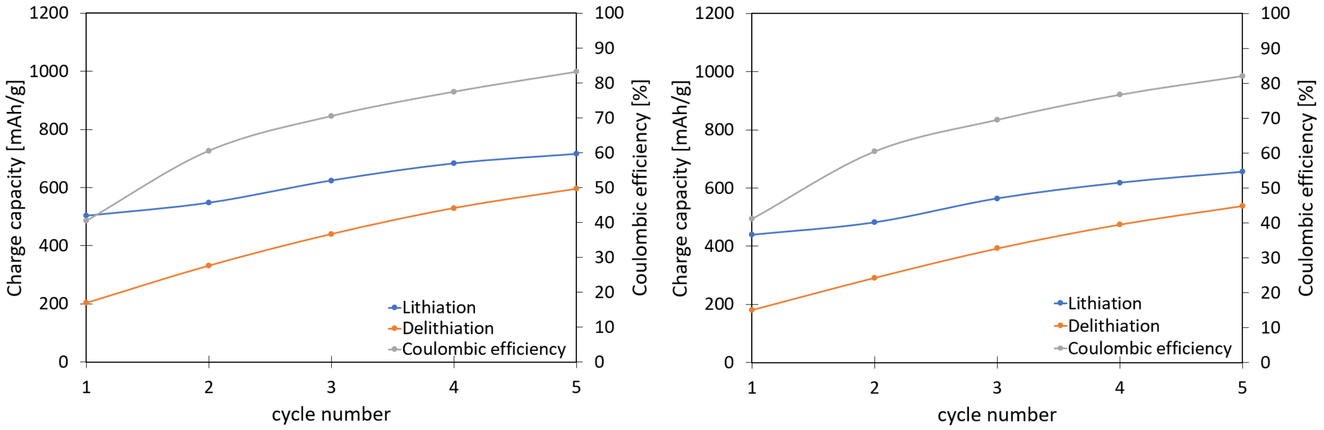

(a) SiO_2 with LiFSI **(b)** SiO_2 with $LiPF_6$

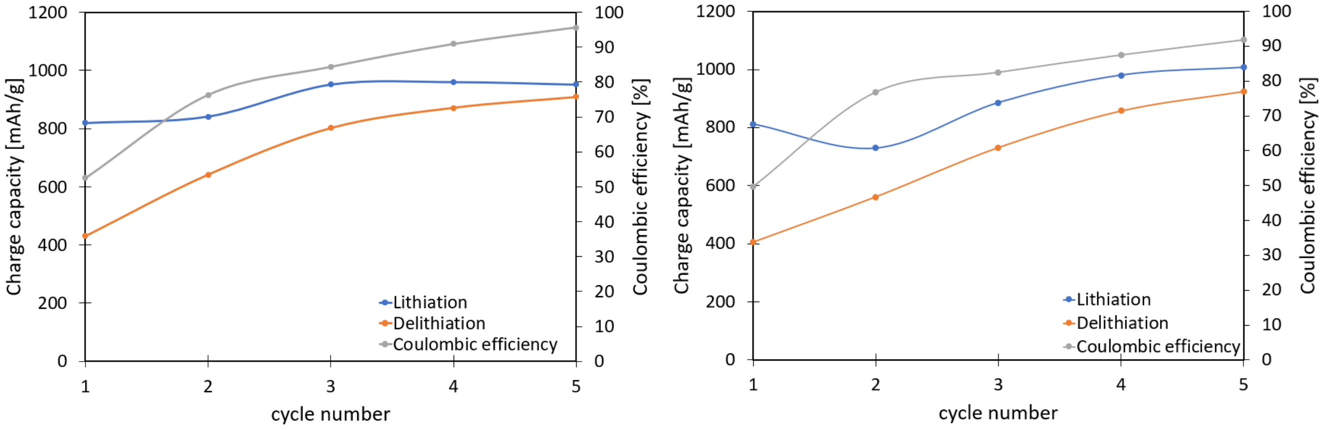

(c) SiO_2/C with LiFSI **(d)** SiO_2/C with $LiPF_6$

Fig. 4.2. Specific capacity of SiO_2/C during galvanostatic activation.

Voltage profiles

In Figure 4.3, representative voltage profiles recorded upon electrochemical activation of the four different cells are presented. A general trend is found for all material systems, whereas in the first lithiation cycle, plateaus are initiated at approximately 1.0 V and 0.68 V for SiO_2 cells and approximately 1.25 V and 0.70 V for carbon-coated SiO_2.

As seen in Figures 4.3a and 4.3b, the voltage profiles of the two SiO_2 cells with different electrolytes are very similar. Here, the potential of the lithiation curves, not applying for the first cycle, rapidly decrease until a kink in the slope is observed at ~ 0.17 V before a flatter plateau is initiated. For the delithiation curves of the SiO_2 cells, a rapid increase in potential is seen from 0.02V to ~0.2 V. Then, a flatter plateau is initiated before the potential rapidly increases again from ~ 0.5 V to 2.0 V. The duration of these flatter plateaus is seen to increase with increasing cycle number. The initial capacity of the SiO_2 cell with LiFSI was 180 $mAhg^{-1}$ whereas the final capacity gained was 548 $mAhg^{-1}$, giving a capacity increase of 368 $mAhg^{-1}$ during the activation. For the SiO_2 cell with $LiPF_6$ the initial capacity was 158 $mAhg^{-1}$ whereas the final capacity was 490 $mAhg^{-1}$, giving a capacity increase of 332 $mAhg^{-1}$ during the activation.

For the carbon-coated SiO_2 cells, presented in Figures 4.3c and 4.3d, the potential of lithiation cycle 2 - 5 decreases rapidly from 2.0 V to ~ 0.9 V. At ~ 0.9 V a flatter plateau is initiated and the potential decreases slowly until the lower potential 0.02 V is reached. For the delithiation curves, a rapid increase is seen from 0.02 V to ~0.2 V before a flatter plateau is initiated. At ~ 0.5 V the potential starts to increase more rapidly until the upper potential limit, at 2.0 V, is reached. As seen for the SiO_2, the duration of the flatter plateaus increases with increasing cycle number. The initial capacity of the carbon-coated SiO_2 anode with LiFSI was 390 $mAhg^{-1}$ whereas the final capacity was 846 $mAhg^{-1}$, giving a capacity increase of 456 $mAhg^{-1}$ during activation. For the carbon-coated SiO_2 anode with $LiPF_6$ the starting capacity was 368 $mAhg^{-1}$ whereas the final capacity was 862 $mAhg^{-1}$, giving a capacity increase of 494 $mAhg^{-1}$ during the activation.

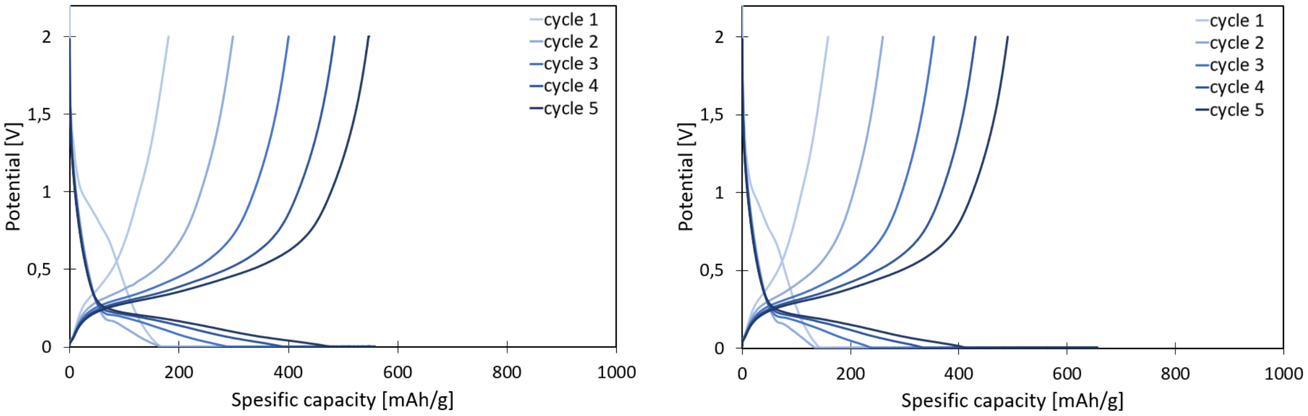

(a) SiO_2 with LiFSI

(b) SiO_2 with $LiPF_6$

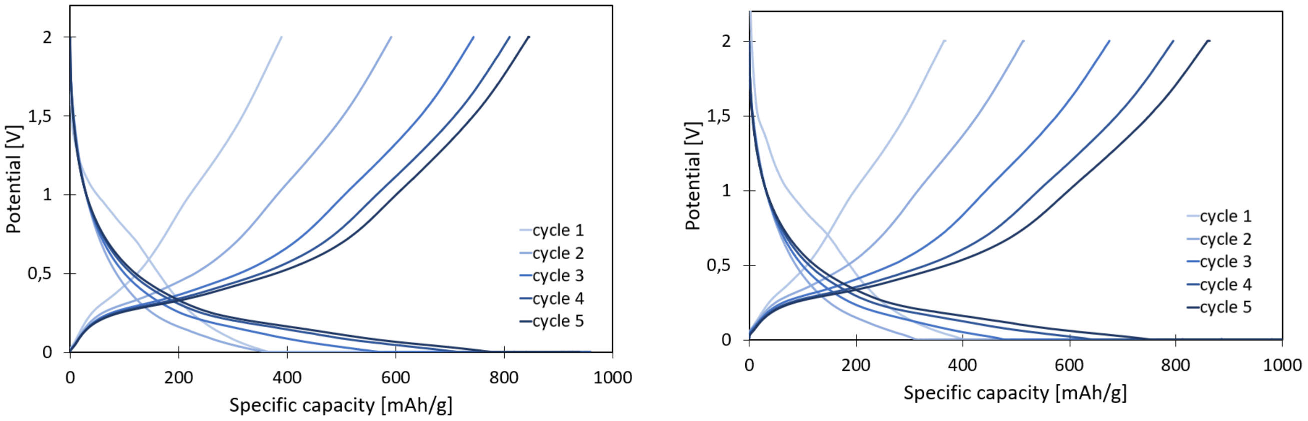

(c) SiO_2/C with LiFSI

(d) SiO_2/C with $LiPF_6$

Fig. 4.3. Voltage profile of SiO_2 and SiO_2/C during galvanostatic activation.

Differential capacity analysis - activation

Differential capacity plots from the activation of the selected cells are presented in Figure 4.4. A general trend is found within all material systems, i.e in the first cycle all cells exhibit broad peaks at ~0.6 V and 1 V, which are attributed to the SEI formation. Then, two oxidation peaks and two reduction peaks emerge and grow upon cycling. These peaks are characteristic to silicon alloying/dealloying reactions. Interestingly, the position of the center of these peaks shift from one cycle to another. The onset potential of the oxidation peaks shifts towards a lower potential, while the onset potential of the reduction peaks is shifted towards a higher potential. Also, the difference in the differential capacity between oxidation and reduction peaks is smaller for SiO_2 anodes than for carbon-coated SiO_2 anodes.

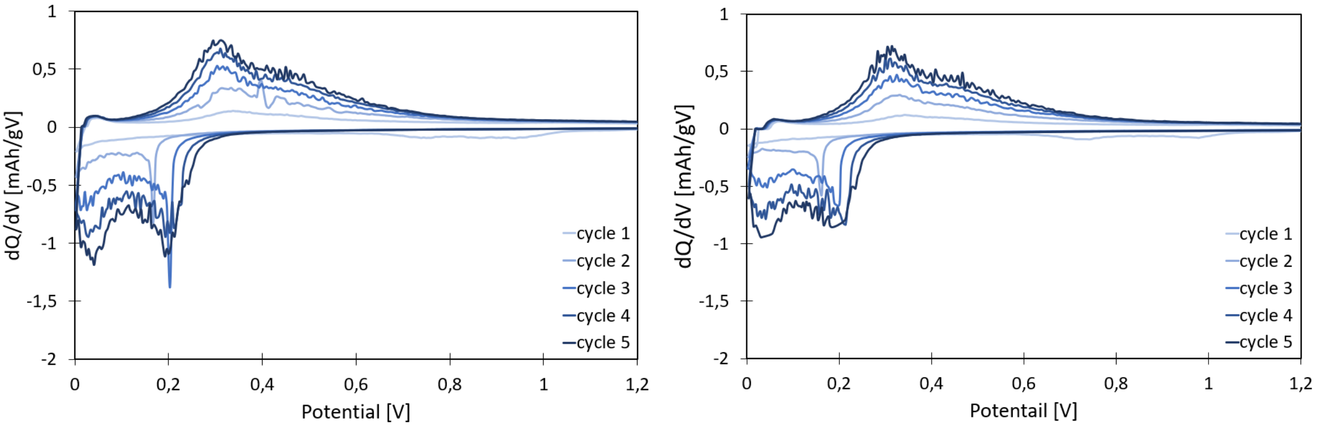

(a) SiO_2 with LiFSI **(b)** SiO_2 with $LiPF_6$

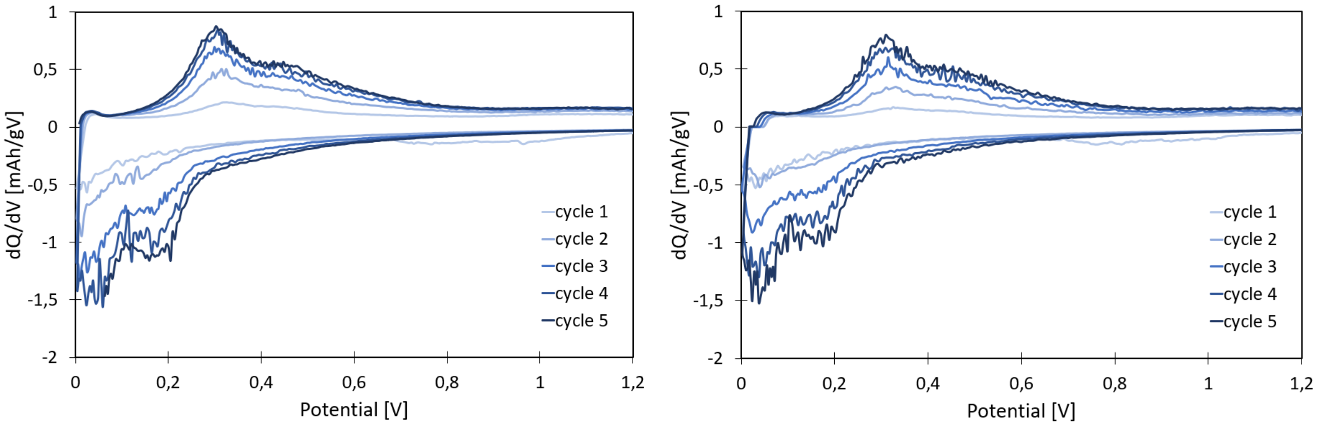

(c) SiO_2/C with LiFSI **(d)** SiO_2/C with $LiPF_6$

Fig. 4.4. Differential capacity of SiO_2/C during galvanostatic activation.

4.2.2 Long-term cycling

When the cells proceed into long-term cycling, after the potentiostatic activation, the current was changed from 50 mAg^{-1} to 100 mAg^{-1}. The increase in the charge/discharge rate can affect the delivered capacity, because discharge of half cells at high rates reduces the amount of energy that can be extracted from the system, thus lowering the capacity. Hence, cycle 1, which is the first cycle after the current change, will not be considered when comparing the voltage profiles of the cells during cycling.

Specific capacity

The capacity curves can be seen in Figure 4.5. For both SiO_2 cells, presented in Figures 4.5a and 4.5b the capacity increases with increasing cycle numbers. This is not the case for the carbon-coated SiO_2 cells, presented in Figures 4.5c and 4.5d. Here, the capacity of the carbon-coated SiO_2 cell with LiFSI decreases with increasing cycle number, while the capacity of the carbon-coated SiO_2 cell with $LiPF_6$ increases with increasing cycle number at first, before stabilizing at ~30th cycle. Regarding the coulombic efficiency, an increase is seen for all systems from the first cycle after activation to the second. From the second cycle and throughout the cycling, the coulombic efficiency is high, i.e. ~99%, and relatively stable for all systems. The only exception is seen in Figure 4.5d for SiO_2/C-$LiPF_6$, where the coulombic efficiency fluctuates somewhat between cycle 47 - 64. However, the coulombic efficiency never decreases below the value of 98.6%.

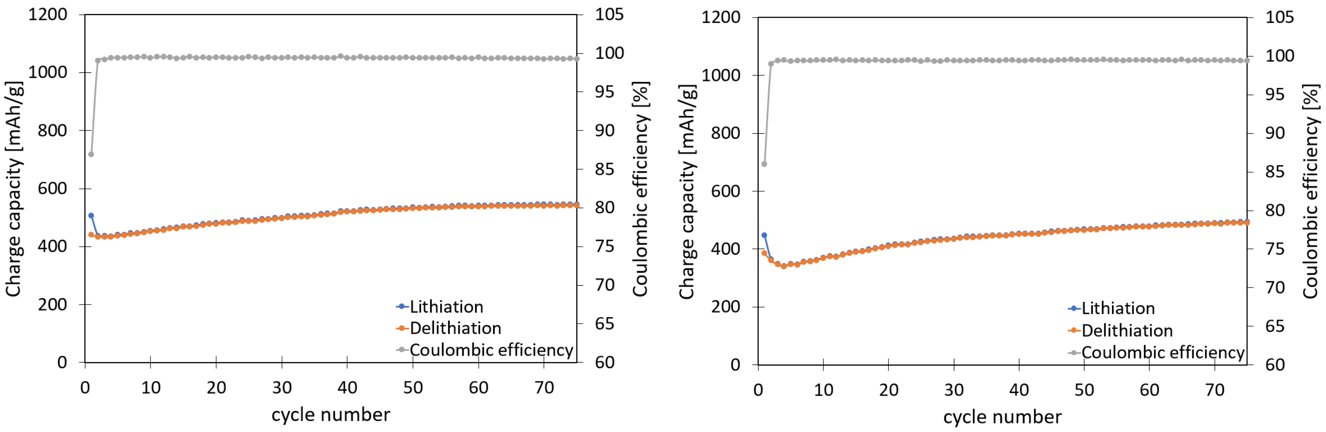

(a) SiO$_2$ with LiFSI

(b) SiO$_2$ with LiPF$_6$

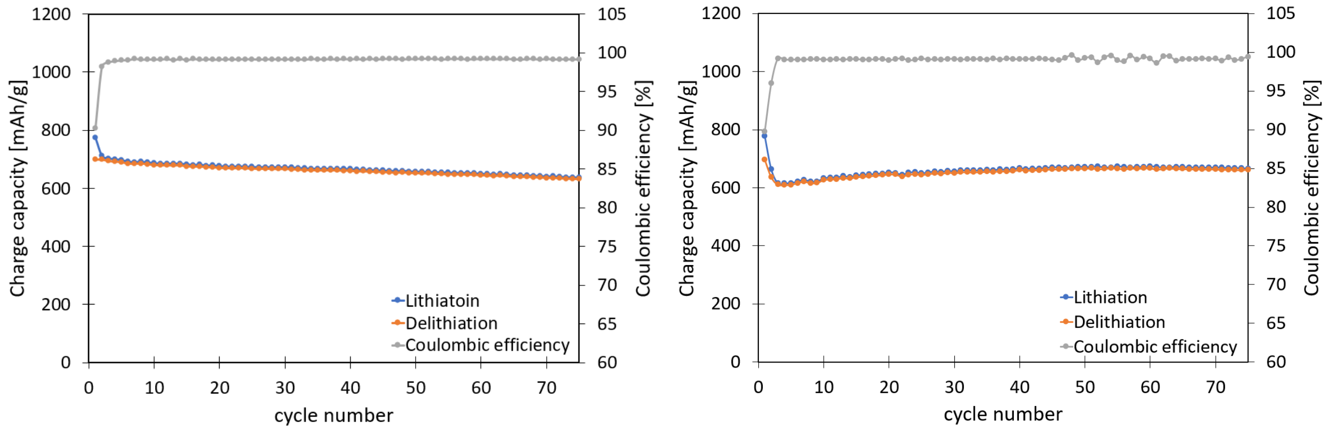

(c) SiO$_2$/C with LiFSI

(d) SiO$_2$/C with LiPF$_6$

Fig. 4.5. Specific capacity of SiO$_2$/C during galvanostatic cycling.

Voltage profiles

The voltage profiles during galvanostatic cycling of representative cells are presented in Figure 4.6.
Figure 4.6a presents the SiO_2 cell with LiFSI. Here, the capacity increases during cycling, from 450 $mAhg^{-1}$ in the 10th cycle to 540 $mAhg^{-1}$ in the 75th cycle, giving an increase of 90 $mAhg^{-1}$ during cycling. The SiO_2 cell with $LiPF_6$ is presented in Figure 4.6b exhibiting an increased capacity from 367 $mAhg^{-1}$ in the 10th cycle to 490 $mAhg^{-1}$ in the 75th cycle, giving a capacity increase of 123 $mAhg^{-1}$. Both SiO_2 cells, regardless of electrolyte, depicts consistent curvature of the slopes throughout cycling. However, the potential of where the plateaus are initiated is seen to decrease during cycling.

Figure 4.6c presents the voltage profile of the carbon-coated SiO_2 cell with LiFSI. The initial capacity in the 10th cycle after activation was 679 $mAhg^{-1}$ while the capacity of the 75th cycle was 624 $mAhg^{-1}$, giving a decrease in the capacity of 55 $mAhg^{-1}$. For this cell, a loss in the capacity during cycling is seen. However, it is only between 1.0 V and 1.3 V the delithiation curves differ from one another. The carbon-coated SiO_2 cell with $LiPF_6$, presented in Figure 4.6d, displays an increase in capacity. The 10th cycle yields a capacity of 615 $mAhg^{-1}$ while the capacity obtained in the 75th cycle was 660 $mAhg^{-1}$, giving an increase of 45 $mAhg^{-1}$. The potential at where the different plateaus are initiated increases from the 1st cycle to the 10th cycle, but decreases from the 10th cycle and throughout the cycling.

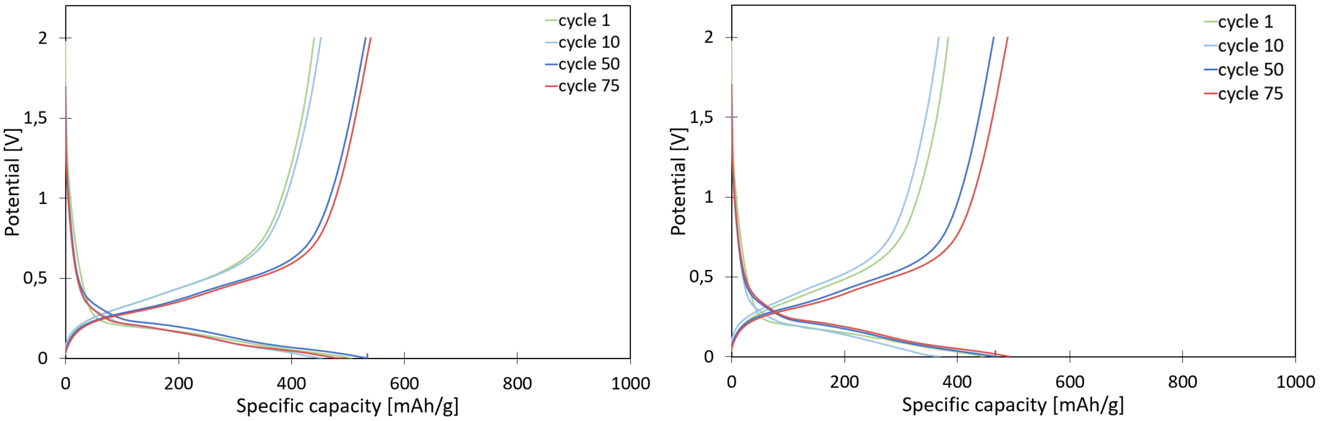

(a) SiO_2 with LiFSI **(b)** SiO_2 with $LiPF_6$

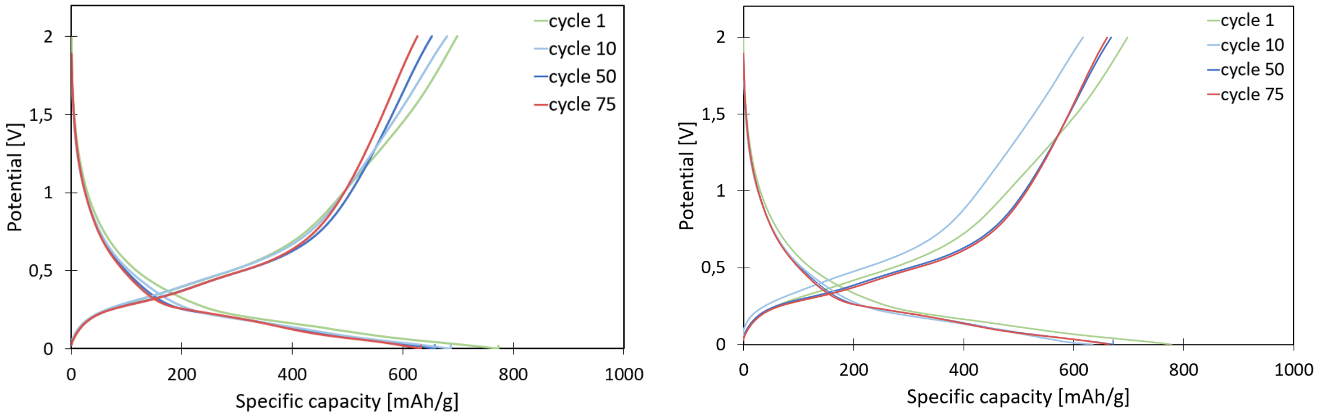

(c) SiO_2/C with LiFSI **(d)** SiO_2/C with $LiPF_6$

Fig. 4.6. Voltage profile of SiO_2/C during galvanostatic cycling.

Differential capacity

Differential capacity plots from the galvanostatic cycling of the selected cells are presented in Figure 4.7. All systems exhibit the same trend, i.e. that there are two main oxidation peaks (delithiation) and two main reduction peaks (lithiation) found in each system. Moreover, the onset potential of the peak formation changes during cycling for all systems. The onset potential of the reduction peaks decreases i.e. shifts towards a lower onset potential, while the onset potential of the oxidation peaks is shifted towards a higher potential. In addition, the difference in the differential capacity between oxidation and reduction is smaller for SiO_2 anodes than for carbon-coated SiO_2 anodes.

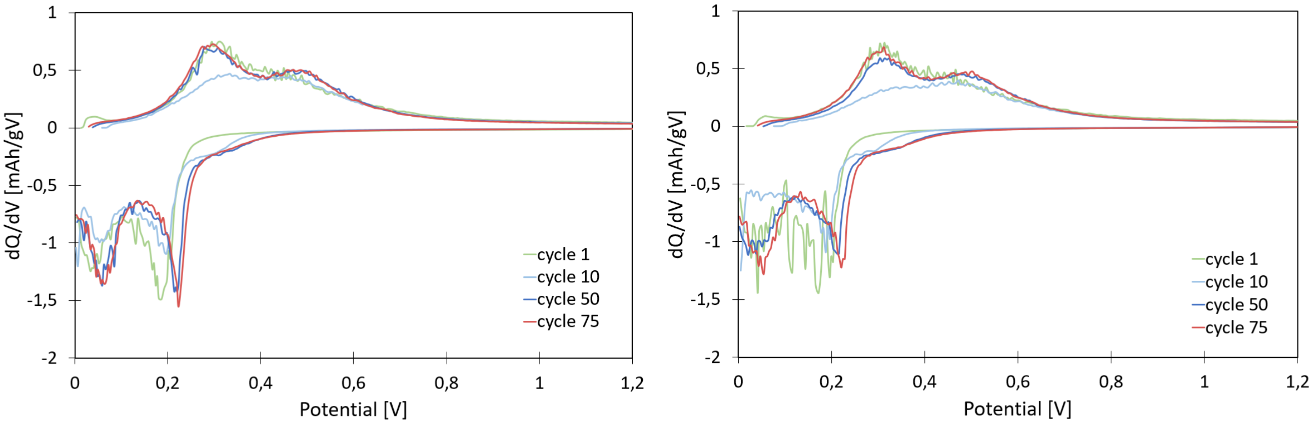

(a) SiO_2 with LiFSI **(b)** SiO_2 with $LiPF_6$

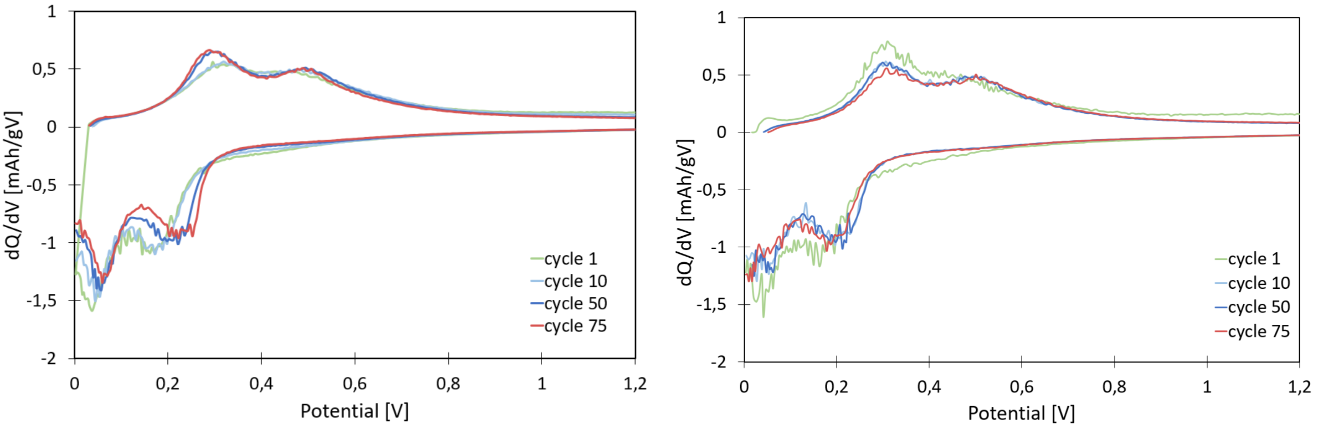

(c) SiO_2/C with LiFSI **(d)** SiO_2/C with $LiPF_6$

Fig. 4.7. Differential capacity of SiO_2/C during galvanostatic cycling.

Comparison of cells

The average capacity values for all cells, with an error bar indicating 1 standard deviation, are presented in Figure 4.8. Here, the difference in capacity between SiO_2 cells and carbon-coated SiO_2 cells is demonstrated. For the SiO_2 cells, LiFSI outperforms $LiPF_6$, while for carbon-coated SiO_2 $LiPF_6$ outperforms LiFSI. For the carbon-coated SiO_2 cells one can see that in the first cycles after the activation the capacity is very similar between the two different electrolytes, but the gap gets larger during cycling. The opposite is happening for the SiO_2 cells, where the difference between the two different electrolytes is larger in the beginning, but gets narrower with increasing cycle number.

For all cells, there is a drop in the capacity during the first cycles after the activation, i.e. cycle 6 in Figure 4.8. The final average capacity obtained is 669 ± 5.58 $mAhg^{-1}$, 598 ± 28.07 $mAhg^{-1}$, 516 ± 25.25 $mAhg^{-1}$ and 554 ± 6.66 $mAhg^{-1}$ for carbon-coated SiO_2 with $LiPF_6$, carbon-coated SiO_2 with LiFSI, SiO_2 with $LiPF_6$ and SiO_2 with LiFSI, respectively. Both carbon-coated SiO_2 with LiFSI and SiO_2 with $LiPF_6$ have large standard deviations, indicating large variations in the datasets.

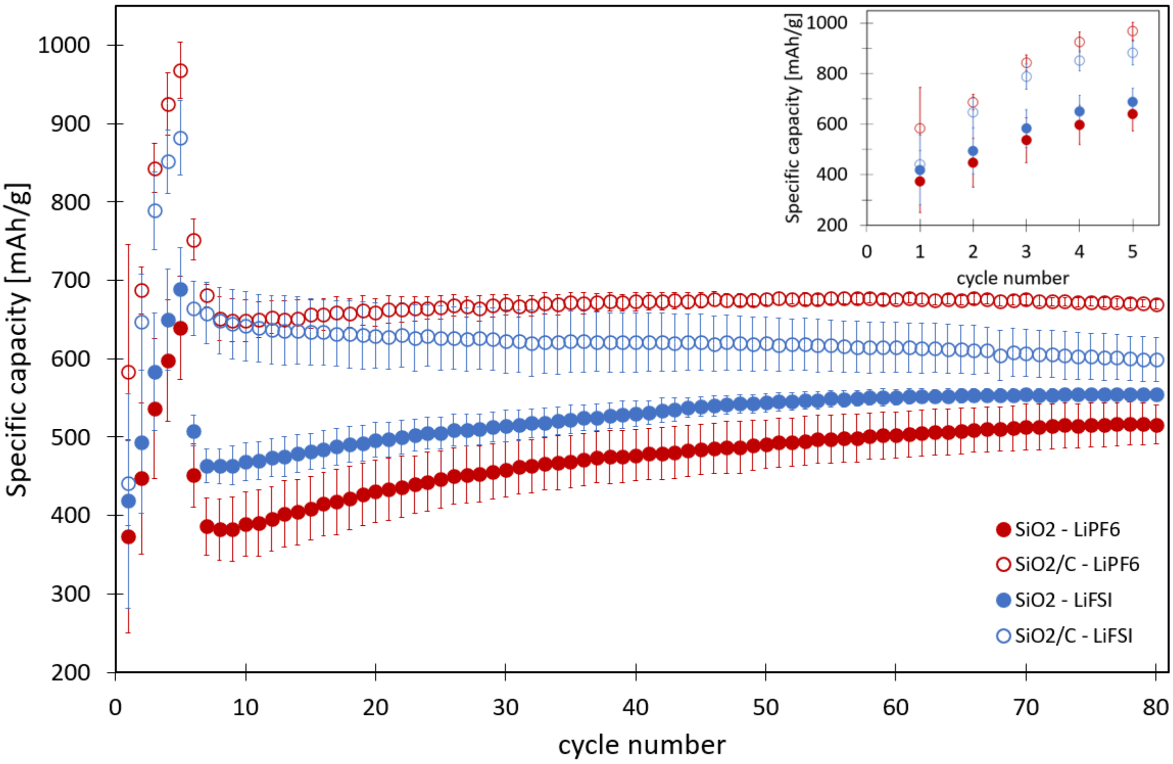

Fig. 4.8. The average specific charge capacity of all cells. Errorbar indicates one standard deviation. All cells cycled between 0.002 V - 2.00 V vs Li/Li^+. First five cycles at 50 mAg^{-1} and subsequent cycles at 100 mAg^{-1}.

The average coulombic efficiency of all cells is given in Figure 4.9. From this figure, one can see that the development of the coulombic efficiency in the first five cycles, which corresponds to the potentiostatic activation, differs for the different cells. However, the SiO_2 cells and the carbon-coated SiO_2 cells behave similarly. After the potentiostatic activation, i.e. cycle number six, the coulombic efficiency of carbon-coated SiO_2 cells and SiO_2 cells is ~90%. As of cycle seven, the coulombic efficiency is ~99% for all cells. A close up of how the coulombic efficiency evolves during cycling is given in Figure 4.10. From this figure a difference in coulombic efficiency between the different cells is visible, showing that the cells with SiO_2 obtained a higher coulombic efficiency than the carbon-coated SiO_2 cells after the activation cycles. Table 4.1 presents the coulombic efficiencies of the different cells.

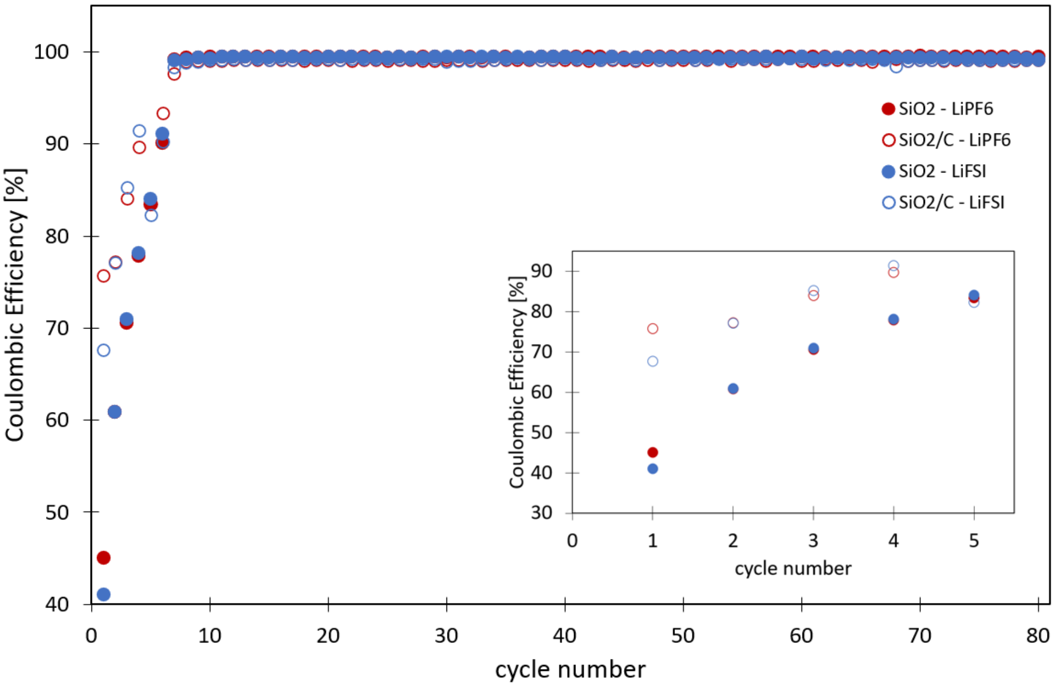

Fig. 4.9. Average coulombic efficiency for SiO_2 and SiO_2/C cells with $LiPF_6$ or LiFSI as electrolyte.

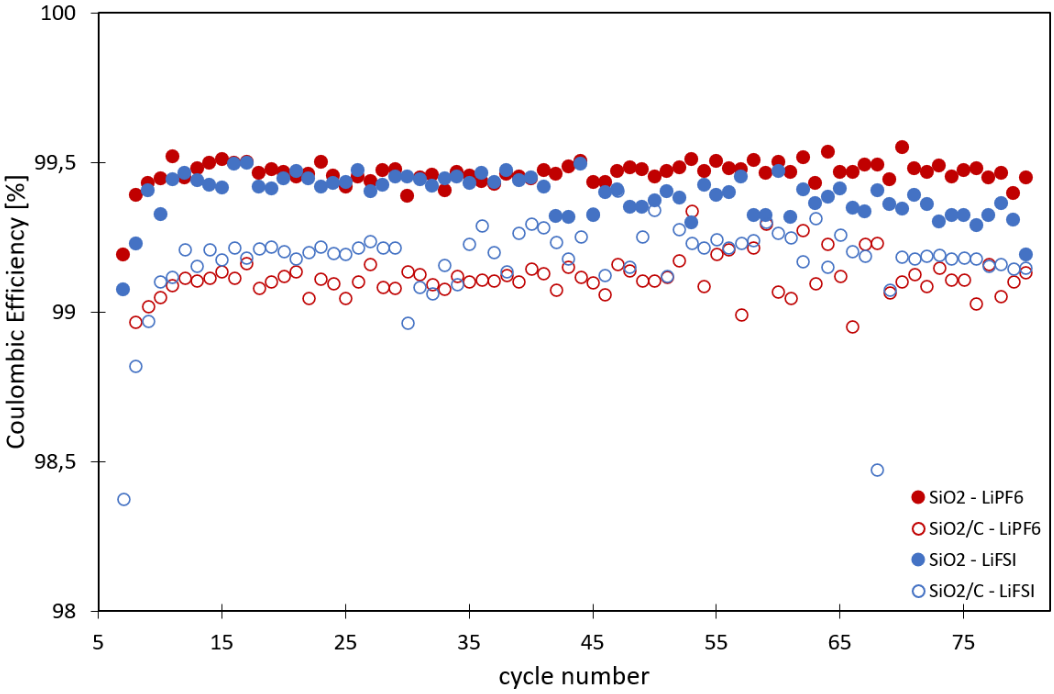

Fig. 4.10. The general trend for the coulombic efficiency of SiO_2 and SiO_2/C cells with $LiPF_6$ or LiFSI as electrolyte.

Tab. 4.1. Average coulombic efficiency of all cells, ± 1 standard deviation.

Cycle	SiO_2-$LiPF_6$	SiO_2-LiFSI	SiO_2/C-$LiPF_6$	SiO_2/C-LiFSI
Activation	CE [%]	CE [%]	CE [%]	CE [%]
1	45.15 ± 4.34	41.05 ± 1.06	75.75 ± 31.29	67.65 ± 24.70
3	70.58 ± 0.76	70.94 ± 0.50	84.07 ± 1.16	85.30 ± 1.17
5	83.43 ± 0.90	84.08 ± 0.99	92.48 ± 1.31	82.30 ± 22.08
Cycle				
1	90.12 ± 5.21	91.12 ± 5.82	93.32 ± 4.73	90.27 ± 0.11
10	99.51 ± 0.04	99.42 ± 0.05	99.10 ± 0.05	99.18 ± 0.09
50	99.51 ± 0.03	99.39 ± 0.07	99.19 ± 0.04	99.24 ± 0.07
75	99.45 ± 0.04	99.19 ± 0.12	99.13 ± 0.21	99.14 ± 0.05

4.3 XPS

The elemental composition of the different samples obtained from XPS (survey scans) are presented in Table 4.2. From this table, the amount of O 1s is found to be approximately similar for the two cells, with different electrolytes, stopped at the same potential. The amount of C 1s was found to be higher for LiFSI than $LiPF_6$, applying for both the cells stopped at 0.5 V and 0.2 V. Regarding F 1s, there is a lot more fluorine detected for $LiPF_6$ cells than LiFSI cells. The amount of Si 2s detected at 0.5 V was remarkably higher for $LiPF_6$ than for LiFSI, whereas at 0.2 V the difference was relatively small. The small amount of Cu and Na detected comes from the copper-foil and the Na-alginate respectively, and will not be assessed further.

Tab. 4.2. Elemental composition from survey scans

	0.5 V				0.2 V			
	LiFSI		$LiPF_6$		LiFSI		$LiPF_6$	
	At%	%STD	At%	%STD	At%	%STD	At%	%STD
O 1s	40.26	0.10	37.42	0.08	40.35	0.09	34.88	0.07
C 1s	32.51	0.13	23.03	0.11	23.91	0.11	20.06	0.11
F 1s	9.38	0.05	21.41	0.06	15.63	0.05	23.56	0.06
Si 2s	10.76	0.11	15.29	0.09	14.20	0.09	15.22	0.09
Na 1s	0.67	0.02	0.91	0.02	1.32	0.02	0.79	0.02
Cu 2p	0.03	0.01	0.04	0.01	0.03	0.01	0.01	0.01
S 2p	3.82	0.07			2.96	0.09		
N 1s	2.56	0.06			1.61	0.06		
P 2p			1.90	0.05			5.48	0.09

The Si 2p spectra are presented in Figure 4.11 and the corresponding atomic concentrations are presented in Table 4.3. Figure 4.11a is the Si 2p spectra of pristine SiO_2 powder. For the cells stopped at 0.5 V the atomic concentration of Li_4SiO_4 detected are larger for $LiPF_6$ than LiFSI, while the atomic concentration of SiO_2 is larger for LiFSI than $LiPF_6$. This is also observed for the cells stopped at 0.2 V.

When comparing the evolution of the cells from 0.5 v to 0.2 V the amount of Li_4SiO_4 have increased for both LiFSI and $LiPF_6$. The amount of SiO_2 have decreased for both LiFSI and $LiPF_6$, however more so for LiFSI than $LiPF_6$.

Tab. 4.3. Percentage atomic concentrations of the components for the Si 2p spectra

	LiFSI 0.5 V	$LiPF_6$ 0.5 V	LiFSI 0.2 V	$LiPF_6$ 0.2 V
Li_4SiO_4	81.5%	90.9%	86.9%	92.4%
SiO_2	18.5%	9.1%	13.1%	7.6%

Tab. 4.4. Characteristic binding energies (eV) for Si 2p (hν = 1486.6 eV)

Chemical state	Binding Energy [eV]	Reference
SiO_2	103.5	[51]
Li_4SiO_4	101.6 - 103.8	[52]

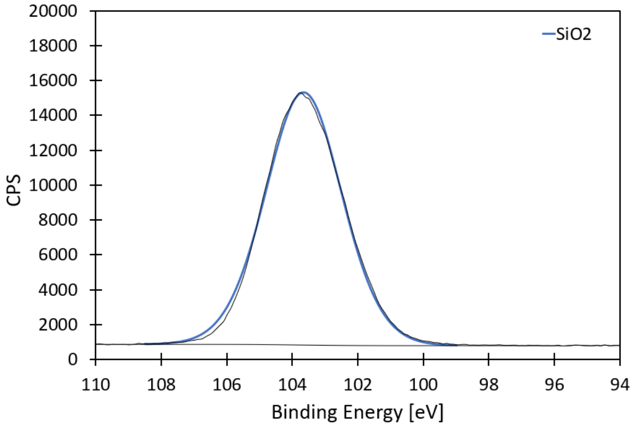

(a) Pristine SiO_2 powder

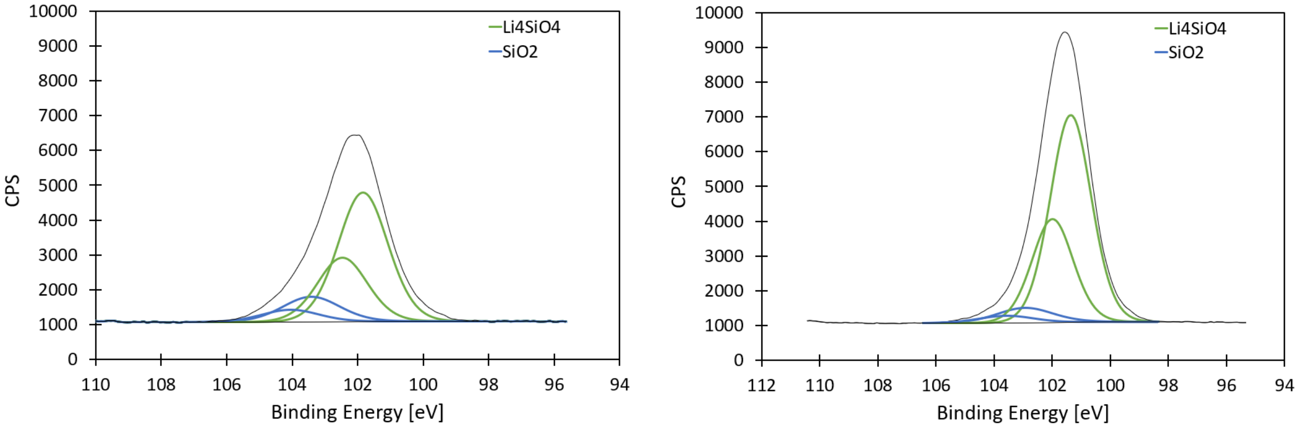

(b) SiO_2 with LiFSI stopped at 0.5 V

(c) SiO_2 with $LiPF_6$ stopped at 0.5 V

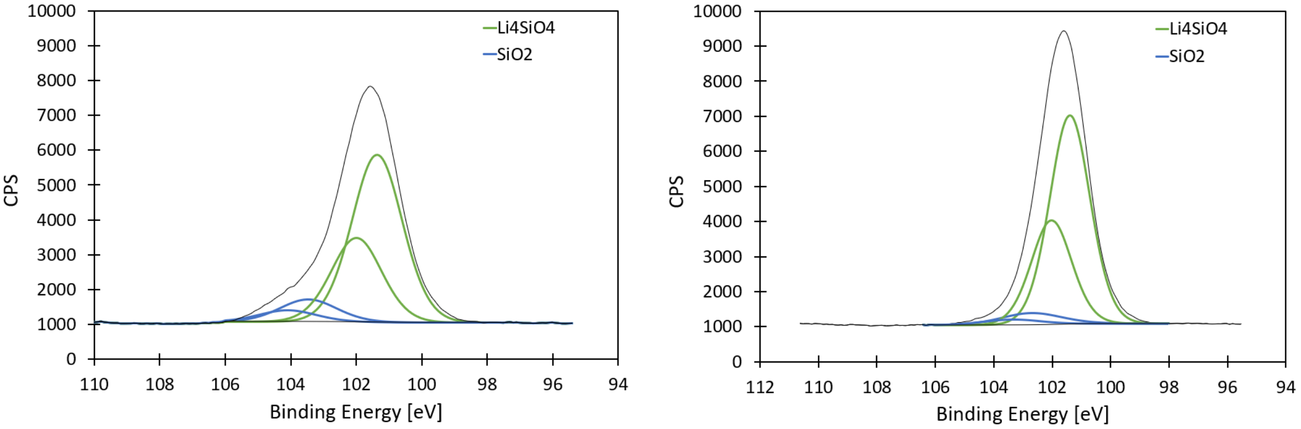

(d) SiO_2 with LiFSI stopped at 0.2 V

(e) SiO_2 with $LiPF_6$ stopped at 0.2 V

Fig. 4.11. High resolution spectra of Si 2p

The spectra for C 1s are presented in Figure 4.12 and corresponding atomic concentrations of the components are presented in Table 4.5. Figure 4.12a represents pristine SiO_2 powder and the peak attributed to C-H are most likely from surface contamination.
When comparing the cells with different electrolytes stopped at 0.5 V, i.e. Figures 4.12b and 4.12c, the atomic concentration of C-C detected is larger for $LiPF_6$ than LiFSI. The same goes for C-O. The atomic concentration of carbon black and O-C=O is larger in LiFSI than $LiPF_6$. Also, a peak attributed to CO_3 is found in the C 1s spectra of LiFSI, but not in the C 1s spectra of $LiPF_6$.
The C 1s spectra of the cells stopped at 0.2 V are presented in Figures 4.12d and 4.12e. Here, the atomic concentration of C-C is larger for $LiPF_6$ than LiFSI, while the atomic concentration of carbon black, C-O, and O-C=O is larger for LiFSI than $LiPF_6$.

From 0.5 V to 0.2 V the amount of carbon black has decreased for both LiFSI and $LiPF_6$, though the decrease in the carbon black is significantly larger for LiFSI than $LiPF_6$. For LiFSI an increase is observed in the amount of C-O, O-C=O and CO_2 from 0.5 V to 0.2 V, while the amount of C-C have decreased. For $LiPF_6$ an increase is seen for C-C, while a decrease is seen in for both C-O and and O-C=O.

Tab. 4.5. Percentage atomic concentration of the components for the C 1s spectra

	LiFSI 0.5 V	$LiPF_6$ 0.5 V	LiFSI 0.2 V	$LiPF_6$ 0.2 V
C-C	45.2%	47.3%	32.8%	50.2%
C-O	11.5%	20.2%	24.9%	18.7%
Carbon black	32.1%	26.2%	25.8%	24.9%
O-C=O	8.1%	6.4%	9.2%	6.2%
CO_3	3.2%		7.3%	

Tab. 4.6. Characteristic binding energies (eV) for C 1s (hν = 1486.6 eV)

Chemical state	Binding Energy [eV]	Reference
C-C	284.8, 285	[51 ,52]
C-O	~ 286	[51]
Carbon Black	~284	[11]
O-C=O	~288.5, 289.0-289.5	[51 ,52]
CO_3	289.3	[52]

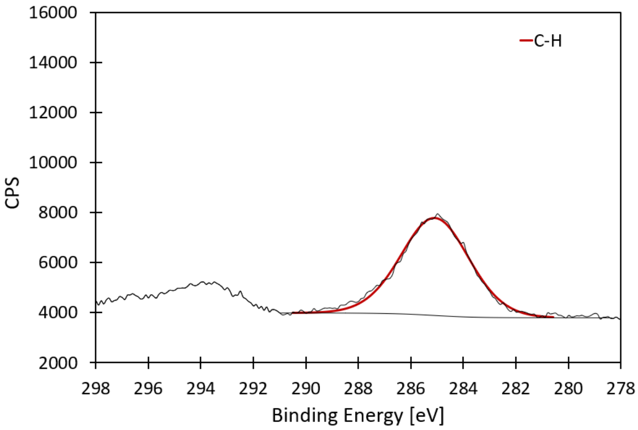

(a) Pristine SiO_2 powder

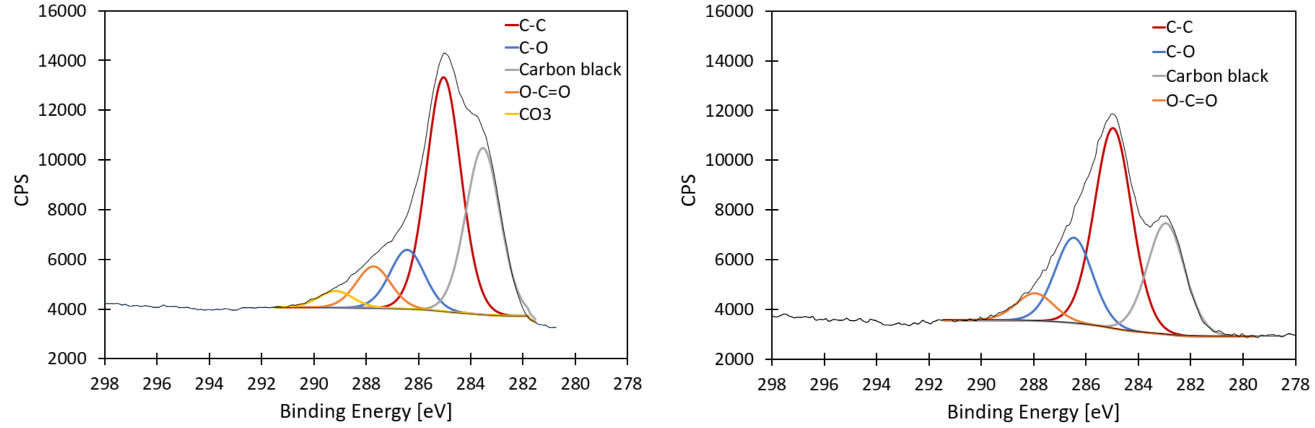

(b) SiO_2 with LiFSI stopped at 0.5 V

(c) SiO_2 with $LiPF_6$ stopped at 0.5 V

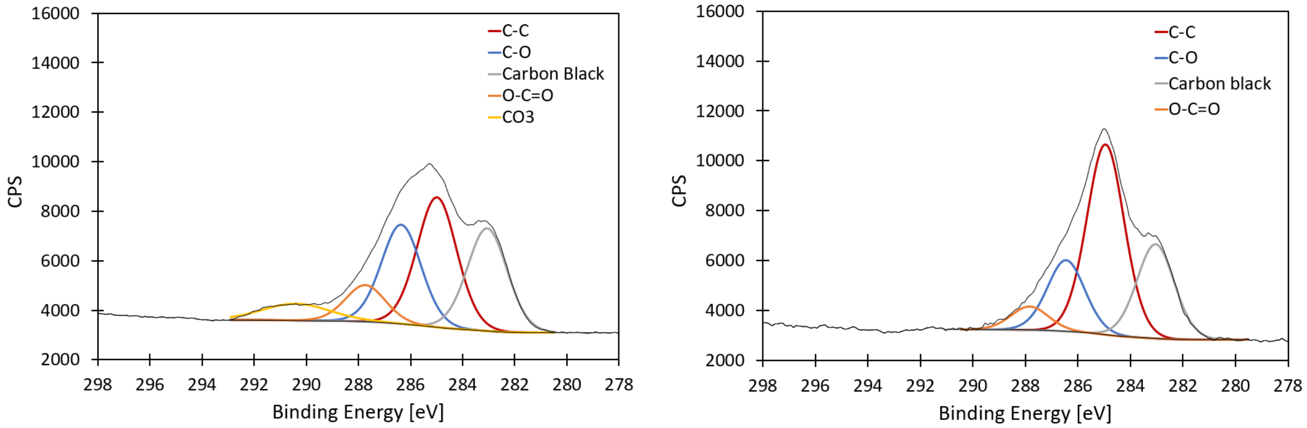

(d) SiO_2 with LiFSI stopped at 0.2 V

(e) SiO_2 with $LiPF_6$ stopped at 0.2 V

Fig. 4.12. High resolution spectra of C 1s

The O 1s spectra are presented in Figure 4.13 and Table 4.7 presents the corresponding atomic concentrations of the components. Figure 4.13a is the O 1s spectra of pristine SiO_2 powder. Figure 4.13b and Figure 4.13c presents the O 1s spectra of SiO_2 cells, with LiFSI and $LiPF_6$ respectively, stopped at 0.5 V. Here, the atomic concentration of SiO_2/binder is larger for $LiPF_6$ than for LiFSI while the atomic concentration of Li_4SiO_4 and C-O/CO_3 are larger for LiFSI than $LiPF_6$. Small concentrations of Li_2O are also detected, more so for LiFSI than $LiPF_6$.
For the cells stopped at 0.2 V the atomic concentration of SiO_2/binder and Li_4SiO_4 are larger for $LiPF_6$ than LiFSI. The O 1s atomic concentration of C-O/CO_3 is at 0.2 V significantly larger for LiFSI than $LiPF_6$. Moreover, the peak attributed to Li_2O is only detected for $LiPF_6$ for the cells stopped at 0.2 V.

From 0.5 V to 0.2 V the amount of SiO_2/binder and Li_4SiO_4 have decreased for LiFSI, but increased for $LiPF_6$. For LiFSI a large increase in the amount of C-O/CO_3 is observed, while a relatively small decrease is observed for $LiPF_6$. The amount of Li_2O has increased for $LiPF_6$.

Tab. 4.7. Percentage atomic concentration of the components for the O 1s spectra

	LiFSI 0.5 V	$LiPF_6$ 0.5 V	LiFSI 0.2 V	$LiPF_6$ 0.2 V
SiO_2/binder	75.7%	82.5%	61.0%	84.0%
Li_4SiO_4	12.8%	9.8%	8.1%	10.2%
C-O/CO_3	10.7%	7.5%	30.9%	5.0%
Li_2O	0.8%	0.3%		0.9%

Tab. 4.8. Characteristic binding energies (eV) for O 1s (hν = 1486.6 eV)

Chemical state	Binding Energy [eV]	Reference
Li_4SiO_4	~529	[51]
SiO_2	532.9	[51]
Li_2O	528.4	[11]
C-O/CO_3	~533	[51]

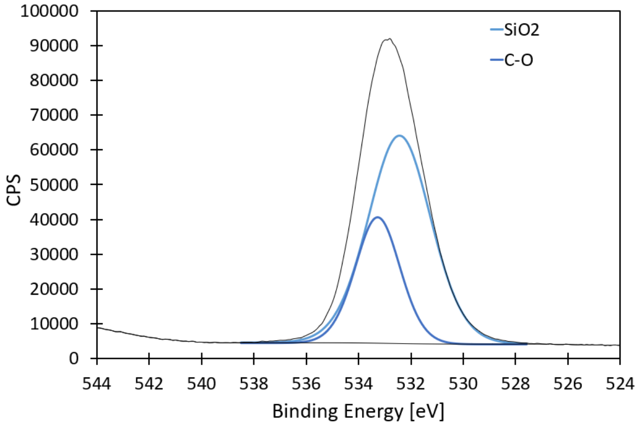

(a) Pristine SiO_2 powder

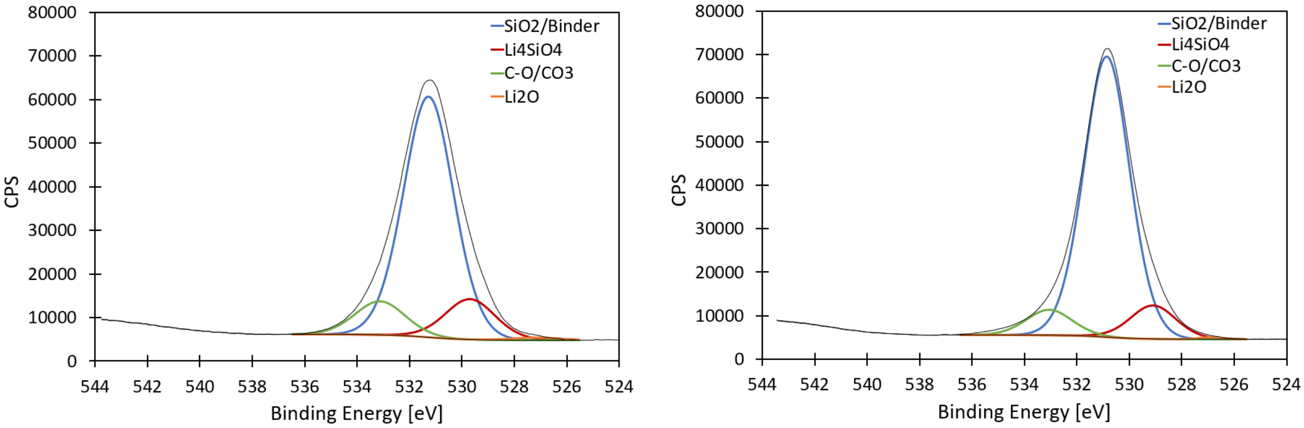

(b) SiO_2 with LiFSI stopped at 0.5 V

(c) SiO_2 with $LiPF_6$ stopped at 0.5 V

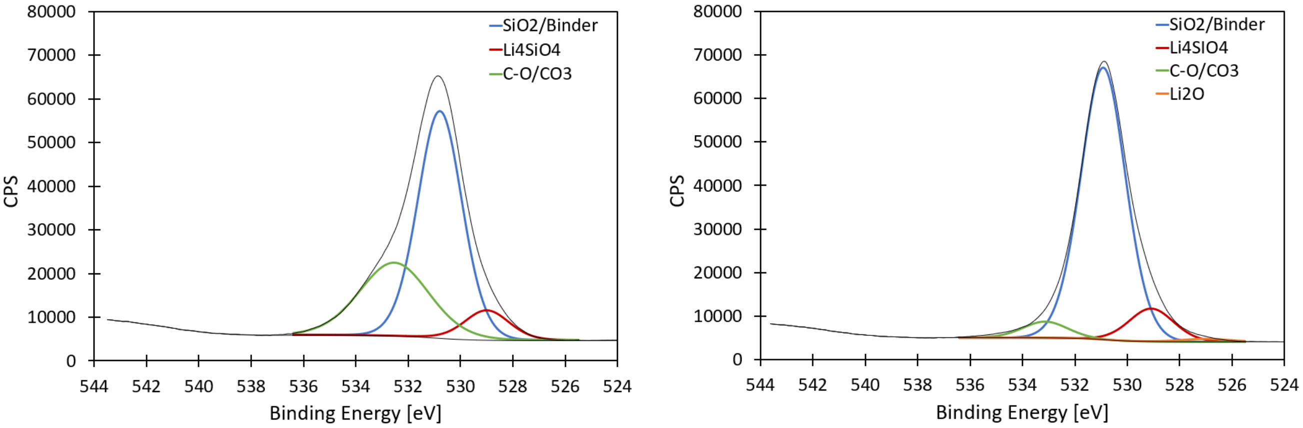

(d) SiO_2 with LiFSI stopped at 0.2 V

(e) SiO_2 with $LiPF_6$ stopped at 0.2 V

Fig. 4.13. High resolution spectra of O 1s

The F 1s spectra and corresponding overview of the atomic concentration of the components are given in Figure 4.14 and Table 4.9 respectively. For the cells stopped at 0.5 V the atomic concentration of the lithium salt, i.e LiFSI, and $LiPF_6$ for the cell with LiFSI and $LiPF_6$ respectively, are larger for $LiPF_6$ than for LiFSI. However the atomic concentration of LiF is larger for LiFSI than $LiPF_6$. For both the LiFSI cell and the $LiPF_6$ cell the atomic concentration of the salt degradation products is larger than the atomic concentration of LiF.
For the cells stopped at 0.2 V the same relation between the two cells applies, however, here the atomic concentration of LiF is larger than the atomic concentration of the lithium salt for the LiFSI cell.

From 0.5 V to 0.2 V the amount of lithium salt and LiF have decreased and increased respectively for LiFSI, whereas for $LiPF_6$ the amount of lithium salt and LiF have increased and decreased respectively.

Tab. 4.9. Percentage atomic concentration of the components for the F 1s spectra

	LiFSI 0.5 V	$LiPF_6$ 0.5 V	LiFSI 0.2 V	$LiPF_6$ 0.2 V
LiF	46.1%	38.8%	53.0%	37.0%
F-S/F-P	53.9%	61.2%	47.0%	63.0%

Tab. 4.10. Characteristic binding energies (eV) for F 1s (hν = 1486.6 eV)

Chemical state	Binding Energy [eV]	Reference
LiF	684-685	[53]
F-S (LiFSI)	687.9	[11]
F-P ($LiPF_6$)	~686, 687.8	[53 ,52]

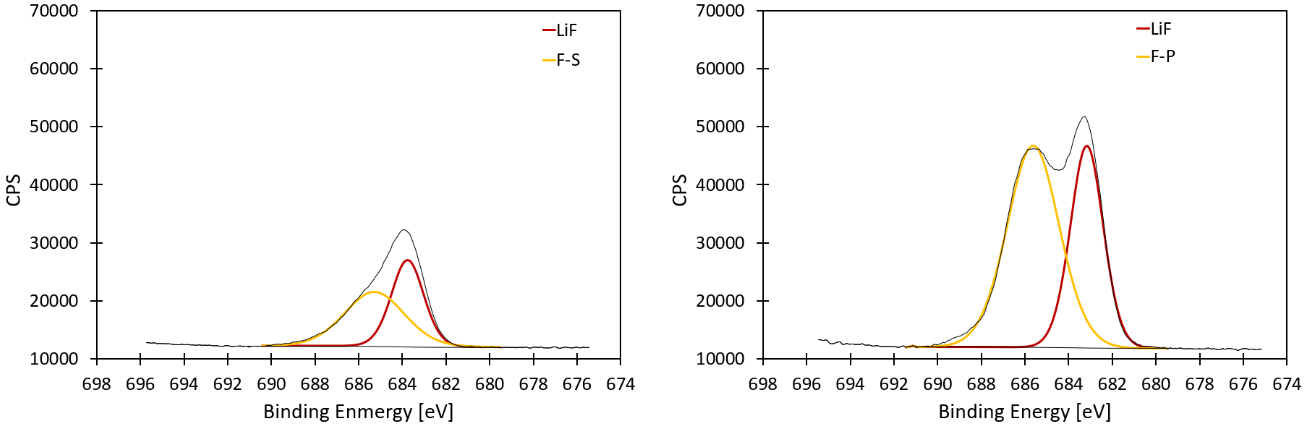

(a) SiO_2 with LiFSI stopped at 0.5 V

(b) SiO_2 with $LiPF_6$ stopped at 0.5 V

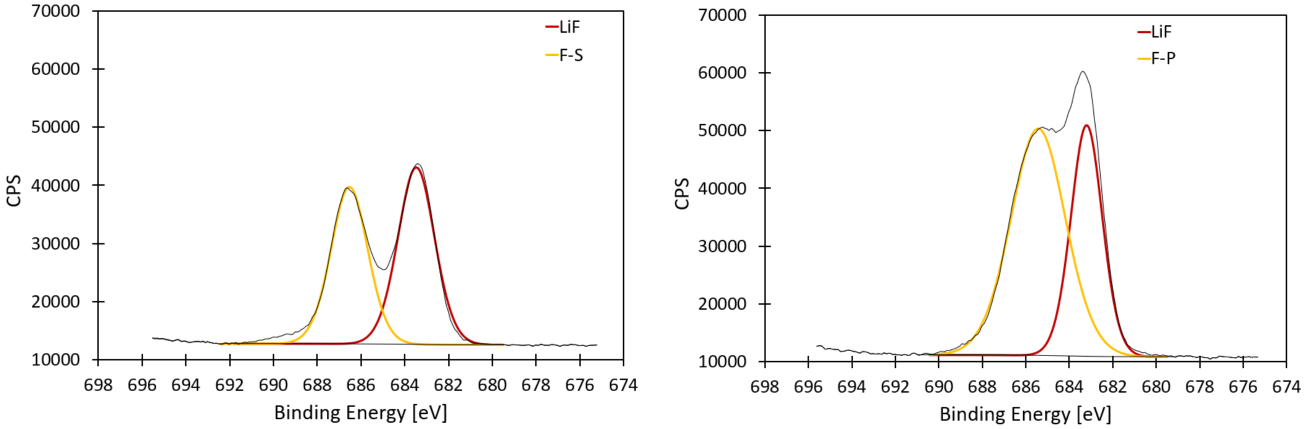

(c) SiO_2 with LiFSI stopped at 0.2 V

(d) SiO_2 with $LiPF_6$ stopped at 0.2 V

Fig. 4.14. High resolution spectra of F 1s

The P 2p spectra from the $LiPF_6$ cells are presented in Figure 4.15a and 4.15b. For the cell stopped at 0.5 V the atomic concentration of P-F detected, as seen from Table 4.11, is greater than the atomic concentration of P-O. However, for the cell stopped at 0.2 V the atomic concentration of P-O is greater than the atomic concentration of P-F.

The N 1s spectra from the LiFSI cells are presented in Figure 4.15c and 4.15d, and the atomic concentration of the components are presented in Table 4.11. Here, the atomic concentration of N-S (from the LiFSI salt) for the cell stopped at 0.5 V is very small, however, a larger concentration of N-S is seen for the cell stopped at 0.2 V. For the grey peak, attributed to decomposition products of the LiFSI salt, the atomic concentration is larger at 0.5 V than 0.2 V.

For the S 2p spectra, presented in Figure 4.15e and 4.15f, peaks attributed to the lithium salt, i.e LiFSI, the decomposition products of the salt and a peak labeled A is detected. The atomic concentration of LiFSI detected at 0.5 V is relatively large, whereas at 0.2 V the amount of LiFSI detected have drastically decreased. The atomic concentration of the decomposition products of the lithium salt have increased from 0.5 V to 0.2 V. The peaks labeled A is attributed to degradation of the SEI due to the X-rays, and will therefore not be considered.

Tab. 4.11. Percentage atomic concentration of the components for the P 2p, N 1s and S 2p spectra

	LiFSI 0.5 V	$LiPF_6$ 0.5 V	LiFSI 0.2 V	$LiPF_6$ 0.2 V
P 2p				
P-O		40.5%		66.7%
P-F		59.5%		33.3%
N 1s				
N-S (LiFSI)	6.1%		15.6%	
Decomposition product	93.9%		84.4%	
S 2p				
LiFSI	30.9%		7.1%	
Decomposition product	52.5%		66.8%	
A	16.6%		26.2%	

Tab. 4.12. Characteristic binding energies (eV) for P 2p, N 1s and S 2p (hν = 1486.6 eV)

Chemical state	Binding Energy [eV]	Reference
P 2p		
P-F	~136	[53]
P-O	~133	[52]
N 1s		
N-S (LiFSI)	~401	[53]
S 2p		
LiFSI	170.2	[54]

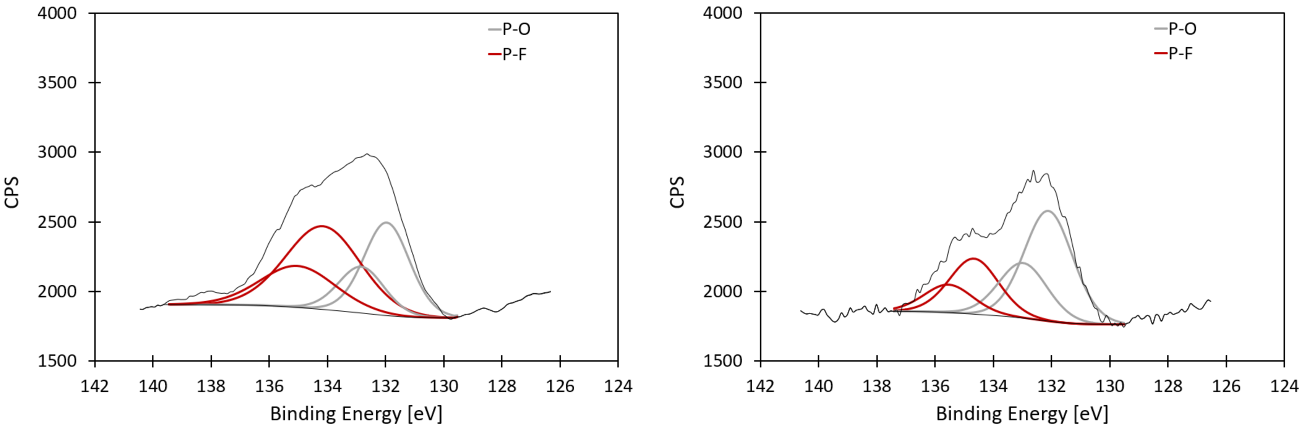

(a) P 2p spectra of SiO_2 with $LiPF_6$ stopped at 0.5 V **(b)** P 2p spectra of SiO_2 with $LiPF_6$ stopped at 0.2 V

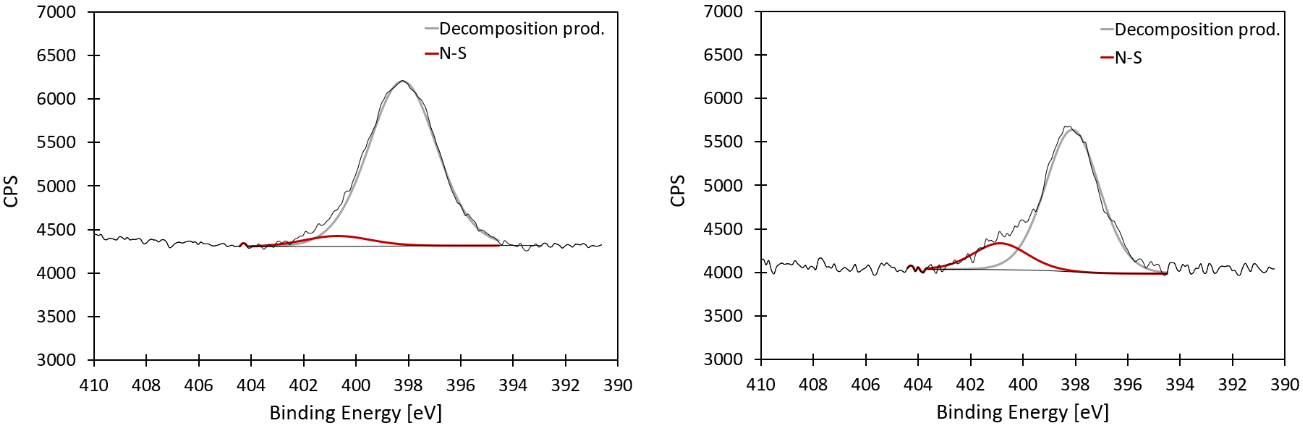

(c) N 1s spectra of SiO_2 with LiFSI stopped at 0.5 V **(d)** N 1s spectra of SiO_2 with LiFSI stopped at 0.2 V

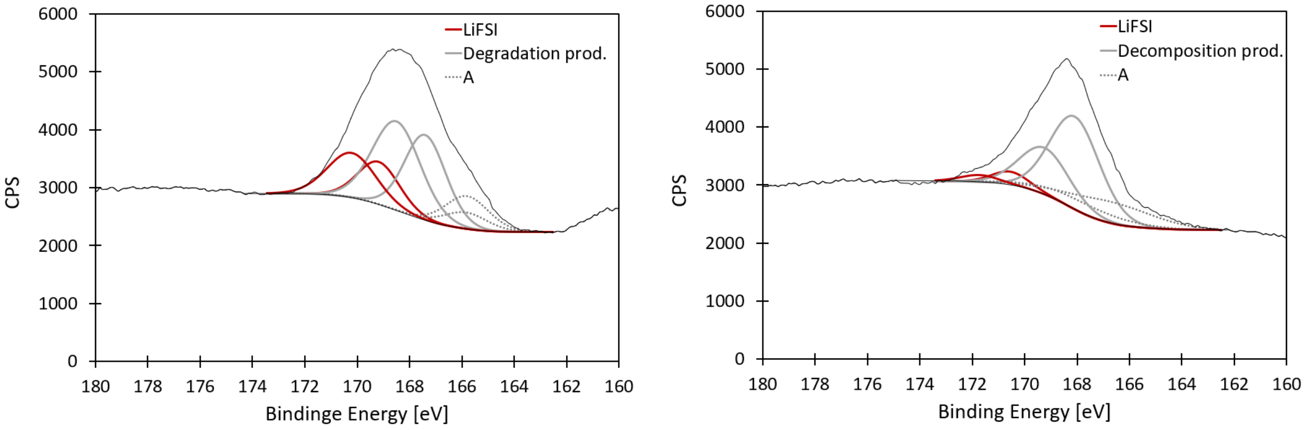

(e) S 2p spectra of SiO_2 with LiFSI stopped at 0.5 V **(f)** S 2p spectra of SiO_2 with LiFSI stopped at 0.2 V

Fig. 4.15. High resolution spectra of P 2p, N 1s and S 2p

4.4 FIB/SEM

Cross-sections made using the FIB were acquired for pristine electrodes with SiO_2 and carbon-coated SiO_2 as the active material. SEM images of these cross-sections are given in Figure 4.16. From these images, it looks like the electrode layer is thicker for the carbon-coated SiO_2 anodes than the SiO_2 anodes. The carbon-coated SiO_2 anodes also look more porous and the carbon layer surrounding the particles is visible.
Cross-sections of electrodes stopped at the second cycle of potentiostatic activation were also acquired. The SEM images of these electrodes are presented in Figure 4.17. Here, one can also see that the thickness of the carbon-coated SiO_2 electrode is greater than for the SiO_2 electrodes. For all three samples, one can notice a loss in the porosity of the electrode material upon cycling.

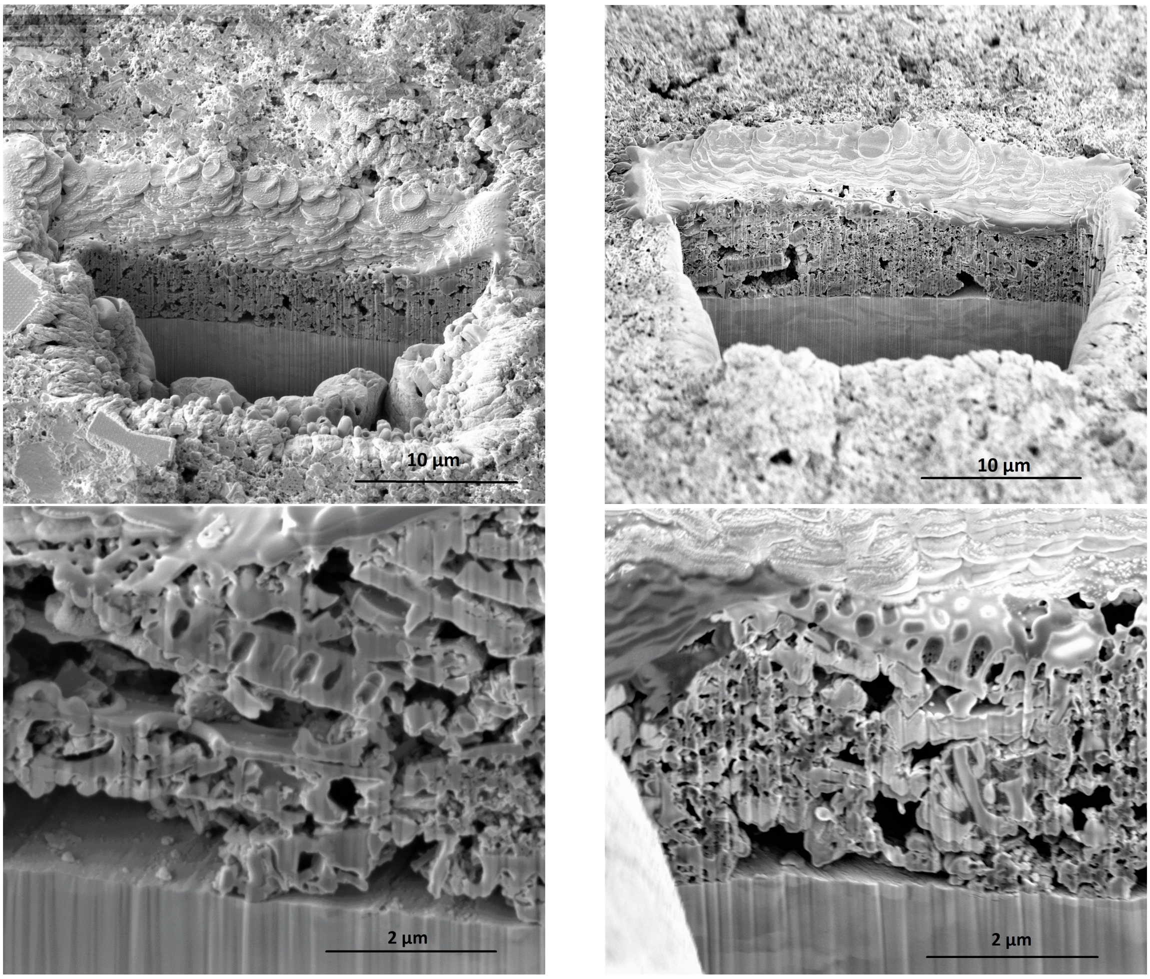

(a) SiO_2 **(b)** SiO_2/C

Fig. 4.16. Cross-section of pristine electrodes

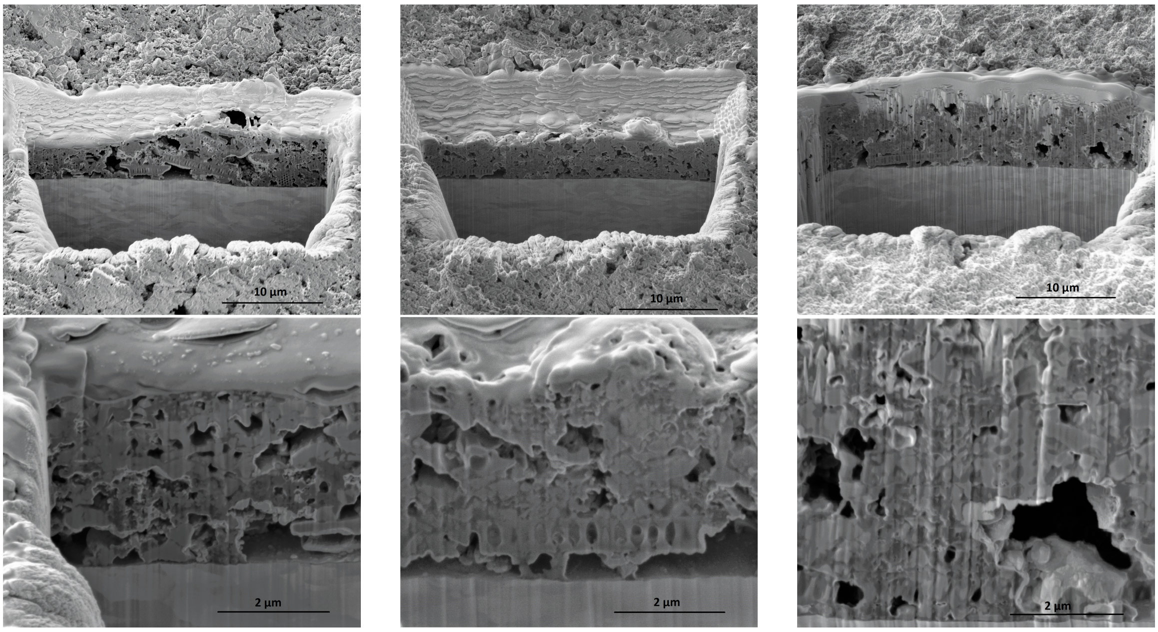

(a) SiO_2 with LiFSI **(b)** SiO_2 with $LiPF_6$ **(c)** SiO_2/C with $LiPF_6$

Fig. 4.17. Cross-section of electrodes stopped at the second activation cycle

In Figure 4.18 SEM images of SiO_2 frustules are presented. Here, the different porous layers of the SiO_2 frustule, as described in section 2.6, can be seen.

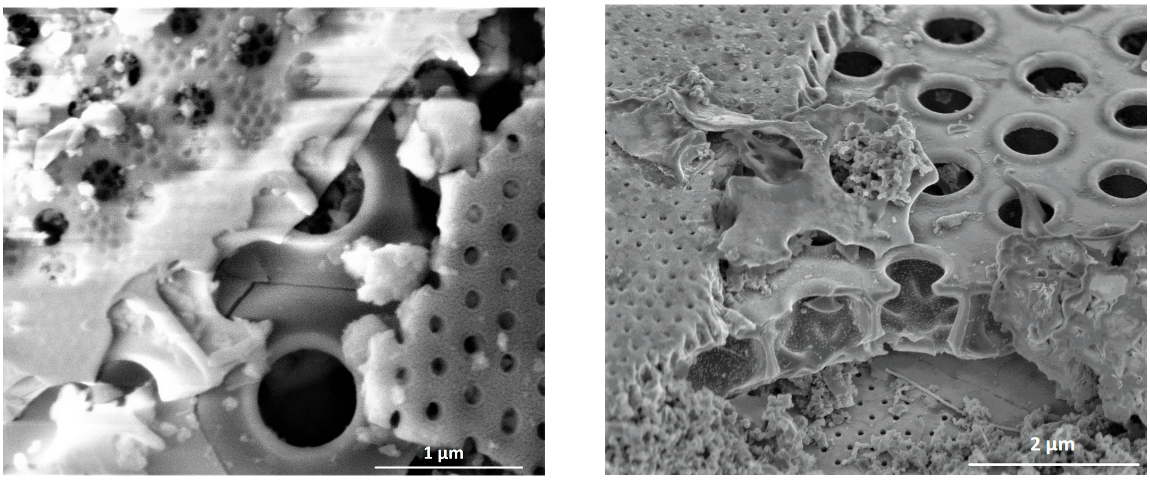

Fig. 4.18. SEM images showing the structure of the SiO_2 frustule

Figure 4.19 shows the surface of carbon-coated SiO_2 electrodes, for both a pristine electrode and an electrode stopped in the second galvanostatic activation step. From this figure, it is found that the surface structure is not showing as clearly for the cell stopped during the second activation step, as a result of the SEI formed on the surface of the electrode.

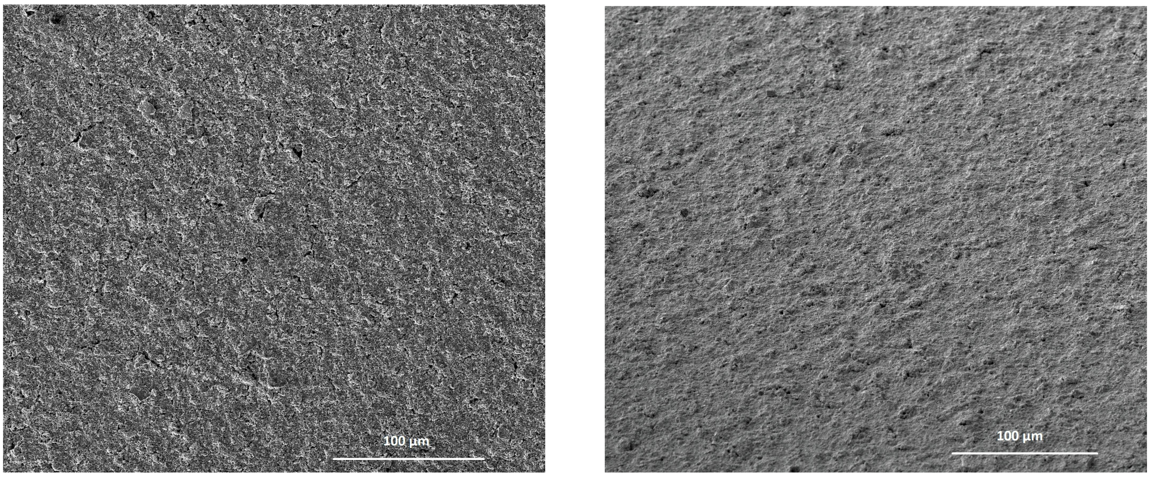

(a) Pristine electrode

(b) SiO_2/C-$LiPF_6$ electrode stopped in the 2nd activation step.

Fig. 4.19. SEM images of the electrode surface of carbon-coated SiO_2 electrodes.

Chapter 5: Discussion

5.1 Electrochemical characterization

The electrochemical data of the cells presented in Section 4.2 will be discussed further in this section. Firstly the differences in the electrochemical activation of the different systems will be discussed, followed by a discussion of the results from the cells cycled long-term. The electrochemical data is important as it determines the performance of the cells. However, the differences in performance seen by electrochemical characterization cannot always be explained by this data.

5.1.1 Analysis of electrode activation

The introduction of electrochemical reduction by potentiostatic holding have showed to significantly improve the capacity of both SiO_2 and carbon-coated SiO_2 anodes. Norberg reported a capacity increase of 632 $mAhg^{-1}$ when comparing a cell with unmilled pristine SiO_2, cycled without electrochemical reduction step, and a cell with milled pristine SiO_2 which had undergone a 48 h electrochemical reduction step at 0.002 V.[17] An improvement in the capacity for both SiO_2 and carbon-coated SiO_2 is also supported by the work of Norberg.[17] The electrochemical activation procedure conducted on cells in this work, presented in Figure 4.1, includes potentiostatic hold steps at both 2 V and 0.002 V for 24 h and 48 h respectively, which was repeated five times. The reason for introducing the hold steps at 0.002 V is the slow reaction rate of SiO_2 with Li^+. At 0.002 V there is a high driving force for the conversion reactions, given in equations 2.18-2.21, as it is below the lithiation potential of SiO_2, but above the potential of Li-plating. Thus, by holding the potential at 0.002 V for 48 h a larger amount of SiO_2 is able to react with Li^+, and the material becomes more active. This procedure was proposed by Lepoivre *et al.*,[37] and good results with this procedure is also seen in the work of Norberg.[2] The reason for including hold steps at 2.0 V is to ensures, more or less, complete delithiation. If the delithiation is not completed, some amount of Li^+ will be trapped in the material for each cycle, eventually preventing the lithiation.

The specific capacity plots in Figure 4.2 shows how the material is evolving during the galvanostatic activation. Here, an increase in the capacity is seen for each of the five activation cycles, however, the capacity increase is larger for the first cycles and decreases throughout the activation. The gain in capacity during the galvanostatic activation indicates that the material is getting more activated. When the material is fully activated, i.e. reached full potential, the lithiation and delithiation reactions are more reversible.

The coulombic efficiency during the activation, presented in Figure 4.2, is quite low, which indicates that the silica is using a lot of lithium that will be irreversibly lost. Hence, in order to use silica as an anode material in real applications prelithiation should be considered to avoid excess lithium consumption.

From the voltage profiles, Figure 4.3, a decrease in the energy gap, E_g, between lithiation and delithiation is observed, as the delithiation reaction curves and the lithiation reaction curves shifts downwards and upwards, respectively, indicating that the reactions are becoming less energetically expensive. As the energy gap, E_g decreases, the overpotential changes. This can also be seen in the differential capacity plots, Figure 4.4, as a shift in the peak centers. This shift upon cycling is most likely caused by a significant overpotential in the electrode, due to poor conductivity of the electrode matrix. This hypothesis is supported by the work of Lepoivre *et al.*, where peak formation was observed in the differential capacity plots at similar potentials after electrochemical reduction of SiO_2 nanoparticles.[37]
The first lithiation cycles, in Figure 4.3, differs from the other lithiation cycles, indicating electrolyte decomposition and SEI formation. This can also be seen in the first cycle of the differential capacity plots, presented in Figure 4.4, which shows that the silica does not react during the first activation cycle, i.e. there are no peaks at the potentials corresponding to the reaction of silicon, hence the small peaks in the first cycle, seen at high potentials (~ 1.0 V and ~ 0.8 V) are attributed to the formation of the SEI.

When comparing the voltage profiles of the four cells (Figure 4.3) it is observed that the curvature of the slopes given by the SiO_2 cells are much steeper than the curvature of the carbon-coated SiO_2 cells. The difference in the slopes is attributed to the carbon lithiation and delithiation, as the different chemical reactions takes place at different voltages for SiO_2 and carbon-coated SiO_2. In addition, a difference in the lithiation curve between “pure” SiO_2 cells and carbon-coated SiO_2 cells are seen from Figure 4.3. Below 0.5 V and between 0 - 200 $mAhg^{-1}$ a kink in the lithiation curve is observed as of the second activation cycle, however, only for the “pure” SiO_2 cells. A reason for this might be that the carbon-coating, which accounts for 30% of the electrode mass, lithiates/delithiates over a wide potential range, masking the behavior of the SiO_2.
Moreover, the specific capacity is higher for carbon-coated SiO_2 than “pure” SiO_2. The reason for this is twofold. Firstly, the initial higher specific capacity of carbon-coated SiO_2 cells is mainly attributed to the capacity contribution from Li^+ intercalation into the amorphous carbon-coating.[17] The capacity contribution from carbon varies depending on the composition, however, from the work of Norberg the carbon contribution was estimated to be 226 $mAhg^{-1}$ in a cell with 50 wt% sucrose coated SiO_2 and 35 wt% carbon black.[17] As the carbon-coating in this work only contains 40 wt% glucose and 10 wt% carbon black is used in

the electrode matrix, it is assumed that the contribution of carbon is not as high as Norberg estimated in his work. Secondly, the increased capacity of carbon-coated SiO_2 cells could also be caused by a higher initial conversion of SiO_2 to Si, as the carbon-coating facilitates the transport of electrons around the SiO_2 particles, creating more active sites for the reaction with Li^+.[17] Limitations in the capacity increase during the galvanostatic activation are mainly caused by two factors, i.e. an overpotential created by extensive SEI formation on carbon-coated SiO_2 cells, limiting the conversion reactions of SiO_2 to Si, or limiting reactivity of SiO_2 beyond a certain penetration depth. The latter is supported in the work by Lepoivre *et al.*[37] However, Norberg suggested in his studies that although the SEI formed on the carbon-coating SiO_2 anodes are thicker, it exhibits good Li^+ conductivity, limiting the overpotential caused by the SEI.

From the voltage profiles, Figure 4.3, and the differential capacity plots, Figure 4.4, it is found that cells with similar active material exhibits relatively identical plots, independent of the electrolyte. However, from Figure 4.3a and 4.3b it is apparent that the capacity gained for the SiO_2-LiFSI is higher than for SiO_2-$LiPF_6$. This difference in capacities between $LiPF_6$ and LiFSI might be attributed to the properties of the SEI, indicating that a thinner and/or more conductive SEI is formed with LiFSI than with $LiPF_6$. For the carbon-coated SiO_2 cells, given in Figure 4.3c and 4.3d, higher capacity was gained in the first three cycles for SiO_2/C-LiFSI compared to SiO_2/C-$LiPF_6$. However, the final capacity reached during the activation of the cells was higher for SiO_2/C-$LiPF_6$ than SiO_2/C-LiFSI. These differences are most likely attributed to the difference in the chemistry of the different reactions, as two different electrolytes are used there will be a difference in the amounts and kinds of decomposition products, i.e. difference in the SEI, which again can affect the capacity.

Electrochemical reduction of silica is primarily divided into three reactions, given in Section 2.5.2. Here, reaction 2.18 is considered reversible, while reaction 2.19 and 2.20 are irreversible. However, these three reactions all have Si as a product, which can react further with Li^+. In Figure 5.1, which is a modified plot of the differential capacity of SiO_2 cell with LiFSI, the lithiation and delithiation reactions between Li^+ and a-Si (amorphous silicon) are indicated. Both the lithiation and delithiation reactions happens in two steps, as indicated by the figure.

The differential capacity plots for the galvanostatic activation, presented in Figure 4.4, showed an increasing trend for all peaks during cycling. The reason for this is as the activation proceeds, the material gets more electrochemically activated, allowing more of the material to react. When comparing the differential capacity of SiO_2 and carbon-coated SiO_2 in Figure 4.4, the lithiation starts at a higher dQ/dV for SiO_2 than for carbon-coated SiO_2, i.e. -0.2 and -0.5 $mAhg^{-1}V^{-1}$ respectively. In addition, the two lithiation peaks, at ~ 0.2 V and ~ 0.05 V, are more prominent for SiO_2 than carbon-coated SiO_2. The dQ/dV gap between lithiation and delithiation is larger for carbon-coated SiO_2 than SiO_2, indicating that the resistance towards lithiation and delithiation is higher for cells with carbon coating, either because of the transport of Li^+ through the coating or because of the SEI layer.

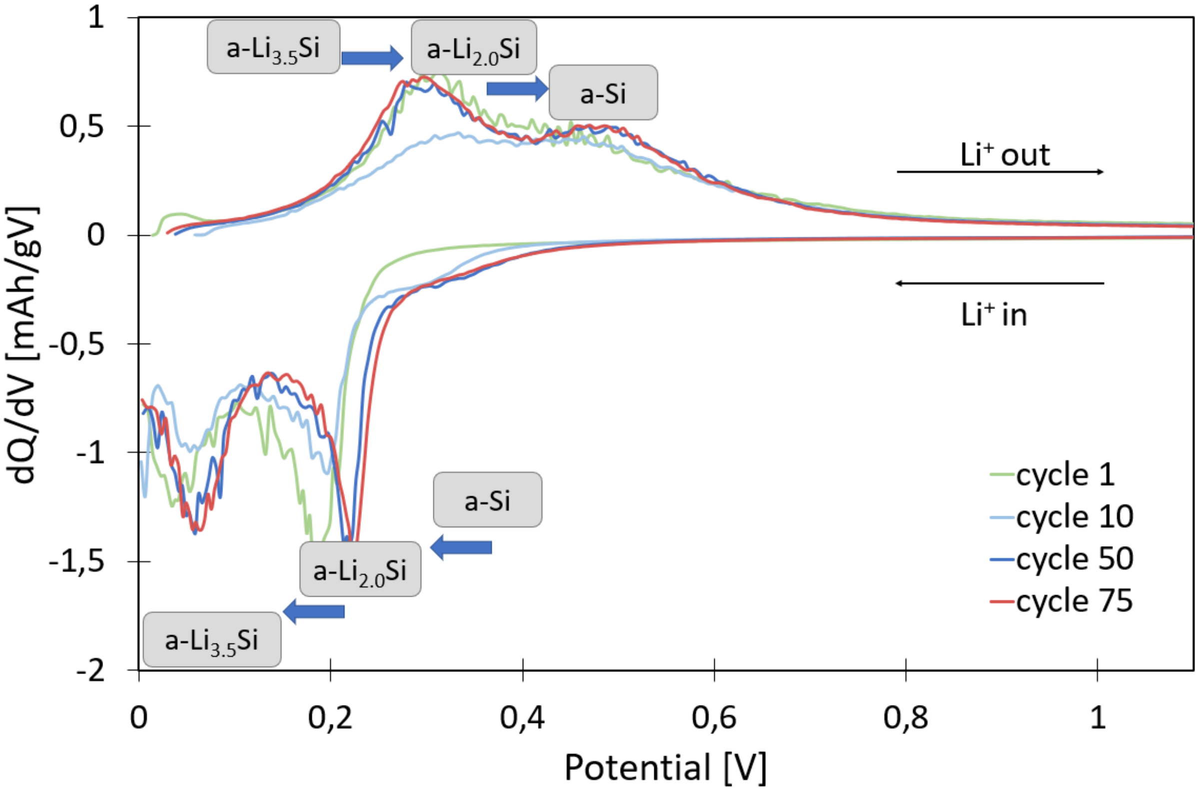

Fig. 5.1. Differential capacity plot of SiO_2 cell with LiFSI showing the different reactions occurring at different potentials

5.1.2 Analysis of long-term cycled electrodes

The specific capacity of the cells during long-term cycling is presented in Figure 4.5. For both SiO_2 cells, presented in Figure 4.5a and Figure 4.5b for LiFSI and $LiPF_6$ respectively, the capacity continues to increase throughout the cycling. The capacity in the 5th cycle was 347 $mAhg^{-1}$ and 437 $mAhg^{-1}$, whereas the final capacity was 490 $mAhg^{-1}$ and 540 $mAhg^{-1}$ for $LiPF_6$ and LiFSI respectively. Moreover, for the carbon-coated SiO_2 cell with LiFSI, Figure 4.5c, a decreasing capacity is observed, indicating that there is something that is difficult on the particles/material. Here, the capacity for the 5th cycle was 689 $mAhg^{-1}$ and the final capacity was 631 $mAhg^{-1}$. The carbon-coated SiO_2 cell with $LiPF_6$, however, exhibits a relatively stable capacity, with a capacity of 610 $mAhg^{-1}$ in the 5th cycle and a final capacity of 662 $mAhg^{-1}$. This indicates that cells without carbon-coating are still gaining capacity after the 75th cycle, whereas the cells with carbon-coated SiO_2 cells does not and are considered as closer to their maximal full potential.

In a perfect battery the coulombic efficiency is close to 100%. However, there are factors that reduces the coulombic efficiency in the cell, such as the formation of the SEI and the reaction mechanisms of silica, which has an intrinsic irreversibility. For the irreversible reactions between SiO_2 and Li^+, Li^+ and e^- are consumed. Hence, it is theoretically impossible to achieve 100% coulombic efficiency when irreversible reactions are occurring.

The coulombic efficiencies of the long-term cycled cells, presented in Figure 4.5, are all at ~ 99%, indicating stable and reversible reactions. However, the coulombic efficiency of the carbon-coated SiO_2 cell fluctuates between cycle 47 - 64. This might be caused by incomplete delithiation. However, it might also be a result of inaccuracies during the measurement. From Figure 4.10 it is noticeable that SiO_2 has a higher coulombic efficiency than carbon-coated SiO_2. This might be attributed to the fact that less material is reacting for SiO_2 electrodes, and this reaction might be more stable/reversible than for carbon-coated SiO_2 where there are several electrochemical reactions taking place, i.e. the activation takes more time. The carbon-coating itself or electrochemical milling might also be a reason for this difference.

From the voltage profiles in Figure 4.6a and Figure 4.6b, for SiO_2 cells with LiFSI and $LiPF_6$ respectively, the delithiation potential corresponding to the flatter plateau deceases with increased cycling. This decrease in delithiation potential is also seen in Figure 4.6d for carbon-coated SiO_2 cells with $LiPF_6$, indicating that the reactions are becoming less energetically expensive. The delithiation curves in Figure 4.6c, for carbon-coated SiO_2 cells with LiFSI, does not have an as defined decrease in the delithiation potential, indicating high resistance to delithiation, and lithiation, which might be related to the SEI layer. However, a decrease in the obtained capacity during cycling is noticed. This is due to degradation of the cell, and is clearly seen from the special capacity plot in Figure 4.5c.

The decrease of the energy gap between lithiation and delithiation, as seen from the voltage profiles in Figure 4.6, can also be observed in the differential capacity plots in Figure 4.7. However, here this difference is seen as a shift in the peak centers. This shift during cycling is most likely caused by a significant overpotential in the electrode, due to poor conductivity of the electrode matrix, as supported by the work of Lepoivre *et al.*[37] However, the shift of the peaks might also be attributed to the electrochemical milling upon cycling, causing the material to fracture and crack, exposing new surface to the lithium which again affects the potential.

From Figure 4.8 it is observed that all cells exhibit relatively good cycling stability, which might be attributed to the buffering of the volume expansion of Si by the conversion products, Li_2O, Li_4SiO_4 and $Li_2Si_2O_5$, from the conversion of SiO_2 to Si (reaction 2.18-2.20). In addition, the pores and voids provided by the carbon-coating also provides extra space to accommodate volume variations of SiO_2 upon cycling. The difference in micropore area and external surface area is presented in Figure 5.2 and Table 5.1, where micropores are defined as pores with a width not exceeding ~2 nm.[55] This data is collected from previous work carried out in the project preceding this thesis.[1] As mentioned earlier, the carbon-coated SiO_2 cells achieves higher capacity then "pure" SiO_2 cells, as the coating facilitates better transport of electrons around the SiO_2 particles, creating more active sites for Li^+ to react. The carbon-coating also prevents sintering, increasing the external surface area, as indicated by Figure 5.2 and Table 5.1. A larger external surface provides for increased contact between SiO_2 an Li^+, which attributes to increasing the capacity.

Tab. 5.1. Micropore area and external surface area of SiO_2 and carbon-coated SiO_2

	Micropore area	External surface area
SiO_2	$3.5\ m^2g^{-1}$	$29.8\ m^2g^{-1}$
Carbon-coated SiO_2	$27.4\ m^2g^{-1}$	$57.7\ m^2g^{-1}$

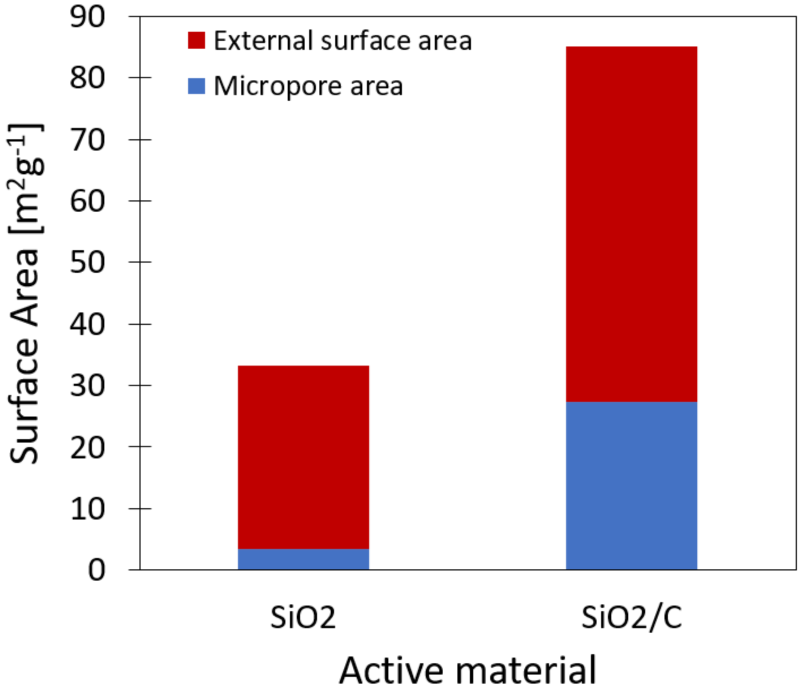

Fig. 5.2. Surface area of milled SiO_2 and milled carbon-coated SiO_2

From Figure 4.8 it is also observed that the starting capacities of carbon-coated SiO_2 cells are very similar, indicating a stable SEI or stability of the microstructure. During cycling some capacity loss of the LiFSI is shown, indicating degradation. Thus, the gap between carbon-coated SiO_2 with LiFSI and $LiPF_6$ increases during cycling. This indicates that for the carbon-coated SiO_2 materials the effect of the electrolyte is more pronounced. For "pure" SiO_2 the capacity gap between LiFSI and $LiPF_6$ gets narrower during cycling, indicating that the effect of poor conductivity is much larger than the effect of the electrolyte.

As seen from Figure 4.8 there are deviations within the same types of cells. This can be caused by several factors; bad adhesion between the current collector and electrode material, limiting the transport of electrons, thus providing an extra voltage drop, agglomerates, trapping the SiO_2 particles, making it difficult for the Li^+ to react with the SiO_2 or a difference in loading during galvanostatic cycling.
The loading during cycling varied some, as seen in Table A.5 in the appendix, due to the non-uniformity of the electrode cast. When the electrode slurry is casted onto the current collector it is hard to make a completely uniform layer, thus the thickness of the different electrodes might vary. To compensate for this, all electrodes are weighted prior to cell installation, so that the mass of the active material can be calculated. However, since the electrodes are very thin there are some uncertainties regarding these measurements. A small difference in loading can impact the capacity of the cell, which might be one of the reasons for the variations within the same types of cells.

5.1.3 Summary of electrochemical characterization

The electrochemical results of the SiO_2 anodes with LiFSI and $LiPF_6$ are similar to results found in the literature of Si anodes with LiFSI and $LiPF_6$.[14] To reveal to reasons of why LiFSI improves the performance of SiO_2 anodes, further study of the SEI, by XPS, was conducted, as the SEI greatly influences the performance of a cell.

5.2 Analysis of the XPS results

5.2.1 Analysis of elemental composition

From the elemental composition collected from the survey scans, presented in Table 4.2, the silicon is detected in larger quantities for $LiPF_6$ than LiFSI at both 0.5 V and 0.2 V. The amount of silicon increases for LiFSI but decreases for $LiPF_6$. However, this decrease in the silicon detected for $LiPF_6$ is so small, that it can be neglected. As the formation of the SEI evolves, less Si will be detected, as the SEI layer covers the electrode surface, thus the Si particles. Based on this, the formation of the SEI evolves more rapidly for cells with LiFSI than $LiPF_6$ as less Si is detected for the former. A possible reason for the increase in Si detected from 0.5 V to 0.2 V in cells with LiFSI is a better conversion of SiO_2 to Si from 0.5 V to 0.2 V, i.e. the SEI is more rich in Si for LiFSI than $LiPF_6$ at 0.2 V.

The amount of carbon that is detected, presented in Table 4.2, comes from both the carbon additive, i.e. carbon black, but also from the electrolyte decomposition, as the electrolyte solvents (EC and DEC) contains carbon. The amount of carbon detected at both 0.5 V and 0.2 V was greater for LiFSI than $LiPF_6$. When comparing the carbon content for the cells stopped at 0.5 V and 0.2 V, the amount of carbon has decreased. This could be due to the formation of the SEI. At 0.2 V the SEI layer formed is more developed than at 0.5 V, thus the carbon from the electrode (i.e. carbon black) is more covered, and not as easily detected. As

the electrolyte decomposes forming the SEI some of the carbon from the electrolyte solvents will be found in the electrolyte decomposition products. However, there is great uncertainty when disusing the carbon-content based on the elemental composition as some of the carbon will be undetected due to the SEI formation, but the SEI itself contains organically- and inorganically bound carbon.
The amount of oxygen detected is higher for LiFSI than $LiPF_6$. From 0.5 V to 0.2 V there is little change amount of oxygen detected for LiFSI. For $LiPF_6$, however, a small decrease is seen. As the amount of O and C detected is higher for cells with LiFSI than cells with $LiPF_6$, this indicates that there are more organic components for LiFSI compared to $LiPF_6$. These organic components can work as a conductive network in the SEI, ensuring high conductivity of Li^+ to the SiO_2/Si particles.

The amount of fluorine was much larger for $LiPF_6$ than LiFSI, which is expected as the amount of fluorine in $LiPF_6$ is three times greater than for LiFSI. From 0.5 V to 0.2 V the amount of fluorine increases, as the fluorine mainly comes from the electrolyte, a more developed SEI will contain more fluorine from electrolyte decomposition. However, higher amount of fluorine can also lead to more trapping of Li during cycling.

For the electrolyte components sulfur and nitrogen, from LiFSI, the amount detected decreases from 0.5 V to 0.2 V, indicating that the reduction of the salt happens early in the SEI formation, i.e. further into the SEI layer. Thus, as the SEI continues to evolve, the salt reduction products gets harder to detect. However, from the elemental composition the presence of salt residues can not be excluded.

The amount of phosphorus detected increases from 0.5 V to 0.2 V. The phosphorus comes from the $LiPF_6$ electrolyte.

5.2.2 Analysis of high resolution peak fitting

The evolution of the Si 2p spectra is seen in Figure 4.11 and corresponding table of atomic concentration is given in Table 4.3. The amount of SiO_2 decreases from 0.5 V to 0.2 V for both cells with LiFSI and cells with $LiPF_6$, indicating that evolution of the conversion of SiO_2 to Si. As for Li_4SiO_4 the amount of the component detected increases from 0.5 V to 0.2 V for both LiFSI and $LiPF_6$. Suggesting the evolution of the SEI formation. The amount of SiO_2 detected is larger for LiFSI than $LiPF_6$, indicating that a thinner SEI layer is formed with LiFSI than $LiPF_6$. Moreover, the amount of Li_4SiO_4 detected is smaller for LiFSI than $LiPF_6$. This indicates that the initial conversion of SiO_2 to Si is going faster for cells with $LiPF_6$ than cells with LiFSI, however the increase in the amount of Li_4SiO_4 detected from 0.5 V to 0.2 V is larger for LiFSI, indicating that this conversion might be "better", i.e. more efficient.
Philippe did a similar study on Si electrodes.[11] The Si 2p spectra ($h\nu$ = 1487 eV) presented in Philippe's work and this work are not similar, given that the Si is used in the former and SiO_2 in the later.[11] However, in both cases peaks attributed to SiO_2 and lithium silicate are identified.

The C 1s spectra is presented in Figure 4.12 and Table 4.5 gives the atomic concentration of the components found in the spectra. When comparing the electrode from cells stopped at 0.5 V and 0.2 V the reduction of C-C and CB for LiFSI and the reduction of CB for $LiPF_6$ is the most noticeable. The detection of these components are reduced as a result of the SEI forming on the surface of the electrode. At 0.5 V the formation of the SEI have already started and new carbonaceous species are present in the SEI. However, the peak attributed to C-C might also contain C-H, which comes from hydrocarbon surface contamination, as the two components have the same binding energy (285 eV[52]). this can explain why the amount of C-C is not reduced from 0.5 V to 0.2 V for $LiPF_6$. At 0.2 V the amount of these carbonaceous species, such as C-O, O-C=O and CO_3 have all increased for the cells with LiFSI, indicating that the growth of the SEI have continued. However, for the $LiPF_6$ cells, the amount of C-O and O-C=O have decreased and CO_3 was not detected. While LEDC, which is one of the most favorable decomposition products of EC, contributes to both C-O and the carbonate feature, Li_2CO_3 is only visible in the carbonate feature.[56] Hence, when CO_3 is not present in the C 1s spectra, there is no Li_2CO_3 and the "new" C- and O- bonds must thus be from organic SEI components.
The carbonaceous species deposited on at the surface of the SEI are assigned to carbonates such as Li_2CO_3 and/or lithium alkyl carbonates.[11]
When comparing the C 1s spectra from this work with the C 1s spectra from Si electrodes with $LiPF_6$ (hν = 1487 eV) presented in Philippe's work, identical components are found in the C 1s spectra except the CO_3 peak, which was not identified for the SiO_2 cells with $LiPF_6$. When comparing the C 1s spectra of SiO_2 with the C 1s spectra of Si with LiFSI (hν = 2300 eV) from Philippe,[11] all components detected are similar.

The O 1s spectra presented in Figure 4.13 and the Table 4.7. Since more oxygen is detected for cells with LiFSI, compared to cells with $LiPF_6$, this implies that more organic components are detected in the analyzed depth of the electrode with LiFSI compared to the electrode with $LiPF_6$. The amount of SiO_2/binder detected decreases from 0.5 V to 0.2 V for the SiO_2 cells with LiFSI, but increased for the cell with $LiPF_6$. However, based on the observation of the SiO_2 from the Si 2p spectra, indicating that the atomic concentration of SiO_2 decreased for all cells, this increase in SiO_2/Binder for $LiPF_6$ must thus be attributed to the binder.
The amount of Li_4SiO_4 also decreases from 0.5 V to 0.2 V for LiFSI, but increased for $LiPF_6$, indicating that this component is not found on the surface of the SEI for LiFSI but rather buried under the SEI. However, as the increase in atomic concentration for Li_4SiO_4 was relatively small for $LiPF_6$, this might also be the case for $LiPF_6$. For the cells with LiFSI the amount of C-O/CO_3 increases greatly from 0.5 V to 0.2 V, as more oxygen is bound to carbon forming carbonaceous species in the SEI. However, for $LiPF_6$ the amount of C-O/CO_3 detected decreases from 0.5 V to 0.2 V. Indicating that $LiPF_6$ reduces at a lower potential, changing the ratio between solvent and salt reduction products in the SEI layer.
For the $LiPF_6$ cells, Li_2O is detected in small amounts, however increasing from 0.5 V to 0.2 V, indicating an increase in the conversion of Si to SiO_2.

The O 1s spectra (hν = 1487 eV) of Si cells with $LiPF_6$, presented in the work of Philippe,[11] have only identified two components for the cell stopped at 0.5 V, a peak attributed to SiO_2

and binder, and a peak attributed to carbonates, alkyl carbonates and organic compounds. However, for the cells stopped at lower potentials during the first discharge a peak attributed to Li_4SiO_4 and a peak attributed to Li_2O was also identified. The O 1s spectra for Si cells with LiFSI presented in Philippe's work is rather similar to his O 1s spectra for $LiPF_6$. For the O 1s spectra of SiO_2 obtained in this work, great resemblance is seen compared to that of Philippe. However, already at 0.5 V both the Li_4SiO_4 peak and the C-O/CO_3 peak is identified. The Li_2O peaks, however, are not as pronounced.

For the F 1s spectra, presented in Figure 4.14 with corresponding table, Table 4.9, the amount of the F-S (from lithium salt) and LiF component decreases and increases respectively for LiFSI from 0.5 V to 0.2 V. For the cell with $LiPF_6$, however, the amount of F-P (from lithium salt) increases while the amount of LiF decreases from 0.5 V to 0.2 V. As the formation of the SEI layer should be more evolved at 0.2 V than 0.5 V, a larger amount of LiF is also expected. However, as this increase is only detected for LiFSI, this suggest that the SEI formation with LiFSI evolves more rapidly than the SEI formation with $LiPF_6$, which was also seen from the Si 2p spectra discussed above. The amount of the lithium salt detected is larger for the $LiPF_6$ cell than LiFSI cell. However, it is unknown if the detection of salt components comes from salt residues on the surface or is decomposed salt in the SEI matrix.
The F 1s spectra for $LiPF_6$ ($h\nu = 1487$ eV) and LiFSI ($h\nu = 810$ eV) presented in Philippe's work showed the same peaks as the ones found in this work. However, the amount of LiF compared to the amount of lithium salt seemed to be larger in Philippe's work, whereas the opposite is true for this work.

From the P 2p spectra, presented in Figure 4.15a and 4.15b and Table 4.11 the amount of P-F detected decreases from 0.5 V to 0.2 V while the amount of P-O simultaneously increases. The reason for this is that P goes from being bound to F in the electrolyte to form phosphates as the electrolyte decomposes. In Philippe's work, the P 2p spectra presented was obtained after the 100th cycle, thus a good comparison to the P 2p spectra presented in this work can not be obtained. However, the same components are observed in both spectra.

For N 1s, presented in Figure 4.15c and 4.15d and Table 4.11, the amount of N-S (LiFSI) detected increased from 0.5 V to 0.2 V, which might be attributed to the evolution of the SEI formation. However, the amount of decomposition products from the lithium salt decreases, indicating that LiFSI reduces at a higher potential, forming a SEI which is rich on salt reduction components closest to the electrode - SEI interface, and with organic components closer to the surface.

The S 2p spectra, given in Figure 4.15e and 4.15f and Table 4.11, shows how the amount of LiFSI detected decreases while the amount of decomposition products from the salt increases, when comparing the cells stopped at 0.5 V and 0.2 V respectively. This indicates that the salt from the electrolyte have decomposed during the formation of the SEI and the decomposition products are allocated in/on the SEI.

As Philippe used soft X-rays when studying the degradation mechanism of the LiFSI salt in his work, a fair comparison to the N 1s and S 2p spectra in this work can not be obtained. However, peaks attributed to the same species are allocated in both cases.

5.3 Analysis of FIB/SEM results

The SEM images from the FIB cross section of pristine SiO_2 electrodes and pristine carbon-coated SiO_2 electrodes, presented in Figure 4.16 indicated that the electrodes with carbon-coated SiO_2 was more porous. As the carbon coating increases the external surface area and micropore area of the SiO_2, as seen from Figure 5.2 and Table 5.1. The layer seen on top of the electrode is a carbon layer deposited on top of the electrode surface, to protect the material during etching with the ion beam.
Figure 4.17, represents cells that were stopped at the second activation cycle. Here, a loss in the porosity of the electrode material is seen for all samples. This indicates that the active material have reacted with the electrolyte, thus the SEI layer have already been formed at this stage of cycling.
From the SEM images of the surface of carbon-coated SiO_2 electrodes, presented in Figure 4.19, the formation of the SEI layer is indicated, as the surface structure of the electrode is not seen as clearly as for the pristine electrode. However, there is a difference in the tilt of this samples upon imaging, which might influence the result to some extent. Moreover, no large cracks were detected, indicating limited volume expansion from reaction between Si and Li^+.

5.4 Comparing LiFSI and $LiPF_6$ electrolytes for algae based silica anodes

For LiFSI to be a viable option as an electrolyte salt, replacing the commercial $LiPF_6$, the cell performance with LiFSI must be competitive to the one seen for $LiPF_6$.

Based on the discussion in the previous section $LiPF_6$ obtained the best performance for carbon-coated SiO_2, with an average capacity of ~ 669 $mAhg^{-1}$, giving an increase of ~71 $mAhg^{-1}$ compared to the cell with LiFSI. For "pure" SiO_2 cells, however, improved performance was seen in cells with LiFSI, obtaining an average capacity of 554 $mAhg^{-1}$, giving an increase in capacity of ~ 38 $mAhg^{-1}$ compared to the cell with $LiPF_6$. This improvement might be attributed to the formation of the SEI as well as the properties of the SEI formed. From the XPS results, conducted on "pure" SiO_2 electrodes, a correlation between the conductivity of the SEI and the thickness of the SEI was seen. The SEI formed on SiO_2 electrodes with LiFSI had more defined layers, where the inorganic components were deposited in the inner part of the SEI, i.e. closes to the electrode surface, and the organic components were found in the outer part of the SEI. This composition of the SEI provides for better flexibility and better Li conductivity. For the SEI, formed with LiPF$_6$, the organic- and inorganic components were more mixed throughout the SEI, making the SEI more rigid.

During the galvanostatic activation of the cells, the coulombic efficiency was very low for all samples, but more so for the "pure" SiO$_2$ cells, as seen in Table 4.1. This indicates irreversible losses caused by the SEI formation but also Li$^+$ consumption due to the conversion reactions of SiO$_2$ (reaction 2.18 - 2.20). For SiO$_2$ to be a good option as anode material, prelithiation should be considered to prevent this initial loss of Li$^+$. However, the coulombic efficiency was stable upon prolonged cycling, at an average value above 99% for all cells.

Chapter 6: Conclusion

The primary goal of this work was to investigate the effect of the LiFSI salt, compared to the common $LiPF_6$ salt, on the electrochemical properties of SiO_2 anodes. In literature, carbon-coating of the SiO_2 have shown to improve the capacity of the cells.[17] Thus, initial electrochemical characterization of the effect of lithium salt was investigated by comparing cells with and without carbon-coated SiO_2, with electrolytes containing different lithium salts. This initial characterization indicated a difference in the activation between coated and uncoated SiO_2 cells. Moreover, the electrochemical reactions was found to take place over a larger potential window for the carbon-coated SiO_2 cells compared to the "pure" SiO_2 cells. In addition, the resistance towards lithiation/delithiation was higher for the carbon-coated cells.

The long-term cycling of the cells showed that for cells with carbon-coated SiO_2 highest capacity was achieved with the $LiPF_6$ salt, 671 $mAhg^{-1}$ after 80 cycles. However for "pure" SiO_2 cells, the highest capacity was achieved with LiFSI salt, 559 $mAhg^{-1}$ after 80 cycles. The fact that higher capacities was achieved with LiFSI in "pure" SiO_2 electrodes corresponds well with literature from studies on Si electrodes, indicating that it is the SEI layer formed on the electrode surface that accounts for most of this improvement.

In an attempt to better understand the improved performance of "pure" SiO_2 cells with LiFSI compared to $LiPF_6$, the SEI, formed during the first lithiation, was studied using XPS. Analysis of the XPS data indicated that the SEI is formed at higher potentials for LiFSI than $LiPF_6$. In addition, more organic components was detected inn the electrodes cycled with LiFSI, contributing to a good conductive network in the SEI. For the electrodes cycled with $LiPF_6$, more inorganic components were detected, indicating that the SEI formed with $LiPF_6$ is more mixed, making it more prone to cracking and lowering the Li conductivity by trapping Li^+ in the SEI. In the SEI formed with LiFSI the inorganic components tends to form in the inner layer of the SEI, while the organic components are formed in the outer layer of the SEI, improving the flexibility of the SEI and the Li conductivity.

Chapter 7: Further work

Good cycling stability was achieved with the cells in this work. However, this stability was only proven up to 80 cycles. Hence, it has jet to be proven if the cycle stability will continue being stable or fade with increased cycling. The industry standard for cycle life time is ~ 1000 cycles, thus, efforts should be made to prove the cycle stability of prolonged cycling in line with the industry standards. Moreover, the applied loading during cycling of the cells in this work was relatively small, ~ 0.44 - 0.54 mgcm^{-2}, thus testing with higher loadings, relevant for industrial applications, should also be tested.
In addition, rate performance testing should be conducted on the cells, to see whether the material can hold different rates during cycling.

The capacity that can be achieved with SiO_2 as anode material is limited due to irreversible conversion reactions of SiO_2 to Si. However, if it is possible to favor the reversible conversion reaction of SiO_2, i.e reaction 2.20, and limit the conversion of SiO_2 by reaction 2.18 and 2.19, it would be possible to achieve higher capacities, as reaction 2.20 is not only reversible but also converts the highest amount of Si.

This work demonstrated that for carbon-coated SiO_2 cells, $LiPF_6$ outperformed LiFSI, whereas for "pure" SiO_2 cells LiFSI outperformed $LiPF_6$. However, the effect of the lithium salts was only tested for 1 M electrolytes, with no additional electrolyte additives. Thereby, extended testing with different electrolyte compositions should be performed.

Bibliography

[1] Anne-Line Berg Korneliussen. Algae based silica anodes for li-ion batteries. Project report in TTM4500, Department of Materilas Science and Engineering, NTNU – Norwegian University of Science and Technology, Dec. 2019.

[2] Andreas Nicolai Norberg, Nils Peter Wagner, Henning Kaland, Fride Vullum-Bruer, and Ann Mari Svensson. Silica from diatom frustules as anode material for Li-ion batteries. *RSC Advances*, 9(70):41228–41239, 12 2019.

[3] J.-M. Tarascon. Key challenges in future Li-battery research. *Philosophical Transactions of the Royal Society A: Mathematical, Physical and Engineering Sciences*, 368(1923):3227–3241, 7 2010.

[4] Joseph M. Ngowi, Lennart Bångens, and Erik O. Ahlgren. Benefits and challenges to productive use of off-grid rural electrification: The case of mini-hydropower in Bulongwa-Tanzania. *Energy for Sustainable Development*, 53:97–103, 12 2019.

[5] Boucar Diouf and Ramchandra Pode. Potential of lithium-ion batteries in renewable energy, 4 2015.

[6] Kirti Richa, Callie W. Babbitt, and Gabrielle Gaustad. Eco-Efficiency Analysis of a Lithium-Ion Battery Waste Hierarchy Inspired by Circular Economy. *Journal of Industrial Ecology*, 21(3):715–730, 6 2017.

[7] Christian Julien, Alain Mauger, Ashok Vijh, and Karim Zaghib. *Lithium Batteries: Science and Technology*. Springer International Publishing, 10 2015.

[8] Vijay A Sethuraman, Venkat Srinivasan, and John Newman. Analysis of Electrochemical Lithiation and Delithiation Kinetics in Silicon. *Journal of The Electrochemical Society*, 160(2):394–403, 2013.

[9] Won Seok Chang, Cheol Min Park, Jae Hun Kim, Young Ugk Kim, Goojin Jeong, and Hun Joon Sohn. Quartz (SiO2): A new energy storage anode material for Li-ion batteries. *Energy and Environmental Science*, 5(5):6895–6899, 5 2012.

[10] Bingkun Guo, Jie Shu, Zhaoxiang Wang, Hong Yang, Lihong Shi, Yinong Liu, and Liquan Chen. Electrochemical reduction of nano-SiO2 in hard carbon as anode material for lithium ion batteries. *Electrochemistry Communications*, 10(12):1876–1878, 12 2008.

[11] Bertrand Philippe. Insights in Li-ion Battery Interfaces through Photoelectron Spectroscopy Depth Profiling. 2013.

[12] John B. Goodenough and Youngsik Kim. Challenges for rechargeable Li batteries, 2 2010.

[13] Heng Zhang, Wenfang Feng, Jin Nie, and Zhibin Zhou. Recent progresses on electrolytes of fluorosulfonimide anions for improving the performances of rechargeable Li and Li-ion battery. *Journal of Fluorine Chemistry*, 174:49–61, 7 2015.

[14] Bertrand Philippe, Rémi Dedryveìre, Mihaela Gorgoi, Haìškan Rensmo, Danielle Gonbeau, and Kristina Edström. Improved performances of nanosilicon electrodes using the salt LiFSI: A photoelectron spectroscopy study. *Journal of the American Chemical Society*, 135(26):9829–9842, 7 2013.

[15] Myland Jan C. Oldham, Keith B. and Alan M. Bond. *Electrochemical Science and Technology*. John Wiley and Sons,Ltd., 2013.

[16] Gianfranco Pistona. *Lithium-ion Batteries Advances and Applications*. Elsevier B.V., 2014.

[17] Andreas Nicolai Norberg. *Exploring Silica from Diatom Frustules as a High Performance, Low Cost and Environmentally Friendly Anode Material for Lithium Ion Batteries*. Norwegian University of Science and Technology, 6 2017.

[18] John B Goodenough and Kyu-Sung Park. The Li-Ion Rechargeable Battery: A Perspective. *Journal of the American Chemical Society*, 135(4):1167–1176, 2013.

[19] Kang Xu. Nonaqueous liquid electrolytes for lithium-based rechargeable batteries. *Chemical Reviews*, 104(10):4303–4417, 10 2004.

[20] Perla B. Balbuena and Yixuan Wang. *Lithium-ion Batteries: Solid-Electrolyte Interphase*. Imperial College Press, 2004.

[21] Yali Liu, Sisi Zhou, Hongbo Han, Hong Li, Jin Nie, Zhibin Zhou, Liquan Chen, and Xuejie Huang. Molten salt electrolyte based on alkali bis(fluorosulfonyl)imides for lithium batteries. *Electrochimica Acta*, 2013.

[22] Hong Bo Han, Si Si Zhou, Dai Jun Zhang, Shao Wei Feng, Li Fei Li, Kai Liu, Wen Fang Feng, Jin Nie, Hong Li, Xue Jie Huang, Michel Armand, and Zhi Bin Zhou. Lithium bis(fluorosulfonyl)imide (LiFSI) as conducting salt for nonaqueous liquid electrolytes for lithium-ion batteries: Physicochemical and electrochemical properties. *Journal of Power Sources*, 2011.

[23] Alexandre Magasinski, Bogdan Zdyrko, Igor Kovalenko, Benjamin Hertzberg, Ruslan Burtovyy, Christopher F. Huebner, Thomas F. Fuller, Igor Luzinov, and Gleb Yushin. Toward efficient binders for Li-ion battery Si-based anodes: Polyacrylic acid. *ACS Applied Materials and Interfaces*, 2(11):3004–3010, 11 2010.

[24] Nam-Soon Choi, Se-Young Ha, Yongwon Lee, Jun Yeong Jang, Myung-Hwan Jeong, Woo Cheol Shin, and Makoto Ue. Recent Progress on Polymeric Binders for Silicon Anodes

in Lithium-Ion Batteries. *Journal of Electrochemical Science and Technology*, 6(2):35–49, 6 2015.

[25] Igor Kovalenko, Bogdan Zdyrko, Alexandre Magasinski, Benjamin Hertzberg, Zoran Milicev, Ruslan Burtovyy, Igor Luzinov, and Gleb Yushin. A major constituent of brown algae for use in high-capacity Li-ion batteries. *Science*, 334(6052):75–79, 10 2011.

[26] Xiuxia Zuo, Jin Zhu, Peter Müller-Buschbaum, and Ya Jun Cheng. Silicon based lithium-ion battery anodes: A chronicle perspective review, 1 2017.

[27] S. Xun, X. Song, L. Wang, M. E. Grass, Z. Liu, V. S. Battaglia, and G. Liu. The Effects of Native Oxide Surface Layer on the Electrochemical Performance of Si Nanoparticle-Based Electrodes. *Journal of The Electrochemical Society*, 158(12):A1260, 2011.

[28] K. Ogata, E. Salager, C. J. Kerr, A. E. Fraser, C. Ducati, A. J. Morris, S. Hofmann, and C. P. Grey. Revealing lithium-silicide phase transformations in nano-structured silicon-based lithium ion batteries via in situ NMR spectroscopy. *Nature Communications*, 5(1):1–11, 2 2014.

[29] C. John Wen and Robert A. Huggins. Chemical diffusion in intermediate phases in the lithium-silicon system. *Journal of Solid State Chemistry*, 37(3):271–278, 5 1981.

[30] Matthew T. McDowell, Seok Woo Lee, William D. Nix, and Yi Cui. 25th Anniversary Article: Understanding the Lithiation of Silicon and Other Alloying Anodes for Lithium-Ion Batteries. *Advanced Materials*, 25(36):4966–4985, 9 2013.

[31] Nam Soon Choi, Kyoung Han Yew, Kyu Youl Lee, Minseok Sung, Ho Kim, and Sung Soo Kim. Effect of fluoroethylene carbonate additive on interfacial properties of silicon thin-film electrode. *Journal of Power Sources*, 161(2):1254–1259, 10 2006.

[32] Wuxiao Wang and Suhui Yang. Enhanced overall electrochemical performance of silicon/carbon anode for lithium-ion batteries using fluoroethylene carbonate as an electrolyte additive. *Journal of Alloys and Compounds*, 695:3249–3255, 2 2017.

[33] L. Martin, H. Martinez, M. Ulldemolins, B. Pecquenard, and F. Le Cras. Evolution of the Si electrode/electrolyte interface in lithium batteries characterized by XPS and AFM techniques: The influence of vinylene carbonate additive. *Solid State Ionics*, 215:36–44, 5 2012.

[34] Libao Chen, Ke Wang, Xiaohua Xie, and Jingying Xie. Effect of vinylene carbonate (VC) as electrolyte additive on electrochemical performance of Si film anode for lithium ion batteries. *Journal of Power Sources*, 174(2):538–543, 12 2007.

[35] B. Gao, S. Sinha, L. Fleming, and O. Zhou. Alloy Formation in Nanostructured Silicon. *Advanced Materials*, 13(11):816–819, 6 2001.

[36] G. Lener, M. Otero, D. E. Barraco, and E. P.M. Leiva. Energetics of silica lithiation and its applications to lithium ion batteries. *Electrochimica Acta*, 259:1053–1058, 1 2018.

[37] Florent Lepoivre, Dominique Larcher, and Jean-Marie Tarascon. Electrochemical Activation of Silica for Enhanced Performances of Si-Based Electrodes. *Journal of The Electrochemical Society*, 163(13):A2791–A2796, 10 2016.

[38] Chien Wen Wang, Kung Wen Liu, Wei Fu Chen, Jing De Zhou, Hong Ping Lin, Chun Han Hsu, and Ping Lin Kuo. Mesoporous SiO2/carbon hollow spheres applied towards a high rate-performance Li-battery anode. *Inorganic Chemistry Frontiers*, 3(11):1398–1405, 11 2016.

[39] Qian Sun, Bing Zhang, and Zheng Wen Fu. Lithium electrochemistry of SiO 2 thin film electrode for lithium-ion batteries. *Applied Surface Science*, 254(13):3774–3779, 4 2008.

[40] Jiguo Tu, Yan Yuan, Pan Zhan, Handong Jiao, Xindong Wang, Hongmin Zhu, and Shuqiang Jiao. Straightforward approach toward SiO2 nanospheres and their superior lithium storage performance. *Journal of Physical Chemistry C*, 118(14):7357–7362, 4 2014.

[41] Huiqiao Li and Haoshen Zhou. Enhancing the performances of Li-ion batteries by carbon-coating: Present and future. *Chemical Communications*, 48(9):1201–1217, 1 2012.

[42] Zhenhui Liu, Qiang Yu, Yunlong Zhao, Ruhan He, Ming Xu, Shihao Feng, Shidong Li, Liang Zhou, and Liqiang Mai. Silicon oxides: A promising family of anode materials for lithium-ion batteries, 1 2019.

[43] Huiqiao Li and Haoshen Zhou. Enhancing the performances of Li-ion batteries by carbon-coating: Present and future. *Chemical Communications*, 48(9):1201–1217, 1 2012.

[44] Nan Yan, Fang Wang, Hao Zhong, Yan Li, Yu Wang, Lin Hu, and Qianwang Chen. Hollow Porous SiO2 nanocubes towards high-performance anodes for lithium-ion batteries. *Scientific Reports*, 3(1):1–6, 3 2013.

[45] Clayton Jeffryes, Jeremy Campbell, Haiyan Li, Jun Jiao, and Gregory Rorrer. The potential of diatom nanobiotechnology for applications in solar cells, batteries, and electroluminescent devices, 10 2011.

[46] Dusan Losic, Rachel J. Pillar, Thorsten Dilger, James G. Mitchell, and Nicolas H. Voelcker. Atomic force microscopy (AFM) characterisation of the porous silica nanostructure of two centric diatoms. *Journal of Porous Materials*, 14(1):61–69, 3 2007.

[47] Hidetaka Konno. X-ray Photoelectron Spectroscopy. In *Materials Science and Engineering of Carbon*, pages 153–171. Elsevier, 1 2016.

[48] Weilie Zhou, Robert Apkarian, Zhong Lin Wang, and David Joy. Fundamentals of scanning electron microscopy (SEM). In *Scanning Microscopy for Nanotechnology: Techniques and Applications*, pages 1–40. Springer New York, 2007.

[49] Lucille A. Giannuzzi and Fred A. Stevie. *Introduction to focused ion beams: Instrumentation, theory, techniques and practice.* Springer US, 2005.

[50] J. C. Burns, L. J. Krause, Dinh Ba Le, L. D. Jensen, A. J. Smith, Deijun Xiong, and J. R. Dahn. Introducing symmetric Li-ion cells as a tool to study cell degradation mechanisms. *Journal of the Electrochemical Society*, 158(12), 2011.

[51] Thermo Scientific XPS: Knowledge Base.

[52] X-ray Photoelectron Spectroscopy (XPS) Reference Pages.

[53] NIST XPS Database, Selected Element Search Menu.

[54] Thomas A. Carlson. *Photoelectron and Auger Spectroscopy*. Springer US, 1975.

[55] Matthias Thommes, Katsumi Kaneko, Alexander V Neimark, James P Olivier, Francisco Rodriguez-Reinoso, Jean Rouquerol, and Kenneth S W Sing. IUPAC Technical Report Physisorption of gases, with special reference to the evaluation of surface area and pore size distribution (IUPAC Technical Report). 2015.

[56] Katarzyna Ciosek Högström, Sara Malmgren, Maria Hahlin, Mihaela Gorgoi, Leif Nyholm, Håkan Rensmo, and Kristina Edström. The buried carbon/solid electrolyte interphase in li-ion batteries studied by hard x-ray photoelectron spectroscopy. *Electrochimica Acta*, 138:430–436, 8 2014.

Chapter A: Appendix

A.1 Supplementary notes on experimental work

A.1.1 Actual Binder Composition

The actual composition of the alginate binder is presented in Table A.1

Tab. A.1. Actual composition of binder

Binder composition	DI-water [mL]	Alginic acid sodium salt [mg]
~ 1:59 Alginate:DI-water	29.507	0.502

A.1.2 Actual carbon-coating composition

The actual composition used for the carbon coating procedure of SiO_2 are presented in Table A.2.

Tab. A.2. Actual composition of the carbon-coating

Coating composition	SiO_2	Carbon precursor (glucose)	DI-water
60 wt% SiO_2 40 wt% carbon precursor	0.7 g	0.4667 g	15 mL

A.1.3 Actual Slurry Composition

An overview of the actual composition of the cast produced is found in Table A.3. Here, binder indicates the amount of alginate binder.

Tab. A.3. Actual composition of casts

Cast	Active material [g]	Carbon black [g]	Binder [g]	Isopropanol [g]
	SiO_2			
SiO_2_1	0.1253	0.0168	1.5109	0.0530
SiO_2_2	0.1253	0.0167	1.5075	0.0524
	SiO_2/C			
SiO_2/C_1	0.1254	0.0168	1.5166	0.0523
SiO_2/C_2	0.1253	0.0166	1.5057	0.0541

Tab. A.4. Actual composition of prepared electrolyte

Nomenclature	Composition	Solvent [mL]	Salt [mg]
LiFSI	~ 1.00 M LiFSI in 50.1:40.9 EC:DEC	$V_{EC} = 2.503$ $V_{DEC} = 2.500$	$m_{LiFSI} = 0.938$

A.2 Experimental matrix of cells

Table A.5 shows an overview of cells assembled and cycled for electrochemical characterization and structural characterization with FIB and XPS. The programs L, S, 0.5, and 0.2 represents cells that are long term cycled, i.e. activation + 75 cycles, short term cycled, i.e. stopped during the second activation, and cells stopped during the first discharge at 0.5 V and 0.2 V, respectively.

Tab. A.5. Experimental matrix

Material system	Galvanostatic Cycling (# cells, Program)	Loading [mg/cm^2]
Cells for electrochemical characterization		
SiO_2-$LiPF_6$	3x, L	0.46/0.47/0.51
SiO_2-LiFSI	3x, L	0.45/0.46/0.46
SiO_2/C-$LiPF_6$	3x, L	0.44/0.46/0.50
SiO_2/C-LiFSI	3x, L	0.54/0.47/0.46
Cells for structural characterization (FIB)		
SiO_2-$LiPF_6$	2x, S	0.43/0.42
SiO_2-LiFSI	2x, S	0.40/0.45
SiO_2/C-$LiPF_6$	2x, S	0.48/0.46
SiO_2/C-LiFSI	2x, S	0.49/0.45
Cells for structural characterization (XPS)		
SiO_2-$LiPF_6$	1x, 0.5	0.46
SiO_2-LiFSI	1x, 0.5	0.46
SiO_2-$LiPF_6$	1x, 0.2	0.46
SiO_2-LiFSI	1x, 0.2	0.50

A.3 Supplementary data on electrochemical characterization

The specific capacity of all cells cycled long-term are presented in Figure A.1 - A.4 below.

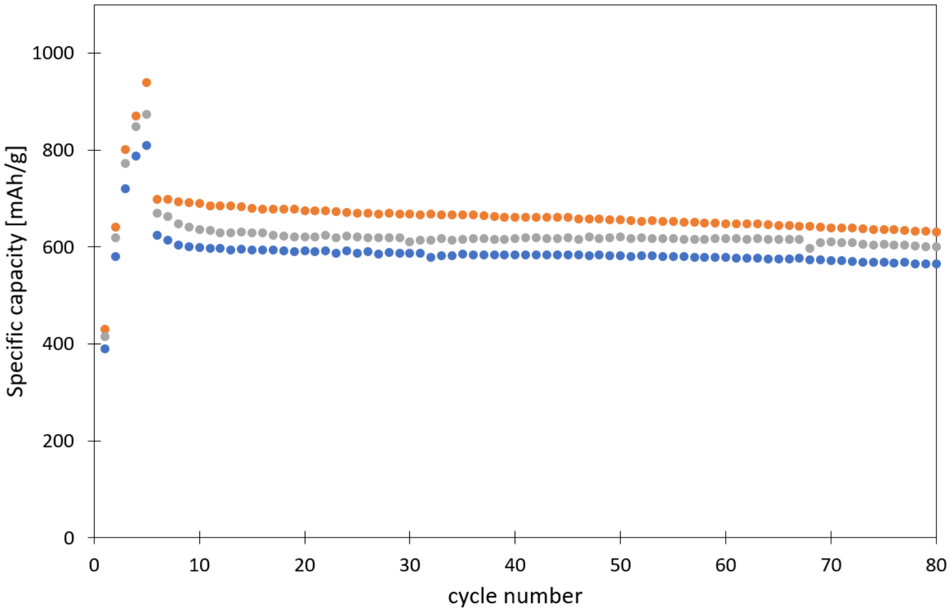

Fig. A.1. Specific capacity for all carbon-coated SiO_2 cells with LiFSI

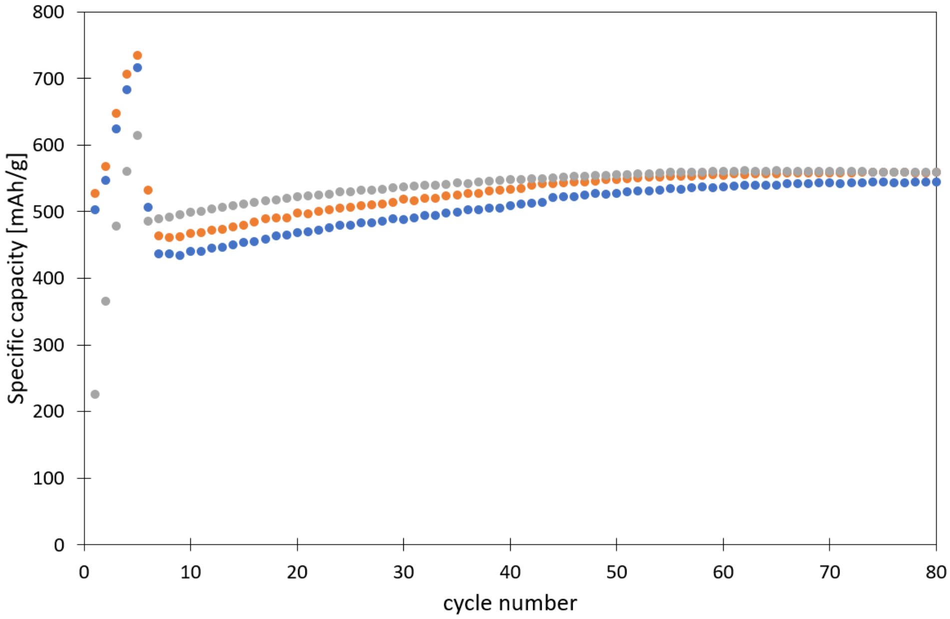

Fig. A.2. Specific capacity for all SiO_2 cells with LiFSI

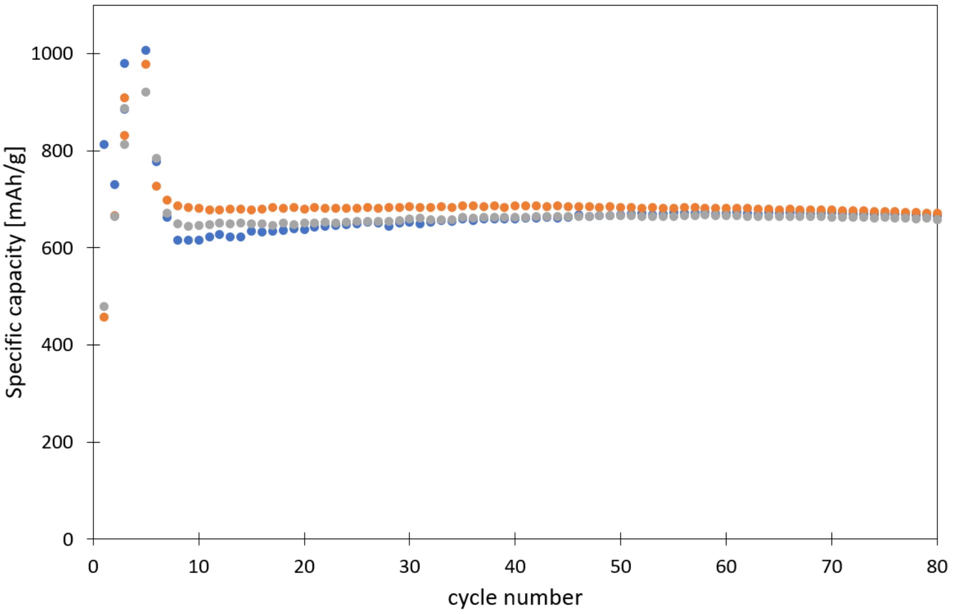

Fig. A.3. Specific capacity for all carbon-coated SiO_2 cells with $LiPF_6$

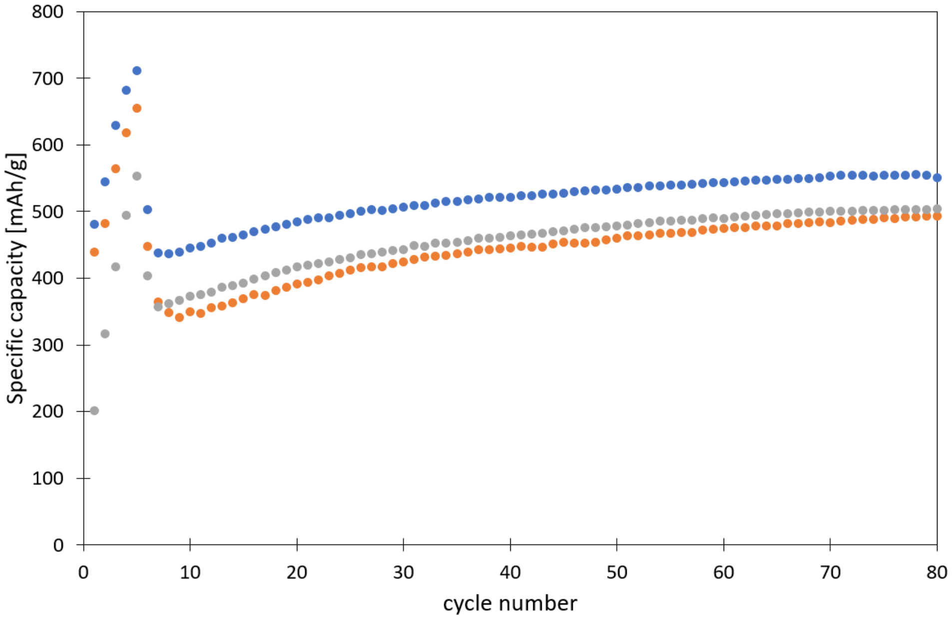

Fig. A.4. Specific capacity for all SiO_2 cells with $LiPF_6$

A.4 Supplementary XPS data

The survey scans collected from the XPS measurements of SiO_2 cells are presented in Figure A.5 - A.8 below.

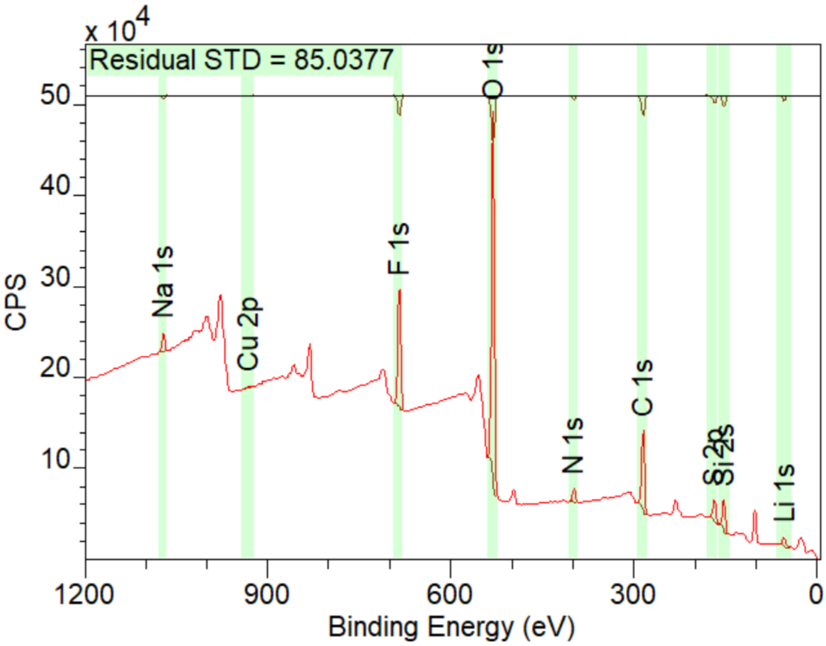

Fig. A.5. Survey scan of SiO_2 cell cycled with LiFSI stopped at 0.5 V during the first lithiation.

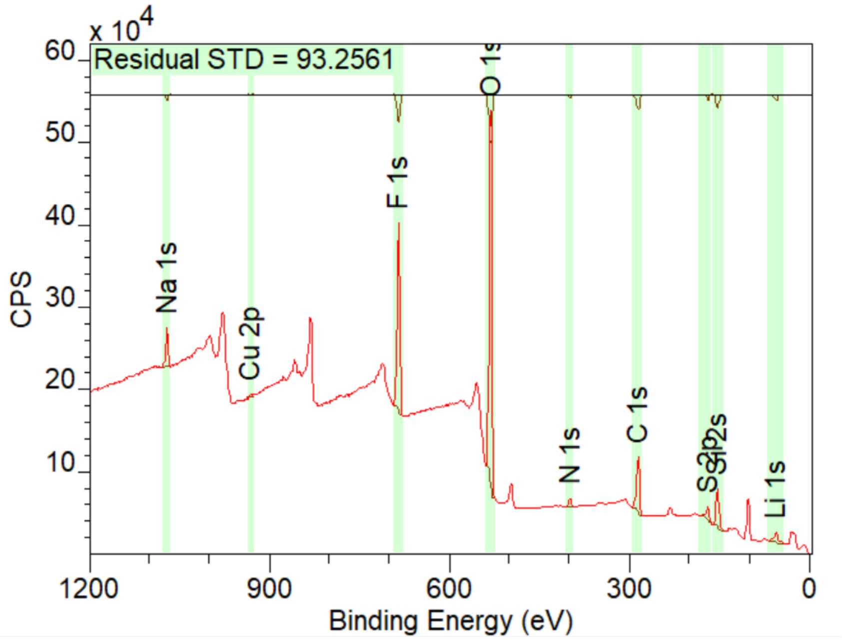

Fig. A.6. Survey scan of SiO_2 cell cycled with LiFSI stopped at 0.2 V during the first lithiation.

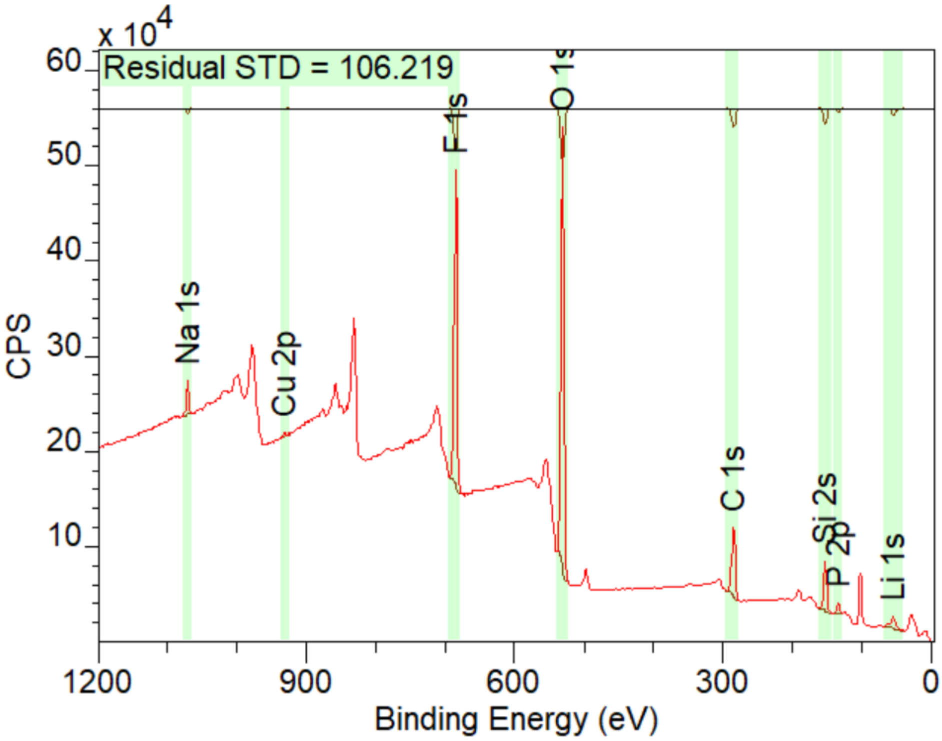

Fig. A.7. Survey scan of SiO_2 cell cycled with $LiPF_6$ stopped at 0.5 V during the first lithiation.

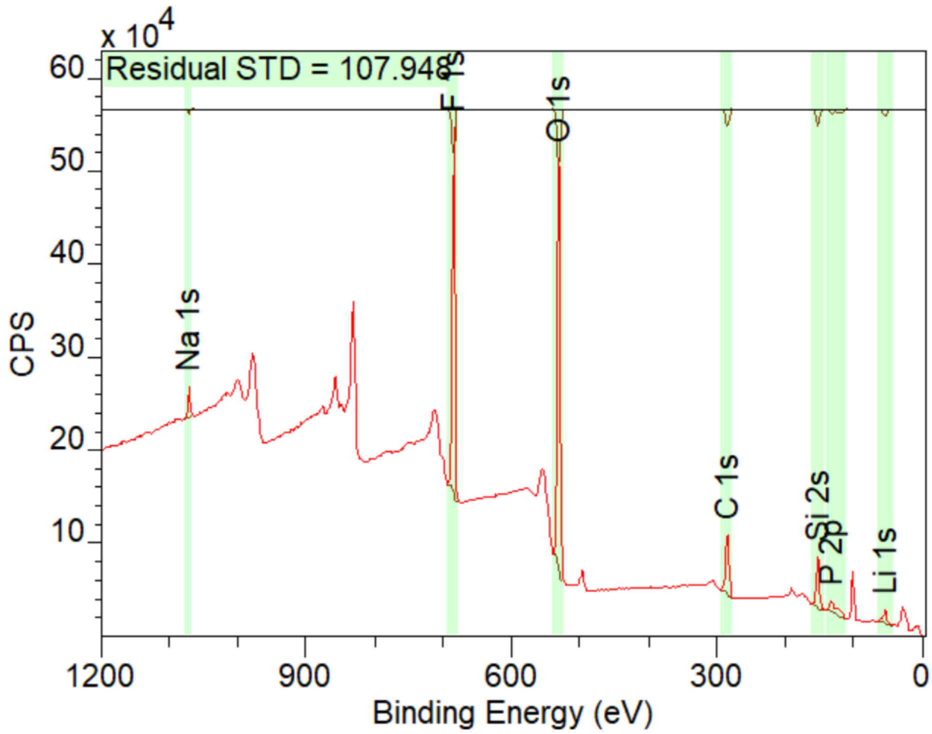

Fig. A.8. Survey scan of SiO_2 cell cycled with $LiPF_6$ stopped at 0.2 V during the first lithiation.

Anne-Line Berg Kornneliussen

Comparing LiFSI and LiPF$_6$ electrolytes for Algae based Silica Anodes in Li-ion Batteries

NTNU
Norwegian University of
Science and Technology